Growth and characterization of silicon and germanium nanowhiskers

DISSERTATION

zur Erlangung des akademischen Grades
doctor rerum naturalium
(Dr. rer. nat.)
im Fach Physik

eingereicht an der
Mathematisch-Naturwissenschaftlichen Fakultät I
Humboldt-Universität zu Berlin

von
Frau Dipl.-Phys. Andrea Kramer
geboren am 16.07.1978 in Singen (Hohentwiel)

Präsident der Humboldt-Universität zu Berlin:
Prof. Dr. Christoph Markschies

Dekan der Mathematisch-Naturwissenschaftlichen Fakultät I:
Prof. Dr. Lutz-Helmut Schön

Gutachter:

1. Prof. Dr. Roberto Fornari
2. Prof. Dr. Dr. h.c. Hans Lüth
3. Prof. Dr. W. Ted Masselink

eingereicht am:	03.09.2008
Tag der mündlichen Prüfung:	19.02.2009

Abstract

This dissertation deals with the growth and the characterization of silicon and germanium nanowhiskers, also called nanorods or nanowires.
The investigation of these structures is of great interest as they represent promising building blocks for future electronic devices. With regard to a possible application, the knowledge of size, crystallographic orientation and position of the nanowhiskers is essential.
The purpose of this work was, therefore, to investigate the growth of Si and Ge nanowhiskers with regard to their size, orientation and position.
The nanowhiskers were grown via physical vapor deposition (PVD) in ultra-high vacuum using the vapor-liquid-solid (VLS) mechanism which is based on growth from solution droplets.
The size of the nanowhiskers could be reproducibly determined by the experimental parameters in the case of Si nanowhiskers on Si(111) with gold as the solvent. A higher gold coverage as well as a higher substrate temperature led to larger droplet diameters and thus to thicker whiskers. A longer silicon evaporation time and a higher silicon rate led to longer whiskers. Thinner whiskers grew faster than thicker ones.
A second material used as the solvent was indium as it is more suitable for electronic application compared to gold. Based on results of droplet formation of the two solvents on silicon, the better results of whisker growth using gold could be explained.
Ge nanowhiskers grown from gold droplets on Ge(111) did not show the [111] orientation of the substrate as in the case of Si nanowhiskers on Si(111) but a <110> orientation. By calculating nucleation energies on different crystal facets, the experimental findings could be explained.
To position nanodroplets of the solvent material and thus to obtain a regular arrangement of nanowhiskers, substrates were pre-structured with nanopores by focused ion beams (FIB). Silicon and germanium nanowhiskers could be epitaxially grown from ordered arrays of gold droplets.

Keywords:
silicon and germanium nanowhiskers, vapor-liquid-solid (VLS) mechanism, physical vapor deposition (PVD), focused ion beams (FIB)

Zusammenfassung

Die vorliegende Dissertation befasst sich mit dem Wachstum und der Charakterisierung von Silizium- und Germanium-Nanodrähten.
Diese Strukturen gelten als aussichtsreiche Komponenten für zukünftige Bauelemente. Für die Anwendung ist die genaue Kenntnis der Größe, der kristallographischen Orientierung und der Position der Nanodrähte erforderlich. Ziel dieser Arbeit war daher die Untersuchung von Si- und Ge-Nanodrähten im Hinblick auf ihre Größe, Orientierung und Position.
Die Herstellung erfolgte durch Physikalische Gasphasenabscheidung (PVD) im Ultrahochvakuum nach dem Vapor-Liquid-Solid (VLS)-Verfahren, das auf dem Wachstum aus Lösungsmitteltröpfchen basiert.
Die Größe der Nanodrähte konnte im Falle von Silizium auf Si(111) mit Gold als Lösungsmittel durch die Parameter des Experiments reproduzierbar bestimmt werden. Höhere Goldbedeckung und höhere Substrattemperaturen führten zu Tröpfchen mit größerem Duchmesser und somit zu dickeren Drähten. Längere Si-Verdampfungszeiten und höhere Si-Verdampfungsraten führten zu längeren Drähten. Dünnere Drähte wuchsen schneller als dickere.
Als zweites Lösungsmittel wurde Indium untersucht, da es sich im Vergleich zu Gold nicht nachteilig auf die elektronischen Eigenschaften von Silizium auswirkt. Basierend auf den Ergebnissen zur Tröpfchenbildung konnten die besseren Wachstumsresultate mit Gold erklärt werden.
Germanium-Nanodrähte, die aus Goldtröpfchen auf Ge(111) gezüchtet wurden, zeigten im Gegensatz zu den Si-Nanodrähten nicht die kristallographische [111]-Orientierung des Substrates, sondern eine <110>-Orientierung, was durch Berechnungen von Keimbildungsenergien auf verschiedenen Kristallflächen erklärt werden konnte.
Zur Anordnung von Metalltröpfchen und damit von Nanodrähten wurden Substrate mithilfe von fokussierten Ionenstrahlen (FIB) vorstrukturiert, um die Tröpfchenbildung an bestimmten Stellen zu begünstigen. Es gelang, aus angeordneten Goldtröpfchen epitaktisch gewachsene Si- und Ge-Nanodrähte zu züchten.

Schlagwörter:
Silizium- und Germanium-Nanodrähte, Vapor-Liquid-Solid (VLS) - Mechanismus, Physikalische Gasphasenabscheidung (PVD), Fokussierte Ionenstrahlen (FIB)

Contents

Introduction

Silicon and germanium nanowhiskers, also called nanowires or nanorods, are of great interest in the field of nanoelectronics as they represent promising building blocks in the bottom-up approach, i.e. the atom-by-atom fabrication of further miniaturized nanodevices. Until now, the top-down technique is most widely applied, consisting of producing ordered nanocomponents by etching or lithographing bulk crystals. Their interface roughness results, however, in scattering of charge carriers which impedes the achievement of theoretically predicted mobilities. The bottom-up technique could avoid these scattering effects [1] and has other advantages as, for example, the possibility of growing radial heterostructures [2].

Si-based electronic devices have dominated integrated circuit technology for many decades. Recently however, germanium has regained importance for electronic applications because of its higher charge carrier mobility compared to silicon. A further advantage of germanium is the larger excitonic Bohr radius (24.3 nm compared to 4.9 nm of silicon) resulting in quantum confinement in larger structures [3]. Yet another advantage is the fact that lower growth temperatures can be applied for germanium [4].

Field effect transistors with good device properties have been produced from single silicon and germanium nanowhiskers [5, 3] as well as from heterostructures of Si/Ge nanowhiskers [6]. However, for the integration of silicon and germanium nanowhiskers in electronic devices, it is essential to reproduce their size and position exactly. Furthermore, most electronic devices are built on (001) substrates, thus it is necessary to induce nanowhisker growth in certain crystal directions, preferably the [001] direction [2].

The purpose of this thesis is, therefore, to investigate the growth of silicon and germanium nanowhiskers with regard to their size, orientation and position.

The growth method, the so-called vapor-liquid-solid mechanism, and the thermodynamic basics related to it will be discussed in chapter 1, as well as the question whether bulk thermodynamics are valid for the nanostructures discussed in this thesis.

The growth is performed by physical vapor deposition in ultra-high vacuum. Chapter 2 presents the experimental setup, which was put into operation during this work, the determination and adjustment of growth parameters and the growth procedure.

As we are interested in controlling the position of nanowhiskers, chapter 3 deals with the influence of focused ion beams applied to different materials. A method is presented as how to provide favored nucleation sites for solution droplets during the vapor-liquid-solid mechanism and thus for the arrangement of nanowhiskers by pre-structuring substrates.

Chapter 4 deals with the characterization methods used for the investigation of the structures grown.

The results of the experiments are presented and discussed in chapter 5.
As the formation of solvent droplets plays an important role in the vapor-liquid-solid mechanism and is highly dependent on the solvent material, the first part of chapter 5 deals with gold and indium droplet formation on silicon. The influence of droplet formation on the outcome of the whisker growth experiment will be discussed as well.
The results of silicon and germanium nanowhisker growth are shown and discussed with regard to their differences. In particular the different directions of growth are considered. A model based on the calculation of nucleation energies will be proposed to explain the directions of growth for silicon and germanium nanowhiskers.
In the last sections of chapter 5, results of SiGe heterostructures and of the arrangement of nanowhiskers will be presented and discussed.

Chapter 1

Vapor-liquid-solid mechanism and thermodynamic basics

As all experiments performed in the course of this work are based on the so-called vapor-liquid-solid (VLS) mechanism, the first part of this chapter discusses its basic principles and its applications.
The second part presents some thermodynamic fundamentals for the description of nanowhisker growth by VLS mechanism.

1.1 The vapor-liquid-solid process

The VLS process was first described for silicon microwhisker growth by Wagner and Ellis [7] in 1964. Some fundamental kinetic aspects of the VLS mechanism were published by Givargizov [8] in 1975. From that time on, many approaches have been undertaken in order to understand and describe this process for the growth of crystalline wires. They vary in the growth method as well as in the materials used, e.g. growth of GaN nanowhiskers by chemical vapor deposition (CVD) [9], growth of InGaAs nanowhiskers by metal-organic vapor phase epitaxy (MOVPE) [10] and growth of Si nanowhiskers by molecular beam epitaxy (MBE) [11], to name just a few. This mechanism is used in other fields of research as well, e.g. for depositing polycrystalline silicon on glass to develop a method for the fabrication of more cost-effective solar cells [12].
According to Wagner and Ellis, the VLS mechanism can be divided into two phases, cf. fig. 1.1, hence the name of the process. During the first phase, a solvent, e.g. gold, forms a liquid (L) solution droplet with the atoms of the substrate, e.g. silicon, at a temperature higher than the eutectic tem-

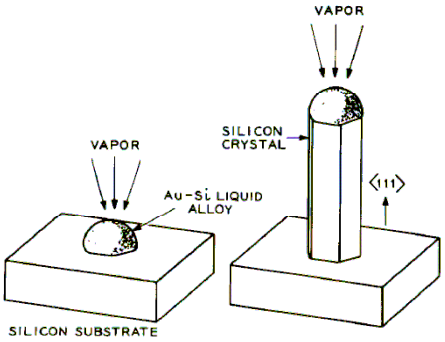

Figure 1.1: The two phases of whisker growth, taken from [7].

perature[1] of the system solvent-substrate. This droplet is a preferred site for atomic deposition out of a supplied vapor (V). Consequently, the liquid solution becomes supersaturated. During the second phase, the droplet (L) precipitates atoms which grow epitaxially on the substrate and by-and-by build a whisker (S).
Although this process seems simple and was discovered more than 40 years ago, many questions remain regarding a detailed description. Especially the application of the VLS mechanism for preparation of nanowhiskers instead of microwhiskers requires a detailed consideration of the thermodynamics in the nanoregime. The second part of this chapter deals with the question whether bulk phase diagrams, which are based on the collective properties of many particles, are still a valid description for the smaller systems. In particular surface effects will play a more important role than in larger systems, see e.g. [13].
Another basic point to consider is the method used to grow the nanowhiskers as it has a strong influence on their shape and especially on the surface state in the space between the whiskers. All experiments described in this thesis were performed by physical vapor deposition (PVD). The particles arriving at the substrate surface are atoms so that processes at the droplet surface can be understood more easily compared to CVD during which a chemical reaction, namely the cracking of a precursor gas, takes place at the droplet surface. On the other hand, in the case of PVD, growth occurs on the whole

[1]Eutectic temperature: Lowest possible temperature at which a eutectic reaction, i.e. a simultaneous crystallization of all constituents at a certain ratio of components takes place.

surface and not only at places at which the precursor gas is cracked. Consequently, in addition to the nanowhiskers, a layer is obtained and whisker growth proceeds more slowly. Apart from that, it is assumed that the atoms which are incorporated into the whisker do not only reach the droplet from the vapor phase but consist also of adatoms which diffuse from the substrate surface and along the whisker sides to the droplet. The role of surface diffusion of adatoms in the PVD case of whisker growth is treated in the second part of this chapter.
A still controversially discussed issue regarding the mechanism of growing whiskers is the aggregation state of the droplet. According to Wagner and Ellis, it is liquid during the whole process. Meanwhile, there are also reports in the literature that for some material systems, growth is based on a solid-phase diffusion mechanism, e.g. gallium arsenide nanowhiskers grown by chemical beam epitaxy [14]. According to these results, a vapor-solid-solid (VSS) process has been proposed which was already named by Bootsma and Gassen in 1971 [15]. There are even reports referring that growth does not occur at all when the particle is liquid. This is e.g. the case for Au-assisted growth of InAs nanowires by MOVPE [16]. Apart from these reports concerning the growth of III-V nanowhiskers, there are also publications which report the growth of silicon nanowhiskers well below the eutectic point of the system with titanium [17] or aluminum as the catalyst [18].
Catalyst-free or self-catalytic nanowhisker growth in order to avoid unwanted incorporation of the catalyst atoms into the wire has been reported, see e.g. [19], but not for silicon whisker growth yet.
In this thesis, all experiments described were performed with a metal particle at temperatures higher than the eutectic temperature of the respective system, thus we assume to grow the nanowhiskers via VLS mechanism.

The next section deals with the thermodynamic fundamentals of the growth process.

1.2 Thermodynamic basics

In the following, some thermodynamical principles [20, 21, 22] necessary for the description of nanowhisker growth will be presented. Most of the whiskers grown during this work have diameters of about 100 nm as will be seen in chapter 5. Thus, the volume of the solution droplet – assuming it to be hemispherical – is $V = \frac{2}{3}\pi r^3 \approx 261800$ nm^3, i.e. the number of atoms in the droplets is in the range of 1 million. The ratio of the number of surface atoms N_S to the number of volume atoms N_V can be estimated by

$$\frac{N_S}{N_V} = \frac{2\pi r^2 \cdot t_S}{\frac{2}{3}\pi r^3 - 2\pi r^2 \cdot t_S} \tag{1.1}$$

with t_S being the "thickness" of the surface layer of the solution droplet. This ratio will be small for r in the range of 50-100 nm and t_S in the range of some Å. This is the reason why we expect bulk thermodynamics to be still valid for our structures.

1.2.1 Material transport and supersaturation

Material transport during the VLS process – as in any other thermodynamical process – is caused by differences between the chemical potentials of different phases.
The chemical potential μ is defined as the derivative of the Gibbs free energy G with respect to the number of particles N at constant pressure p and constant temperature T. U is the internal energy of the system, S the entropy and V the volume:

$$G = U + p \cdot V - T \cdot S \tag{1.2}$$

$$dU = TdS - pdV + \mu dN \tag{1.3}$$

$$\mu = \left(\frac{\delta G}{\delta N}\right)_{T,p=const.} \tag{1.4}$$

Material transport occurs from domains with higher chemical potential to those with lower chemical potential as the whole system tends to be in a state of minimum Gibbs free energy. A material transport according to the VLS mechanism is therefore only possible if

$$\mu_v > \mu_l > \mu_s$$

The subscripts indicate the vapor, liquid or solid phase. The difference of chemical potentials at the phase transition depends on the shape of the interface. The solid-liquid interface is always flat in the VLS mechanism. By contrast, the geometry of the liquid-vapor interface depends on the surface tension of the applied solvent.

Considering the first phase of the VLS mechanism, the formation of a liquid droplet on the substrate, the difference in chemical potentials $\Delta\mu_{VL}$ of a particle before and after being incorporated into the droplet can be derived. For the volume of the vapor, the following is valid:

$$\left(\frac{\delta G}{\delta p}\right)_{T,N=const.} = V_v \tag{1.5}$$

Assuming an ideal gas results in:

$$\left(\frac{\delta G}{\delta p}\right)_{T,N=const.} = \frac{NkT}{p} \tag{1.6}$$

with k being the Boltzmann constant. Integration from equilibrium vapor pressure p_0 to the pressure p yields:

$$\Delta G = G_v - G_l = NkT \cdot ln\frac{p}{p_0} \tag{1.7}$$

Thus, for $\Delta\mu_{VL}$ the following expression is valid:

$$\Delta\mu_{VL} = \mu_v - \mu_l = kT \cdot ln\frac{p}{p_0} \tag{1.8}$$

The curvature of the droplet is neglected in eq. 1.8. However, according to the Gibbs-Thomson effect [23], the vapor pressure of a liquid increases with decreasing radius. The slower growth of thinner whiskers in the case of CVD was explained by this fact, cf. [8], as the higher vapor pressure above the droplet leads to less solvent material incorporated into the droplet. However, we will see that for PVD growth and radii in the range of 50-100 nm, the opposite is the case: thinner whiskers grow faster than thicker ones.

With the simplifying assumption of an ideal solution, the difference in chemical potentials of a particle before and after being incorporated into the crystal during whisker growth can be calculated in an analogous manner to eq. 1.8:

$$\Delta\mu_{LS} = \mu_l - \mu_s = kT \cdot ln\frac{x}{x_0} \tag{1.9}$$

with x being the concentration of the solute in the solvent and x_0 being the equilibrium concentration. $\frac{x}{x_0}$ is called supersaturation which can be experimentally achieved by decreasing the temperature (supercooling) or by increasing the material amount in a solvent above equilibrium.

1.2.2 Nucleation

During the VLS mechanism, two heterogeneous nucleation processes take place. Heterogeneous nucleation is understood as the formation of nuclei at existing surfaces. This is energetically favored compared to homogeneous nucleation during which particles form nuclei in their mother phase without any existing surfaces, see [24]. The first nucleation process is the formation of a liquid droplet from a metal vapor on the substrate. The second occurs inside the droplet on the substrate when the solution is supersaturated and whiskers start growing.

Formation of a liquid droplet on the substrate

Droplet formation plays an essential role in the VLS process and is highly dependent on the solvent and its wetting behavior.
Initially, i particles of the metal vapor are accumulated to a cluster. Let G_i be the Gibbs free energy of this cluster. To determine the nucleation energy ΔG_i of this process, the energy of the system before nucleation has to be subtracted from G_i:

$$\Delta G_i = G_i - i\mu_v - A_{sl}\sigma_{sv} \tag{1.10}$$

μ_v is the chemical potential of a particle in the vapor phase. A_{sl} is the area where the droplet sits on the substrate and σ_{sv} the energy of the interface solid-vapor. When nucleation takes place, the interface energy solid-vapor is reduced by $A_{sl}\sigma_{sv}$. G_i can be written as:

$$G_i = i\mu_l + A_{lv}\sigma_{lv} + A_{sl}\sigma_{sl} \tag{1.11}$$

The first term is the volume contribution, the second and third are surface terms.
Inserting equation 1.11 into 1.10 and applying 1.8 yields:

$$\Delta G_i = A_{lv}\sigma_{lv} - A_{sl}\left(\sigma_{sv} - \sigma_{sl}\right) - ikT \cdot ln\frac{p}{p_0} \tag{1.12}$$

The contribution of the Gibbs-Thomson effect is neglected.
The interface energies and the wetting angle are connected by Young's equation, cf. fig. 1.2[25]:

$$\sigma_{sv} = \sigma_{sl} + \sigma_{lv} \cdot \cos\varphi \tag{1.13}$$

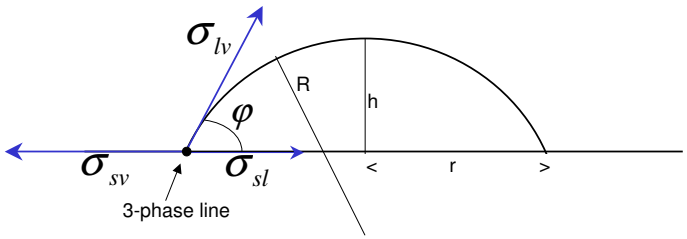

Figure 1.2: Variables used in Young's equation: σ_{sl}, σ_{lv} and σ_{sv} are the different interface energies, φ is the wetting angle. h is the height and R the radius of the spherical cap, r the radius of the circular liquid-solid interface.

Young's equation can be derived by considering the surface tension to be forces acting on the 3-phase line [26]. The sum of their horizontal components has to be zero in equilibrium. The following considerations are valid both for the wetting angle being an acute (= good wettability) or an obtuse one (= poor wettability). Inserting 1.13 into 1.12 yields:

$$\Delta G_i = \sigma_{lv}\left(A_{lv} - A_{sl} \cdot \cos\varphi\right) - ikT \cdot ln\frac{p}{p_0} \tag{1.14}$$

A_{lv} and A_{sl} can be expressed as follows:

$$A_{lv} = 2\pi R^2\left(1 - \cos\varphi\right) \tag{1.15}$$

The surface of a spherical cap of height h is $2\pi Rh$. h can be substituted by $R\left(1 - \cos\varphi\right)$ and eq. 1.15 is obtained. The radius of the circular liquid-solid interface r can be substituted by $R\sin\varphi$:

$$A_{sl} = \pi R^2\left(1 - \cos^2\varphi\right) \tag{1.16}$$

The volume of the liquid spherical cap V_l can be calculated by carrying out the following integration and substituting h by $R(1-\cos\varphi)$:

$$V_l = \int_0^h \pi r(t)^2 dt \tag{1.17}$$

Some geometrical considerations show:

$$r(t)^2 = R^2 - (R-t)^2 \tag{1.18}$$

Thus follows:

$$V_l = \frac{\pi R^3}{3}\left(2 - 3\cos\varphi + \cos^3\varphi\right) \tag{1.19}$$

If n_l is the particle density in the liquid, then $i = n_l \cdot V_l$. The derivative of ΔG_i with respect to R is equated to zero to identify the maximum of the function. For $\varphi = \frac{\pi}{2}$ one obtains the following critical nucleation radius R^*:

$$R^* = \frac{2\sigma_{lv}}{n_l kT \cdot ln\frac{p}{p_0}} \tag{1.20}$$

Formula 1.20 is called the Kelvin equation. For every $R < R^*$ the decomposition of the nucleus is energetically favored whereas for $R > R^*$ the growth of the nucleus is energetically preferred. Fig. 1.3 shows the nucleation energy

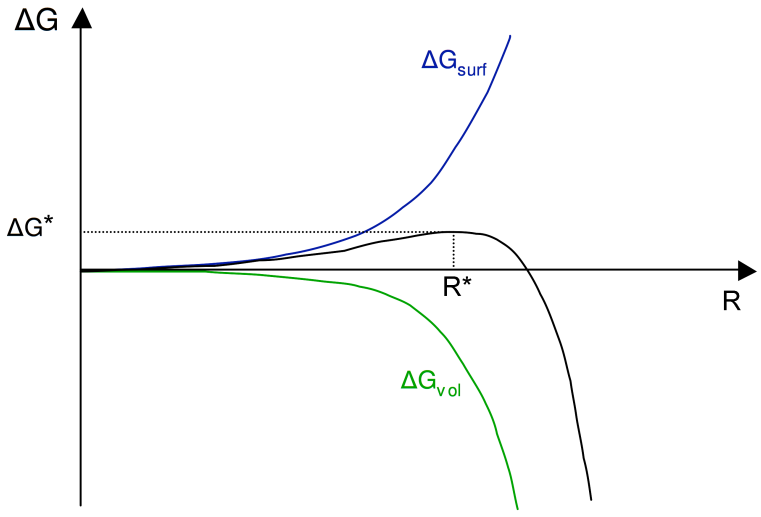

Figure 1.3: Nucleation energy, consisting of a surface and a volume contribution, versus radius of the nucleus.

Heterogeneous nucleation inside the liquid droplet on the substrate

In analogy to the derivation above, one can obtain a critical radius R_s^* for a nucleus on the substrate within the droplet during whisker growth. ΔG_i is in this case:

$$\Delta G_i = i(\mu_s - \mu_l) - A_{ss}\sigma_{sl} + A_{sl}\sigma_{sl} \tag{1.21}$$

The nucleus is assumed to have cylindrical shape with a height of a monoatomic layer. On that condition, R_s^* is found to be:

$$R_s^* = \frac{\sigma_{sl}}{n_s kT \cdot ln\frac{p}{p_0}} \tag{1.22}$$

with n_s being the particle density in the solid.

1.2.3 Phase diagrams

For solution growth of crystals, as occurring in the VLS process, binary phase diagrams play an important role. In such phase diagrams, the temperature is plotted against the relative concentrations of the solvent and the material in solution. The solidus line – below which the solid phase is stable – and the liquidus line – above which the liquid phase is stable – are the lines of the phase transitions. Some phase diagrams exhibit a eutectic point at the composition with the lowest melting point at which the solution components solidify simultaneously. Fig. 1.4 shows the binary phase diagram of silicon and gold.

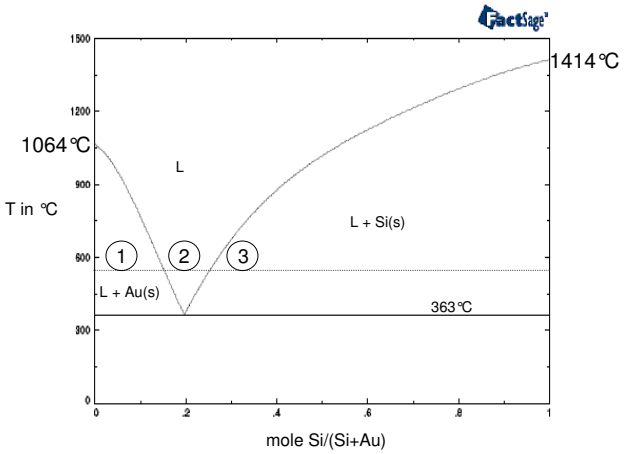

Figure 1.4: Binary phase diagram of silicon and gold.

In order to describe the VLS growth process, it is essential to know how much of the whisker material is dissolved in the metal droplet. For this reason, binary phase diagrams are consulted. However, they are only applicable at equilibrium conditions. Supersaturation is not considered in phase diagrams but growth can only occur if the solution is supersaturated. When growing silicon whiskers from gold droplets, at first gold is evaporated onto the hot silicon substrate (the dashed line in fig. 1.4 indicates our mostly used growth temperature of 550 °C) and gold starts to dissolve silicon atoms which corresponds to region ① in fig. 1.4. Then silicon is evaporated, gold dissolves more silicon and the liquidus line is crossed, i.e. all available gold is liquid. Gold can dissolve silicon until the transition from region ② to region ③. Then the gold droplet is supersaturated and precipitates silicon atoms.
Phase diagrams are valid for systems with sizes at least in the micrometer range. For systems in the nanometer range (1-100 nm), the surface-to-volume ratio has to be considered. If it is not small enough, those systems behave differently than larger systems. Phase diagrams of nanoparticles [27] and nanowires [28] have been treated theoretically in the literature. Adhikari et al. [29] constructed a binary phase diagram valid at the nanoscale and showed a decrease of the eutectic point for 10 to 40 nm diameter gold colloids on germanium. However, we did not find any hint in the literature that bulk phase diagrams are not valid for nanoparticles with diameters around 100 nm.

1.2.4 Influence of diffusion on the growth process

There are basically two different experimental approaches to nanowhisker growth. The first one is accomplished by means of a chemical reaction. In the case of silicon whisker growth, a silane precursor (SiH_4) is commonly used. In this method, the precursor is cracked at the surface of the metal droplet and silicon atoms are obtained and incorporated. Thus, diffusion of atoms on the surface of the wafer does not play an essential role. In the PVD method, atoms are deposited directly from the vapor and are distributed on the whole surface where they diffuse and build a layer. This layer has again an influence on the diffusion which is dependent on the character of the surface. If it is for example oxidized, the diffusion coefficient is different than in case of a pure silicon surface. This will be shown in chapter 5 in which the diffusion of different solvent materials on oxidized and bare Si(111) will be discussed.
The growth of nanowhiskers can be diffusion-limited, i.e. not enough atoms reach the growth interface, or kinetically limited, i.e. limited by the integration of atoms into the whisker.

The influence of diffusion will be presented in the following based on a publication of Dubrovskii et al. [30]. Fig. 1.5 shows their growth model.

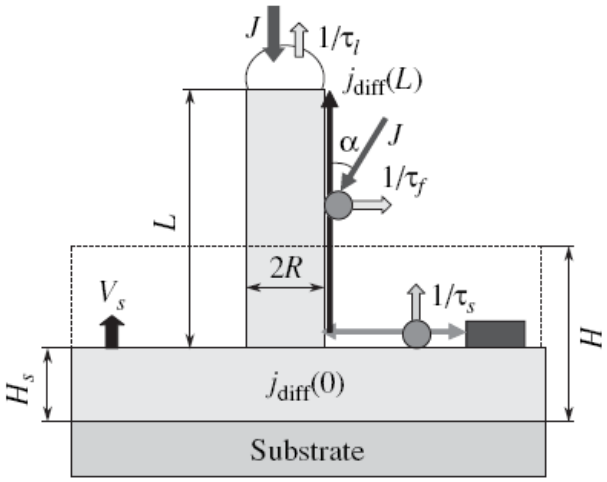

Figure 1.5: Growth model and the basic kinetic processes at the surface according to [30].

The model involves the following processes:

- Adsorption at the droplet surface with intensity $J = \frac{V}{\Omega}$ with V being the deposition rate and Ω the atomic volume in the solid.
- Desorption from the droplet surface with the probability $\frac{1}{\tau_l}$, from the sidewalls with the probability $\frac{1}{\tau_f}$ and from the layer with the probability $\frac{1}{\tau_s}$.
- Layer growth with rate V_s.
- Diffusion flux j_{diff} of adatoms to the top of the whisker.

Diffusion equations are formed for n_s and n_f which are the adatom concentrations at the substrate surface and the side surface of the whisker:

$$D_f \frac{d^2 n_f}{dz^2} + J sin\alpha - \frac{n_f}{\tau_f} = 0 \tag{1.23}$$

$$D_s \Delta n_s + J - \frac{n_s}{\tau_s} = 0 \tag{1.24}$$

with D_s and D_f being the diffusion constants. z is the axis orthogonal to the surface. The general solution depends on the diffusion lengths $\lambda_s = \sqrt{D_s \tau_s}$ and $\lambda_f = \sqrt{D_f \tau_f}$. The boundary conditions are the following:

- The flux of adatoms is zero at the boundary of the feeding zone with radius R_w: $\frac{dn_s}{dr}|_{r=R_w} = 0$. r is the distance from the nanowhisker center.

- Fluxes of adatoms to and from the boundary substrate–nanowhisker are equal: $D_s \frac{dn_s}{dr}|_{r=R} = -D_f \frac{dn_f}{dr}|_{z=0}$.

- The chemical potentials at the boundary substrate–nanowhisker are equal: $\mu_s(R) = \mu_f(0)$.

- Concentration of adatoms at the boundary with the droplet ist zero: $n_f(L) = 0$.

The exact solution for the adatom concentration on sidewalls and substrate surface is obtained from the differential equations and the boundary conditions. The diffusion flux to the nanowhisker top $j_{diff}(L)$ can be written as:

$$j_{diff}(L) = -D_f 2\pi R \cdot \frac{dn_f}{dz}|_{z=L} \tag{1.25}$$

The solution of eq. 1.25 is then inserted into the material balance at the top of the nanowhisker to get the growth rate. As a result, the authors present the following dimensionless equation:

$$\frac{dL}{dH} = \epsilon - \gamma + \frac{R^*(\frac{R}{\lambda_s}, \frac{R_w}{\lambda_s}, \frac{L}{\lambda_f})}{R} \tag{1.26}$$

$\epsilon = 1 - \frac{V_s}{V}$ accounts for the growth of the substrate. $\gamma = \frac{2x_{eq}h}{V\tau_l}$, with x_{eq} being the equilibrium concentration of the atoms in the droplet and h a monolayer, describes desorption from the droplet surface. R^* – called the effective radius – has the dimensionality of length and depends on three parameters. Different limits of equation 1.26 are discussed by Dubrovskii et al. For relatively thick nanowhiskers with a small areal density, R^* can be considered constant. For thinner nanowhiskers, R^* increases. At an increasing density of nanowhiskers, the competition of neighboring nanowhiskers in trapping adatoms plays an important role, and as a result, the length of the nanowhiskers decreases. The authors derive asymptotic behaviors for long ($\frac{L}{\lambda_f} \gg 1$) and for short ($\frac{L}{\lambda_f} \ll 1$) whiskers. They distinguish for the latter also the cases of large or small diffusion lengths ($\frac{R}{\lambda_s} \ll 1$ or $\frac{R}{\lambda_s} \gg 1$) combined with large or small average spacing between the whiskers ($\frac{R_w}{\lambda_s} \gg 1$ or $\frac{R_w}{\lambda_s} \ll 1$).
In chapter 5, this will be discussed with regard to our results.

After having given an introduction into the growth mechanism for nanowhiskers and some thermodynamic basics to describe it, the next chapter will present the experimental setup.

Chapter 2

Experimental setup and growth procedure

In the literature, various approaches to nanowhisker growth using various materials and growth methods can be found, cf. chapter 1. In this thesis, the growth of silicon and germanium nanowhiskers via PVD method is discussed. This chapter deals with the experimental setup and the growth procedure.

2.1 Experimental setup

All experiments have been performed in an ultra-high vacuum (UHV) chamber (fig. 2.1) at a base vacuum of about 2.5 x 10^{-9} mbar. The substrate is inserted upside down into the chamber. It is possible to anneal the sample up to temperatures of about 850 °C. The substrate heater is made of niobium and is placed about 10 mm from the back side of the sample. To measure the substrate temperature, a type K (Chromel/Alumel) thermo couple located between the sample and the heater is used. Thus, the temperature of the sample is not known exactly but after comparison of our results with data from the literature we can assume that the measured temperature is a quite good approximation.
The chamber is equipped with standard effusion cells for indium and gold and with a high temperature effusion source for germanium. Silicon is deposited via electron beam evaporation. Electrons are therefore emitted from a tungsten filament and subsequently bent by a magnetic field and directed to a silicon target where silicon is evaporated.
All evaporation sources have been supplied by Dr. Eberl MBE-Komponenten GmbH.
The composition of the residual gas in the chamber can be in situ monitored

by a quadrupole mass spectrometer (Balzers QMG 421).

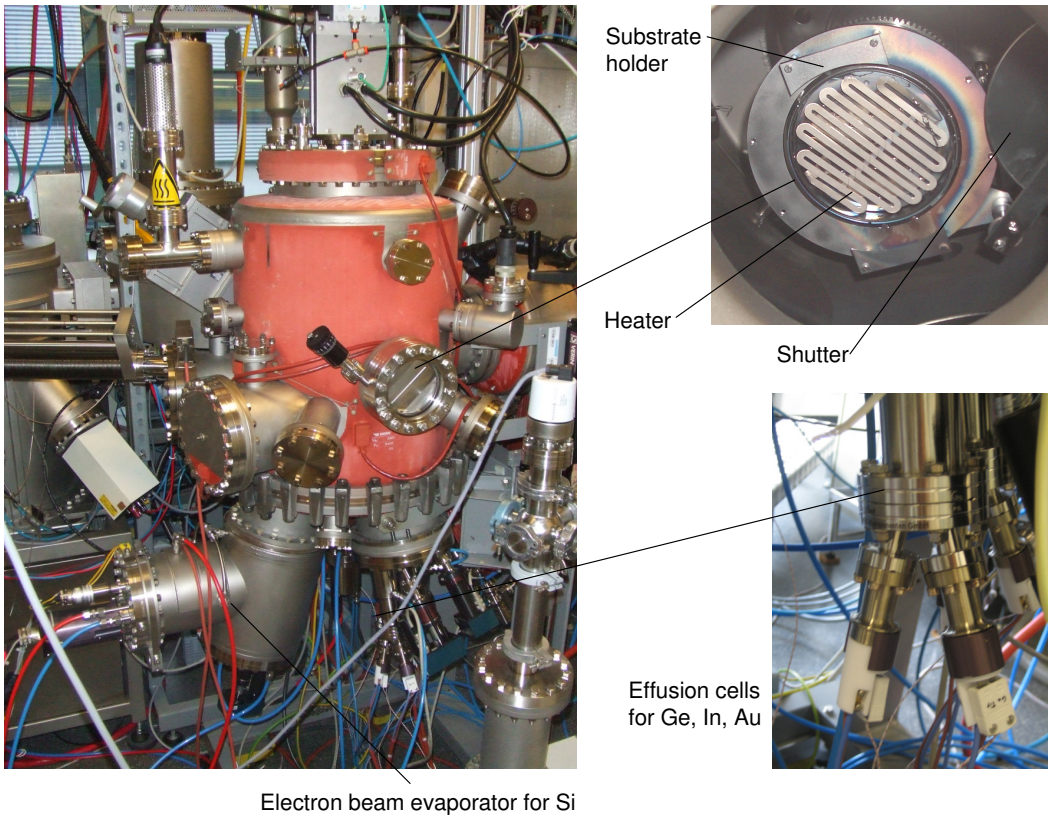

Figure 2.1: The experimental setup.

2.2 Growth procedure

2.2.1 Substrate preparation

Silicon

For our experiments, silicon substrates supplied by CrysTec GmbH Berlin are used. Their dimensions are 25 mm x 25 mm x 0.6 mm and their miscut is less than 0.1°. Both p- and n-doped wafers have been used. Any influence of doping on the outcome of the experiments has not been detected.
Before processing the wafers in UHV, the following cleaning procedure is applied:

Ultrasonic treatment in acetone

The substrates are cleaned for ten minutes by ultrasonic treatment in acetone. Thus, residual particles from substrate machining are removed.

RCA standard clean 1

To remove organic impurities like grease or dust from the surface, the first part of an RCA standard clean process is applied, cf. [31]. For this purpose, an H_2O(deionized) – H_2O_2 – NH_3 solution at a ratio of 5 : 1 : 1 is used (H_2O_2: 31% w/v, NH_3: 28% w/v) to clean the substrate at 80 °C for ten minutes. Ammonia removes organic contaminations, hydrogen peroxide provides a well-defined oxidation of the surface.

HF-dip

After the RCA cleaning procedure, the substrate is dipped into an HF(40% w/v) – H_2O (deionized) solution at a ratio of 1 : 5. Thereby, the oxide is removed and the surface is terminated by atomic hydrogen. As this complete hydrogen termination only lasts for several minutes [32], it is very important to minimize the time between the HF-dip and the insertion of the sample into the UHV chamber.

Germanium

All germanium substrates are cut from crystals grown at IKZ. Their dimensions are 25 mm x 25 mm with various thicknesses. As described by Akane et al. [33], a complete etching of the native oxide can be achieved by dipping the sample into aqueous ammonia (28 % NH_4OH : deionized water = 1 : 4) for at least 120 seconds. The time between etching the substrate and inserting it into the chamber is kept in the range of minutes to avoid oxidation.

2.2.2 Growth parameters and processes in the UHV chamber

Heating

For silicon samples, an oxide desorption step at 850 °C is applied to remove residual oxide which forms in spite of the preceding HF-dip during insertion of the sample into the UHV chamber. For germanium samples, we use a desorption temperature of about 750 °C. In both cases, we achieve clean substrate surfaces whereon epitaxial growth is possible.

Silicon evaporation

The rate of silicon evaporation is related to the current of the electrons emitted in the electron beam evaporator. To determine the dependence of the evaporation rate on the emission current, silicon was deposited with three different currents on a silicon substrate. The thickness of the silicon layers has been determined by x-ray reflectometry, cf. chapter 4. The ratio of layer thickness and evaporation time is the evaporation rate. Fig. 2.2 shows the three calculated rates and a linear fit curve as function of the emission current. The rate is not absolutely stable and there are small errors in time measurement and thickness determination by x-ray reflectometry, but fig. 2.2 can be used as an approximation for the rate dependence on the emission current. The fit indicates a rate error of about 0.03 Å/s.

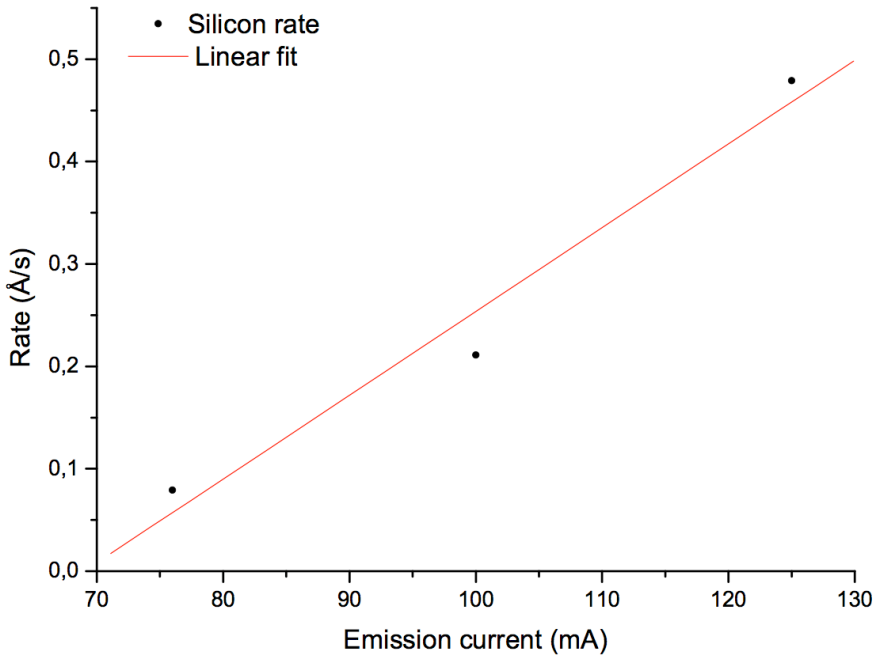

Figure 2.2: Silicon evaporation rate as a function of the emission current.

Germanium evaporation

In order to determine the germanium rate dependence on the temperature of the germanium effusion cell, three layers with different thickness have been deposited on a silicon substrate by evaporating germanium at different source temperatures. The thickness of the germanium layers has been determined by x-ray reflectometry. Fig. 2.3 shows the calculated rate as a function

of temperature. In fig. 2.4, the vapor pressure curve of germanium, and three values corresponding to the experimentally obtained data in fig. 2.3, can be seen. Vapor pressure values were taken from [34]. As expected, the evaporation rate corresponds exactly to the vapor pressure graph.

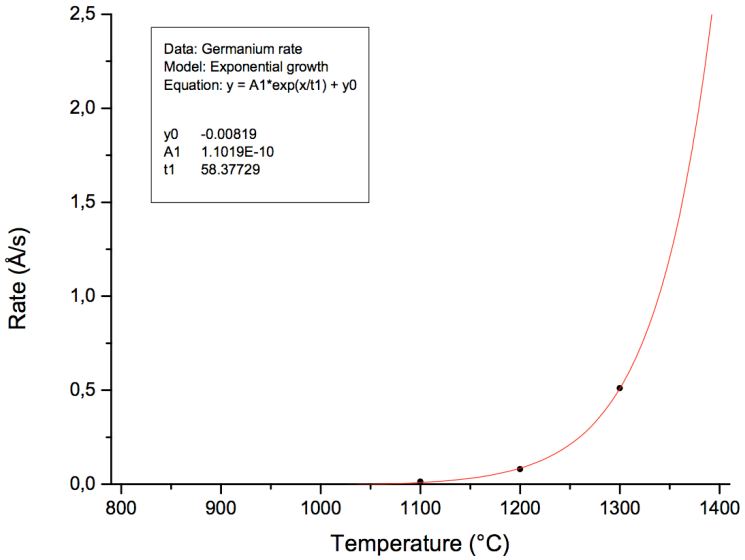

Figure 2.3: Germanium rate as a function of the temperature.

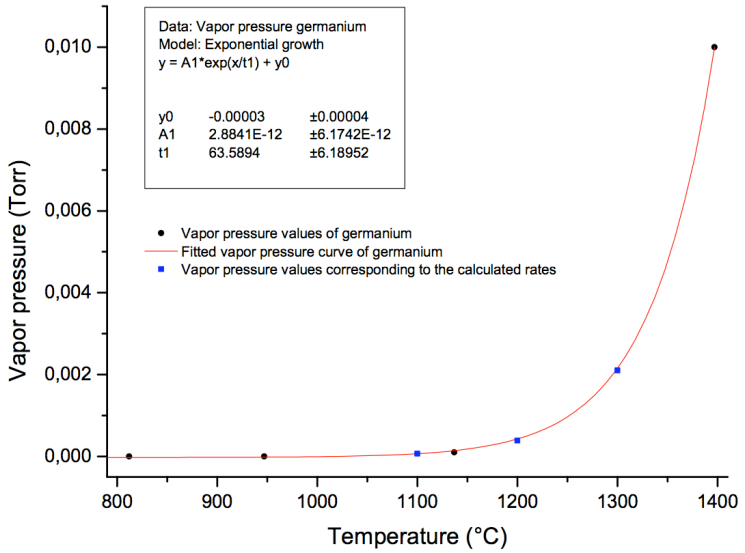

Figure 2.4: Vapor pressure curve of germanium with three experimentally determined data points.

Metal evaporation

The metal evaporation rates are controlled via the source temperatures.
For metals, measurements by x-ray recflectometry cannot be performed as they do not form flat layers, even on substrates at room temperature.

Indium for example behaves as shown on the right when deposited at room temperature. For gold, the vapor pressure curve is almost identical to the one of germanium. The dependence of the rate on the vapor pressure can be calculated by the Hertz-Knudsen equation [35]:

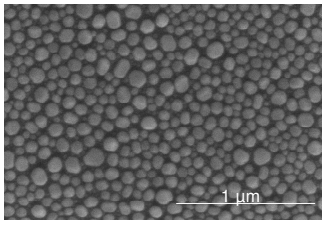

$$J = \alpha \frac{p^* - p}{\sqrt{2\pi m k T}} \tag{2.1}$$

α is a correction factor dependent on the effusion cell, J the number of particles leaving the cell per time and area unit, p^* the vapor pressure of the evaporated material at temperature T and p the pressure in the vacuum chamber. The atomic masses of gold and germanium are 197 amu and 73 amu. Multiplying eq. 2.1 by m yields the mass of the deposited material per time and area unit. Consequently, at the same temperature of the effusion cell, the mass of evaporated gold exceeds the one of germanium by a factor of 1.6. Furthermore, the density of gold (19.3 g/cm^3), calculating with values at room temperature, exceeds the one of germanium (5.3 g/cm^3) by a factor of 3.6. Thus, the volume of deposited gold per time unit is less than half of the volume of germanium. Consequently, the gold rate in length per time unit is about 80 % of the germanium rate.
The indium rate has been determined by weighing samples before and after deposition at three different temperatures. From the sample area and the indium volume, the layer thickness can be calculated and thus the rate. The scales used were Mettler AT20 with an accuracy of 1 µg. The root mean square deviation of 10 measurements was found to be 5-10 µg. The error for the rate is therefore about 0.004-0.008 Å/sec. Fig. 2.5 shows the indium rate against temperature. These data points have been compared with the vapor pressure curve of indium shown in fig. 2.6.

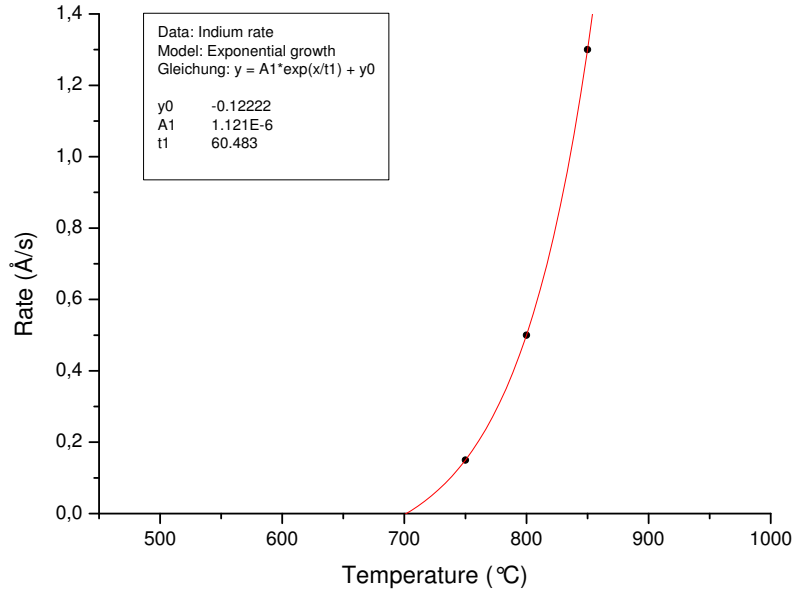

Figure 2.5: Indium rate as a function of the temperature.

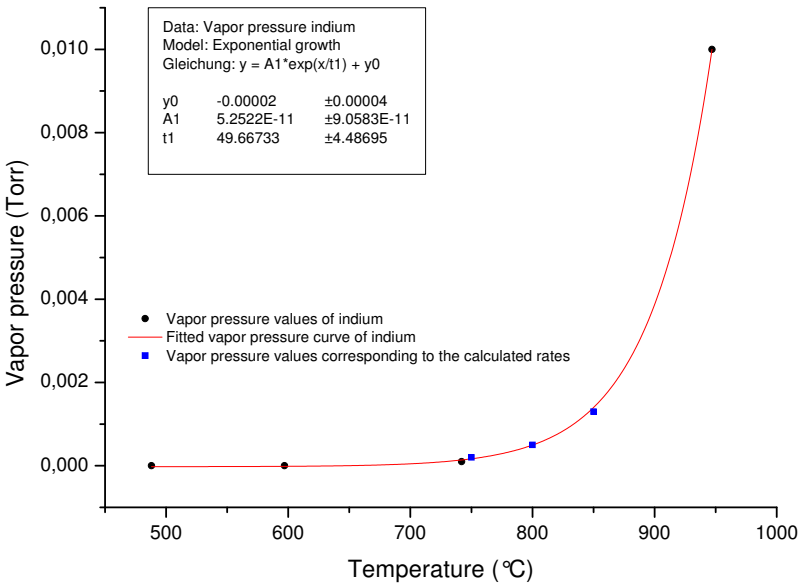

Figure 2.6: Vapor pressure curve of indium with three experimentally determined data points.

The techniques used and the procedures performed in order to grow nanowhiskers have been presented in this chapter. The next chapter will discuss pre-structuring of substrates for the arrangement of droplets and whiskers.

Chapter 3

Structuring of substrates by focused ion beams

With regard to any practical application of nanowhiskers, it is essential to have the possibility to place them in a desired position. A method to pre-structure substrates and to provide preferred nucleation sites on a sample is presented in this chapter.

3.1 The Focused Ion Beam (FIB) system

We use an FEI Nova 600 NanoLab dual beam system for substrate structuring. This system allows structuring by focused Ga^+ ions and simultaneous analyzing of the structure by scanning electron microscopy. The advantage of FIB over other lithography processes is the possibility to structure in the sub-micrometer range without application of any resist. On the other hand, FIB is not useful for large area processing as it is a slow serial process. In the course of this work, FIB has been used to structure substrates before processing them in order to find out if and how this structure influences the growth of nanowhiskers. The following considerations deal with interaction of ions with matter and the setup of the FIB system. They are based on [36].

Interaction of ions with matter

An incident ion is deflected from its path due to collisions with the atoms in the solid material. The ions penetrate to an average depth R_p. A Gaussian fit to the distribution around the depth Z can be written as:

$$G(Z) = \exp\left(\frac{-(Z - R_p)}{2(\Delta R_p)^2}\right) \tag{3.1}$$

The collisions with atoms cause an uncertainty of the ion position in horizontal direction. Light ions reach a larger average depth than heavier ones and scatter more.
An incident ion causes several interactions with matter which can be seen schematically in fig. 3.1.

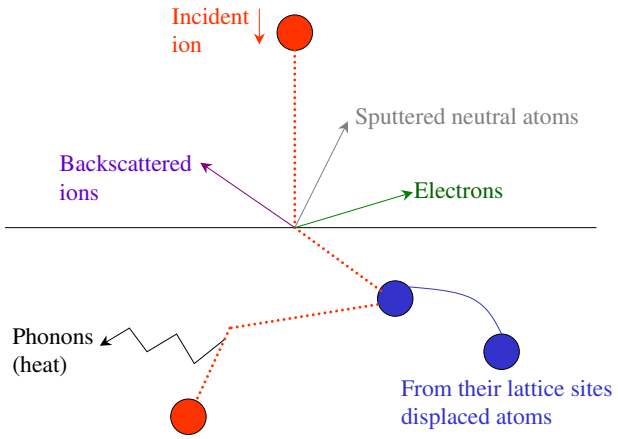

Figure 3.1: Interactions of incident ions in a solid material.

Interactions of incident ions with the solid are summarized in the following:

- Incident ions cause displacement of atoms from their lattice sites. If the ions are heavy enough, an amorphous layer forms.
- Atoms and ions are emitted from the sample. The number of atoms and ions sputtered per incident ion is proportional to the energy of the ion until 100 keV. At higher energies, it is again decreasing. Typical values are 1 to 10 atoms or ions per incident ion, which leave the surface with energies of some eV.
- As well as atoms and ions, electrons are emitted, about 1 to 10 per ion, with energies of some eV.
- Emission of phonons is stimulated and leads to heat generation.

The last point should be considered in more detail because phonon emission occurs especially when treating a sample by focused ion beams whereas all the other effects also take place during any bombardment of a sample with

ions. The heat which is generated in the sample during bombardment by an ion beam is $P_{tot} = U \cdot J \cdot A$, U being the beam voltage, J the current density and A the cross section of the beam. At equilibrium conditions, the heat which is generated in the substrate by the ion beam is equal to the heat which is flowing out of a certain area by heat conduction. Let us consider a hemisphere with radius ρ under the surface of the substrate. The heat conducted per time unit through the area of this hemisphere is $Q = -K \cdot 2\pi\rho^2 \cdot \frac{dT}{d\rho}$. K is the thermal conductivity of the substrate, T the temperature. Equalizing Q and P_{tot} and integrating over ρ, yields:

$$T(\rho) - T(\infty) = \frac{U \cdot J \cdot r^2}{2 \cdot K \cdot \rho} \tag{3.2}$$

$T(\infty)$ is the background temperature and r is the beam radius. If this macroscopic formula is equally valid for microscopic areas, the temperature increase during FIB treatment along ρ can be calculated.

Setup of the FIB system

A FIB system consists of an ion source and an optics column which will be described in more detail in the following.

(a) The ion source

Ideally, the ion source should emit ions from a single point into a limited solid angle. This can be understood easily in analogy to optics, in which a bright source and lenses are needed to focus on a small point. The "brightness" B of an ion source is defined as $B = \frac{I_S}{A_S \Omega_S}$. I_S is the current emitted by an area A_S of the source into the solid angle Ω_S.
Most of the FIB systems are equipped with liquid metal field ionization sources. These sources consist of a tungsten needle whose tip is wetted by liquid metal. An electrical field is applied between the tip and an aperture below it. The geometrical shape of the liquid metal changes and its radius becomes smaller. Because of the high electrical field, ions are finally emitted from the tip.
The ions leave the liquid metal which has a diameter of about 100 Å, but the emission seems to be generated at a virtual tip of 500-1000 Å. This is caused by the electrical field of neighbor ions overlapping the outer electrical field. It results in velocity components of the ions in every direction. But not only the virtual diameter of the emission tip is larger but also the energy distribution of the ions is broader. A limiting of the ion current can reduce these effects.

(b) The optics column

1. The lens system
In contrast to electrons which are focused by electromagnetic fields, lenses for ions are electrostatic fields due to the higher mass of ions. The lenses consist of concentric electrodes. The beam passes through and is deflected and accelerated by the electric fields.
Similar to the chromatic aberration for optical lenses, the focal length of an electrostatic lens is not constant but depends on the energy of the ions. This chromatic aberration causes a contribution to the beam diameter of d_c:

$$d_c = C_c \alpha \left(\frac{\Delta E}{E} \right) \tag{3.3}$$

C_c is the chromatic aberration coefficient, α is the half-angle of the beam arriving at the focal spot, ΔE is the energy width and E the total energy of the ions. The reason for the energy width is the mutual repulsion of the ions, as already described.
Another reason for the increase of the beam diameter is spherical aberration caused by the not perfectly radial focusing fields of the lens, i.e. the focal length is depending on how far from the axis an ion passes the lens. The contribution of this effect to the beam diameter is:

$$d_s = \left(\frac{1}{2} \right) C_s \alpha^3 \tag{3.4}$$

C_s is the spherical aberration coefficient. For small angles, which is mostly the case, this contribution is negligible.
The total diameter of the beam spot d can be calculated as follows:

$$d = \left(d_0^2 M^2 + d_c^2 + d_s^2 \right)^{\frac{1}{2}} \tag{3.5}$$

d_0 is the virtual source diameter and M the magnification of the lens system. By reducing the diameter of the aperture, α is reduced, and thus d_c and d_s. d_c can be also decreased by increasing E.
Yet another lens error is astigmatism which is caused by asymmetry in the focusing field. It results in elliptic images of circular structures.

2. The mass separator
If materials with a high melting point are desired to serve as ion source, they are often incorporated into alloys. In this case, different ions are emitted simultaneously from the source. To separate them, mass separators, i.e. electric and magnetic fields, are used. This is mentioned here for the sake of

completeness, but as we have a simple Ga source in our system, this technique will not be explained in detail.

3. Beam blanking and deflection
For irradiating only certain points on a sample, it is important to have the possibility of turning the beam off. This is achieved by applying an electrical field which by deflecting the beam keeps it from passing through the aperture. There is always a finite time until the blanking effect is established. At high writing speed, this results in a blur of the structure.

In this section, the focused ion beam system has been described. In the next one, its application with regard to our samples will be presented.

3.2 Pre-structuring of substrates

For our experiments regarding the arrangement of nanowhiskers, silicon or germanium substrates have been pre-structured with nanopores by FIB treatment. In this procedure, depth, distance and width of the nanopores can be chosen within certain limits which will be explained in more detail in this section.

3.2.1 III-V materials

Although we are mostly interested in structuring silicon and germanium, we also performed several experiments with III-V materials as they are very appropriate in order to study the influence of FIB treatment. Above a certain temperature, called the incongruent evaporation temperature, the V component is evaporated and a droplet of the III component is left on the substrate surface. This is well-known for annealed bulk material [37] but it can also be achieved by ion bombardment of the sample surface.

Gallium arsenide

Experiment 1

For the first experiment, the pattern shown in fig. 3.2 with squares of 10 x 10 μm^2 was chosen for structuring GaAs. If the ion current I, the acceleration voltage U and the depth value $Z(Si)$ are given, the device determines the energy E necessary to cause the depth $Z(Si)$ in silicon on the given conditions in the chosen area. I determines the diameter of the ion beam. The values of the beam diameter relative to the beam current are shown in table 3.1 for our system. These values are a result of the information about the pitch width of two points which are structured one after the other if their overlap is zero. The pitch width determines the number of structured points in the squares. The energy introduced into the sample per point is $I \cdot U \cdot D$, where D is the dwell time of the ion beam per point. The number of cycles is a result of this value if the total energy necessary to cause the depth $Z(Si)$ is known assuming that there is an overlap of zero between two structured points.

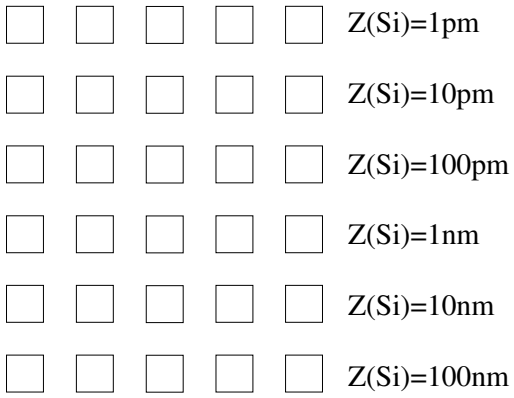

Figure 3.2: Pattern to be structured in experiment 1.

I	Beam diameter
5 nA	110 nm
1 nA	50 nm
100 pA	23 nm
10 pA	12 nm
1 pA	7 nm

Table 3.1: Beam diameter relative to the ion current.

The pattern in fig. 3.2 was structured by 5 different ion currents: I_1=1 pA, I_2=10 pA, I_3=100 pA, I_4=1 nA and I_5=5 nA. For all currents, the acceleration voltage U was 30 kV , the pitch width PW 50 nm and the dwell time per point of the ion beam D 1 μs. By choosing one pitch width for all currents, the energy input is changed, because the number of cycles of the ion beam is only determined by the beam radius, i.e. the current, and by the voltage and the dwell time as described above. The fixed pitch width results in an overlap of two structured points different from zero but the number of cycles of the ion beam remains constant. Consequently, less energy is introduced into the structure at a negative overlap and more at a positive overlap, cf. fig. 3.3.

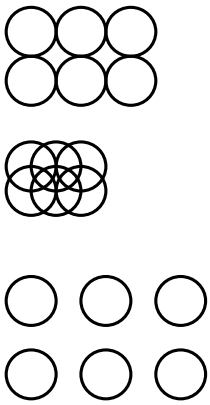

Figure 3.3: Overlap of ion milling: top 0 %, middle 50 %, bottom -50 %

Fig. 3.4 shows the results of experiment 1 which were obtained by atomic force microscopy (AFM) measurements.

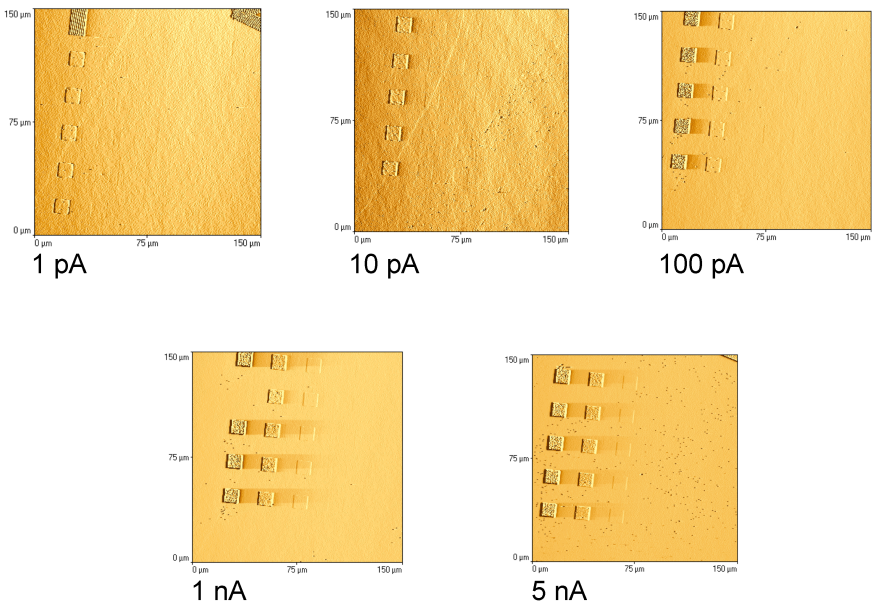

Figure 3.4: AFM images of the structured substrate, with increasing ion current from top left to bottom right.

Some of the squares were not visible by AFM. At currents higher than 100 pA and depths larger than 100 nm, droplets formed, see fig. 3.5. This was probably the point at which the above mentioned incongruent As evaporation began.

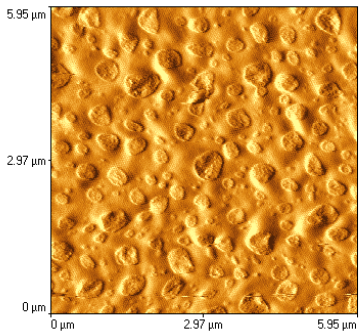

Figure 3.5: AFM image: structure milled at a current of 5 nA and Z(Si)=100 nm.

According to equation 3.2, the increase of temperature by focused ion beam treatment on the area of a hemisphere with radius R ($R \geq$ radius of the beam r) under the sample surface can be calculated as follows:

$$T(R) - T(\infty) = \frac{U \cdot J \cdot r^2}{2 \cdot K \cdot R}$$

$J = \frac{I}{\pi r^2}$, thus:

$$\Delta T(R) = \frac{U \cdot I}{2 \cdot \pi \cdot K \cdot R} \tag{3.6}$$

Table 3.2 shows the dependence of ΔT on the current I, which determines the beam radius r. K is 0.5 $\frac{\mathrm{W}}{\mathrm{cm \cdot K}}$ for GaAs.

I	$\Delta T(r)$
5 nA	8.7 K
1 nA	3.8 K
100 pA	0.83 K
10 pA	0.16 K
1 pA	0.03 K

Table 3.2: The dependence of ΔT on the current I.

Equation 3.6 is time-independent because it results from equating two terms of power: one is the energy input per time unit introduced into the sample by the ion beam and the other one is the heat conducted per time unit through the surface of a hemisphere of radius r. Consequently, ΔT is independent of the irradiation time. With the largest value for I, i.e. 5 nA, ΔT is about 9 K on a hemisphere with radius r below the sample surface, nowhere near being the temperature of incongruent evaporation which is for GaAs about 630 °C [38]. Thus, equation 3.6 cannot account for the experimental results. Table 3.3 shows the different doses for experiment 1. In comparison to the AFM images in fig. 3.4, one can see that droplets form above a certain dose. The doses, which led to droplet formation are colored red. The hyphens in the table 3.3 indicate that the time t was too short to be specified by the device.

	Z1	Z2	Z3	Z4	Z5	Z6
I1	-	0.01	0.06	0.81	8.13	81.25
I2	-	0.03	0.25	2.5	25	242
I3	-	-	1	6.25	88	880
I4	-	-	5	43	440	4300
I5	-	-	-	38	310	4100

Table 3.3: Dose $\frac{I \cdot t}{A \cdot e}$ in 10^{14} cm^{-2}, dependent on depth Z and ion current I, with t time for structuring the square, A: area of the square, e: elementary charge.

Experiment 2

To find out if there is a threshold current below which droplet formation does not occur, the dose was kept constant at 800 x 10^{14} cm^{-2} for the currents 1 pA, 10 pA, 100 pA and 1 nA in experiment 2. The pitch width was again 50 nm during the whole experiment. Fig. 3.6 shows that droplets form at any of the chosen currents. The critical value for droplet formation is - as already supposed above - the ion dose.

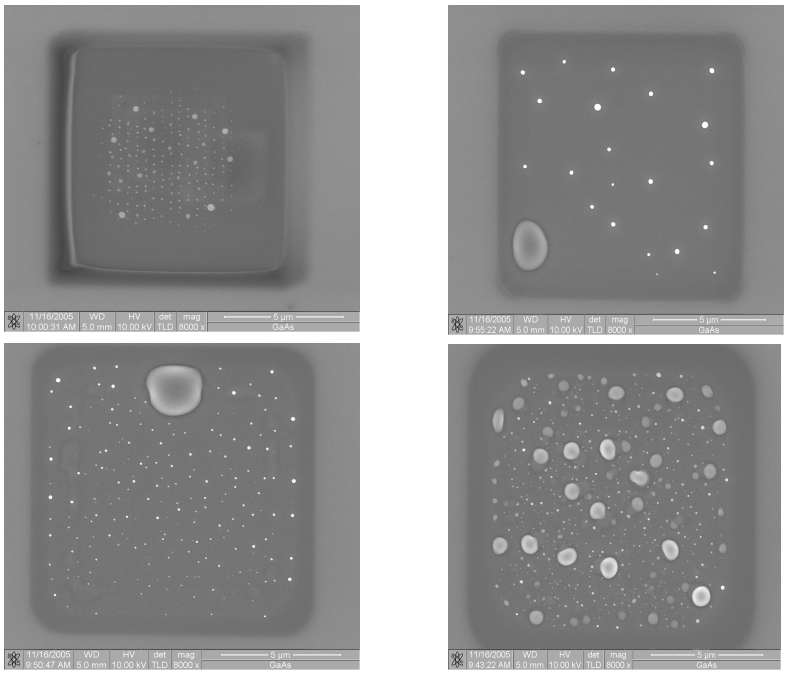

Figure 3.6: SEM images of experiment 2 with increasing ion current from top left to bottom right.

Experiment 3

Experiment 3 was carried out in order to find the lowest dose at which droplet formation occurs. The ion current for this experiment was 1 pA, the depth and thus the structuring time was varied. The lowest dose resulting in droplet formation was found to be about 125 x 10^{14} cm^{-2}.

GaP, InP, InAs

Experiments 1 and 3 were repeated with gallium phosphide, indium phosphide and indium arsenide. The temperatures of incongruent evaporation for the three materials are 780 °C (GaP) [39], 355 °C (InP) [40] and 500 °C (InAs) [41]. The lowest doses for droplet formation were found to be about 250 x 10^{14} cm^{-2}, 40 x 10^{14} cm^{-2} and 80 x 10^{14} cm^{-2}, respectively.

Discussion of results

As already observed above, the temperature rise needed for incongruent evaporation cannot be explained by a simple calculation of energy input and heat conduction. It has been shown that droplet formation depends on the ion dose. The energy needed for incongruent evaporation seems to be accumulated during irradiation due to irreversible interactions. The experiments were performed at room temperature, i.e. the energy input by the ion beam corresponds to the difference between temperature of incongruent evaporation and room temperature. This is shown in fig. 3.7 for the four investigated materials versus the determined lowest dose for droplet formation.

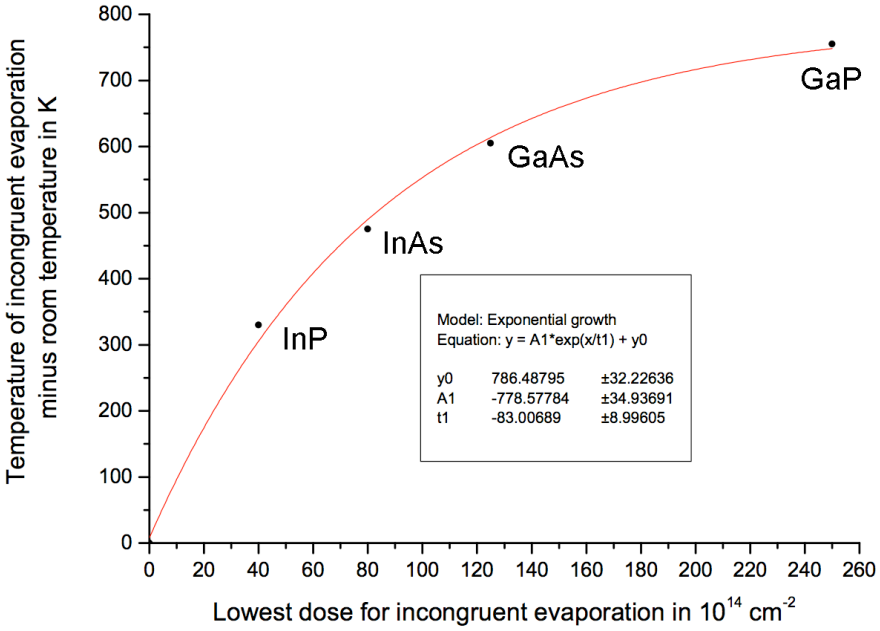

Figure 3.7: Temperature of incongruent evaporation versus the determined lowest dose.

There is obviously no linear dependence between ion input and the temperature of incongruent evaporation but an exponential one. Thus, at a higher equivalent temperature, a higher ion dose is necessary in order to have the same effect on the material. It seems that at a certain dose, a saturation effect is occurring.
Even though the processes have not been investigated in detail, an unambiguous correlation has been found between ion irradiation and the temperature of incongruent evaporation.

3.2.2 Silicon

For the investigation of structuring silicon and germanium, the pattern shown in fig. 3.8 was chosen.

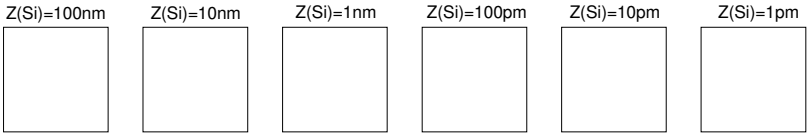

Figure 3.8: Pattern chosen for structuring silicon and germanium with five different currents.

The pitch width PW was set to 50 nm for each current, the acceleration voltage U was 30 kV and the dwell time per point of the ion beam D 1 µs. Fig. 3.9 shows the results of structuring measured by AFM.

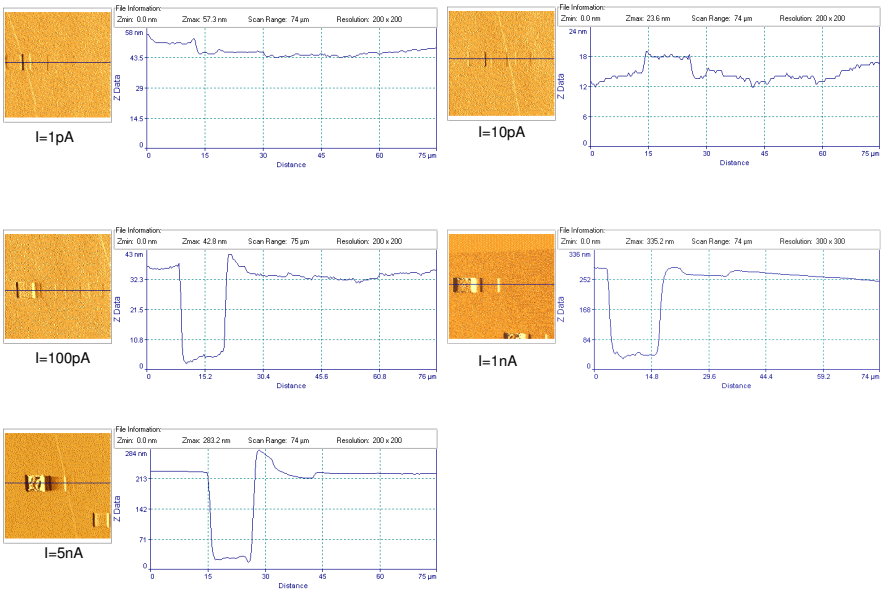

Figure 3.9: AFM measurements and line scans of the structured patterns in silicon.

In fig. 3.10 AFM images are shown with determined roughness values $R_a = \frac{1}{N}\sum_{i=1}^{N}|Z_i - \bar{Z}|$ and $RMS = \sqrt{\frac{1}{N-1}\sum_{i=1}^{N}(Z_i - \bar{Z})^2}$ of patterns with $Z(Si) =$

100 nm for different currents and $Z(GaAs) = 100$ nm which is the nominal depth in gallium arsenide, for $I = 5$ nA. Note also the depths $Z(AFM)$ measured by AFM. They are not equal to $Z(Si)$ as the pitch width was again kept constant for the various currents resulting in a deviation of the real depth from the nominal one, cf. section 3.2.1.

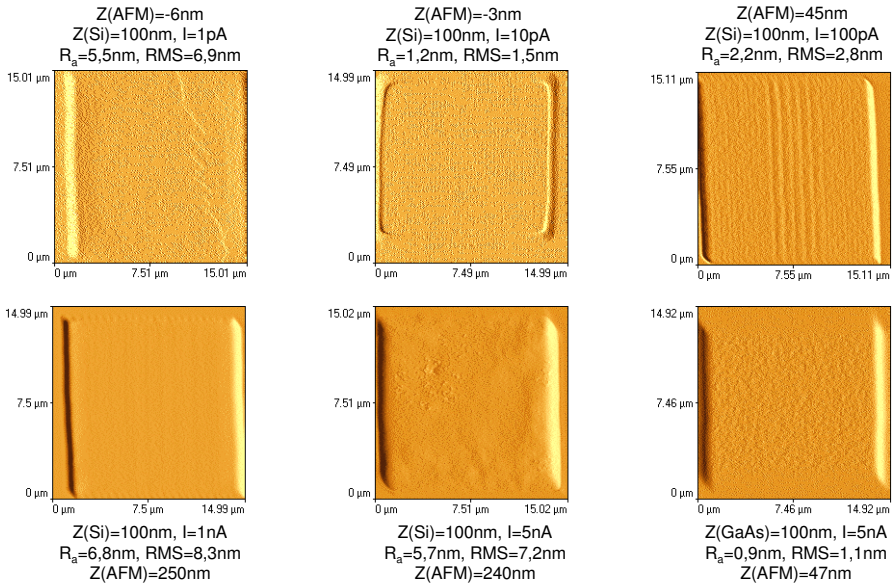

Figure 3.10: AFM measurements: depth and roughness values for structured patterns in silicon.

The roughness values were measured in an area of about 7 x 7 µm^2. They are larger for higher ion doses, except for the lowest dose at an ion current of 1 pA which is probably a measurement artefact.
It can be seen from fig. 3.9 that a minimum dose is necessary to create holes instead of hills. The reason is that the ions expand a material, before milling it. The dose for rendering the interaction zone amorphous is reported to be about 10^{14} cm^{-2}, the minimal dose for getting holes in silicon with 30 keV Au^+ ions to be about 26 x 10^{14} cm^{-2} [42]. Amorphous material always has a smaller density than the corresponding crystalline one which is the reason why the interaction zone expands. The reported minimal dose for milling silicon is lower than what was found out in the course of this work using Ga^+ ions. For $I = 100$ pA and $Z(Si) = 100$ nm, which corresponds to a dose of 880 x 10^{14} cm^{-2}, a clear milling effect can be seen from the AFM measurement, while for $I = 1$ nA and $Z(Si) = 10$ nm, which corresponds to a dose of 440 x 10^{14} cm^{-2}, a milling effect is not yet visible.

Fig. 3.11 shows the measured depth of structures against the applied dose. The depth was measured for the structures in fig. 3.10. For comparison, also the results of [42] with Au^+ ions are shown.

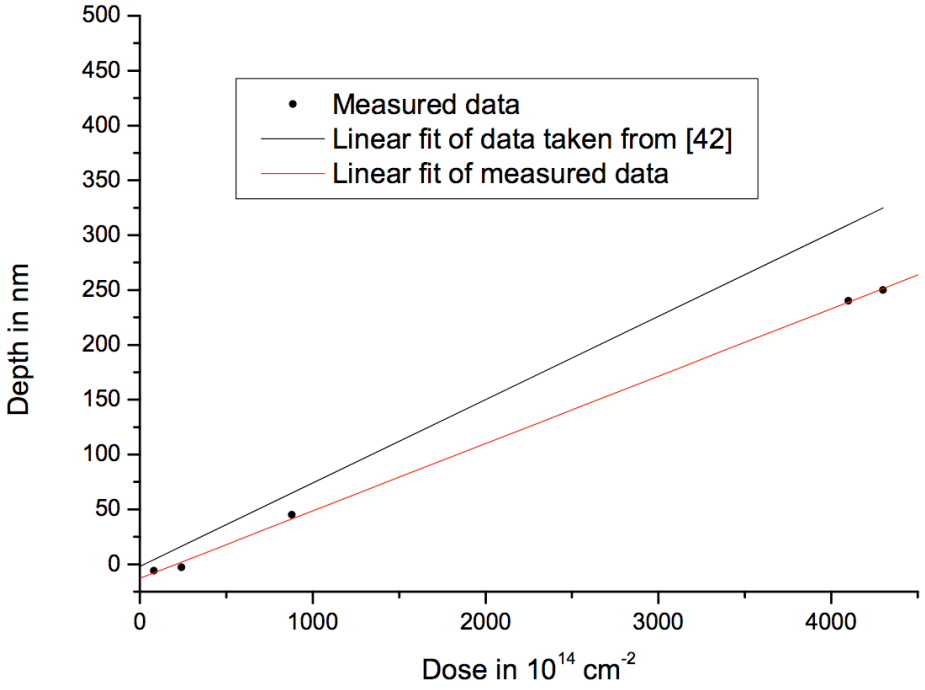

Figure 3.11: Depth of structures in silicon versus the applied dose.

The aim of structuring silicon was actually to arrange metal droplets in nanopores and to grow whiskers out of them. Fig. 3.12 shows several patterns before and after the evaporation of gold. The gold rate was 0.1 Å/s and the evaporation time 10 min at a substrate temperature of 550 °C. All patterns were structured with a dwell time of 30 µs per point and with an ion current of 30 pA.

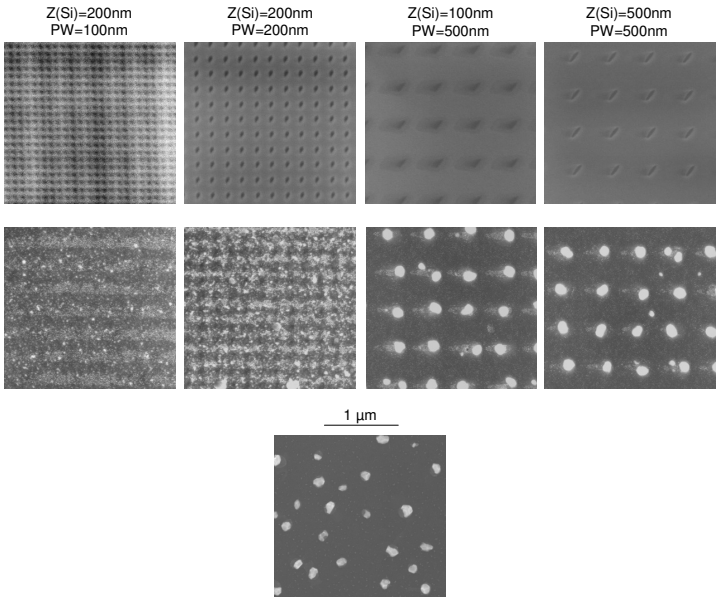

Figure 3.12: Structured areas on silicon. Top: before gold evaporation, middle: after gold evaporation, bottom: gold distribution on a non-structured area of the sample.

It can be seen that the critical parameter for ordering metal droplets is not the depth or the exact circular form of the holes but the pitch width which should correspond more or less to the natural distance of the droplets. This distance can be influenced by the substrate temperature and gold rate during evaporation which will be shown in detail in chapter 5.

Si(111) with a 5 nm AlN layer

Si(111) covered by a 5 nm AlN layer was structured with holes as described in the previous section and with a mesh of perpendicular lines to obtain islands of AlN on Si(111). This was done in the course of a cooperation with Forschungszentrum Jülich where we got the samples from. The aim was the growth of ordered arrays of gallium nitride nanowhiskers. The growth was also performed in Jülich. The growth results will be described in chapter 5. Fig. 3.13 shows the mesh structuring result. The distance between the single lines was 1 µm and the nominal depth $Z(Si)$ in silicon 200 nm.

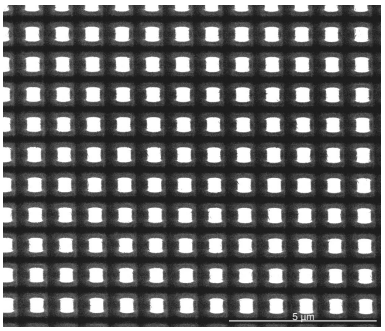

Figure 3.13: Mesh structure on Si(111) with a 5 nm AlN layer.

Si(111) with a 20 nm AlN layer and a 5 nm Si layer

For the same cooperation, a Si(111) substrate with a 20 nm AlN layer and a 5 nm Si layer on top was structured as well, shown in fig. 3.14. The distance between the single lines was 1 µm and the nominal depth in silicon for one pattern 10 nm, and for a second one 20 nm.

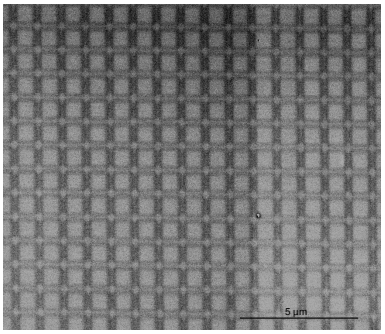

Figure 3.14: Mesh structure on Si(111) with a 20 nm AlN layer and a 5 nm Si layer.

3.2.3 Germanium

The experiments to structure germanium were the same as for silicon. Fig. 3.15 corresponds to fig. 3.9 and shows AFM measurements of structured germanium.

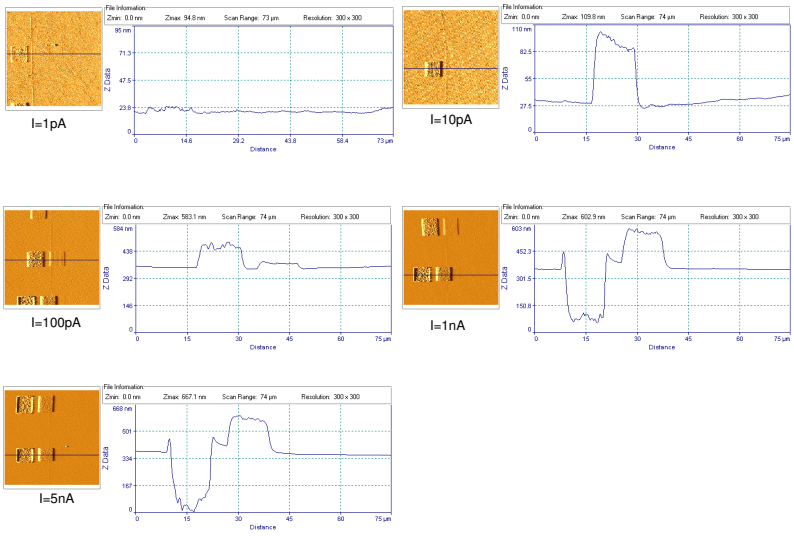

Figure 3.15: AFM measurements and line scans of the structured patterns in germanium.

Fig. 3.16 corresponds to fig. 3.10 and shows depth and roughness values for structured patterns in germanium.

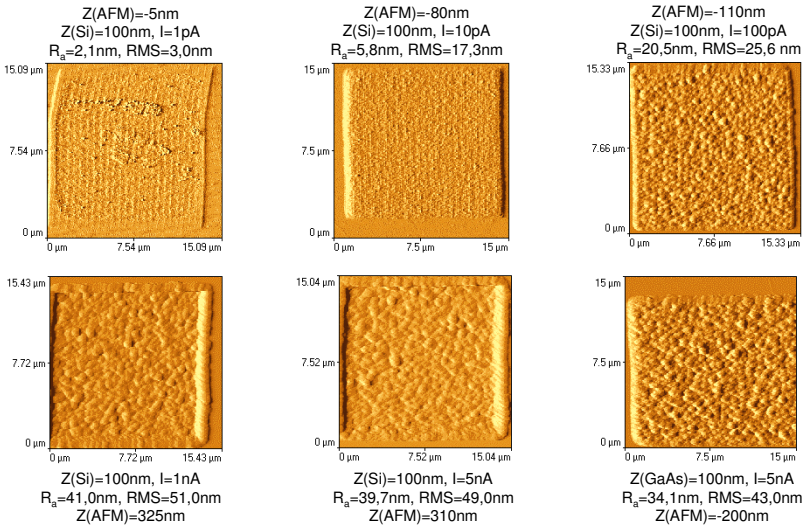

Figure 3.16: AFM measurements: depth and roughness values for structured patterns in germanium.

Higher doses lead – as in the case of silicon – to larger roughness values. It is striking that all roughness values are larger than in the case of silicon. Yanagisawa et al. [43] report about nanoporous structure formations on germanium surfaces by focused ion beam irradiations. No such reports can be found for silicon. But also the depth dependence on the ion dose looks completely different from the one for silicon. This is shown in fig. 3.17 on which the measured values of figs. 3.15 and 3.16 are plotted.

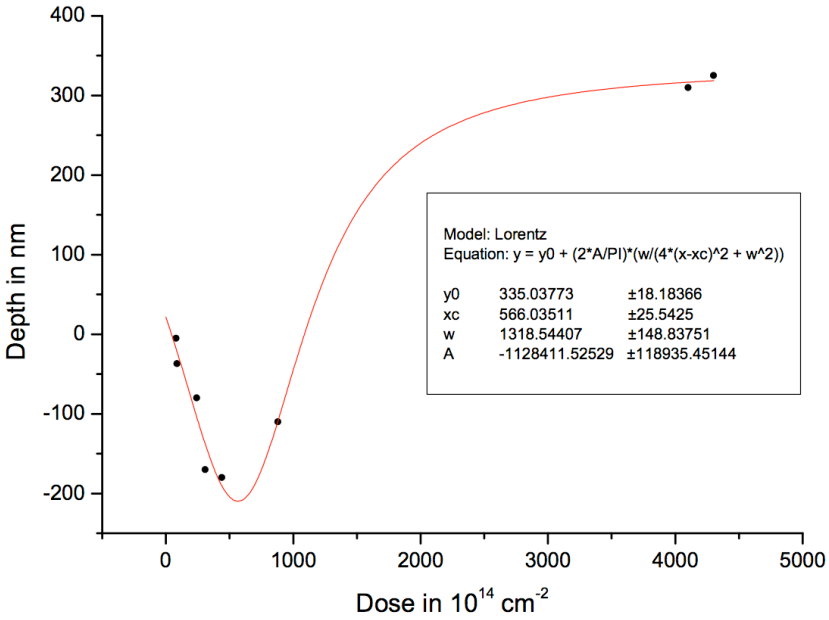

Figure 3.17: Depth of structures in germanium versus the applied dose.

It is assumed that in the case of germanium a larger depth range can be examined using the same doses compared to silicon. Thus, at low doses, only a small part is amorphous, than a larger one before material is milled. At higher doses, a linear correlation is found between dose and depth similar to the behavior on silicon. At very high doses, a saturation effect seems to occur, cf. fig. 3.7.

In germanium as well, patterns were created to enable an arrangement of metal droplets in nanopores. This is shown in fig. 3.18, analog to fig. 3.12 for silicon.

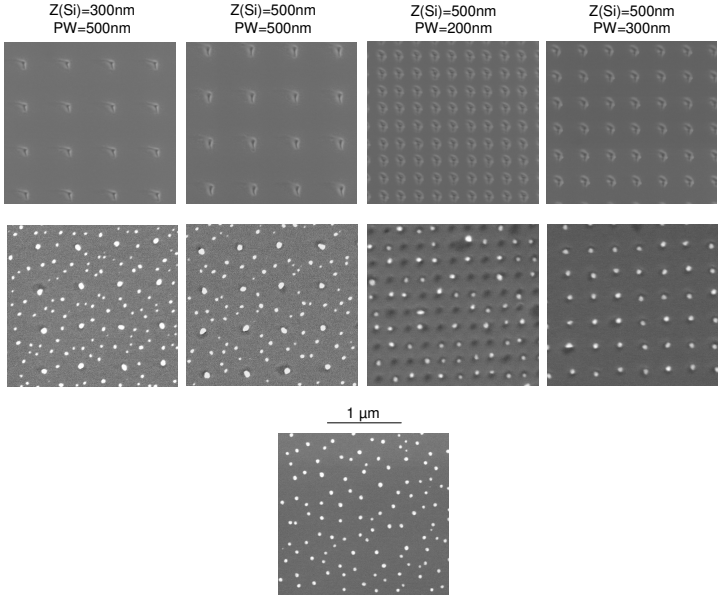

Figure 3.18: Structured areas on germanium. Top: before gold evaporation, middle: after gold evaporation, bottom: gold distribution on a non-structured area of the sample.

As for silicon, the critical parameter for ordering droplets was found to be the distance of the nanopores.

After having presented the equipment and the methods for substrate structuring here, the following chapter will deal with the characterization techniques used in this work.

Chapter 4

Characterization methods

In this chapter, the characterization methods of electron microscopy, atomic force microscopy and x-ray reflectometry used for sample characterization will be presented.

4.1 Electron microscopy

4.1.1 Scanning electron microscopy

Scanning electron microscopy (SEM) is a method to examine sample surfaces. All samples for this thesis were measured by an FEI Nova 600 NanoLab dual beam system, cf. chapter 3. A typical SEM setup is shown in fig. 4.1. In a microscope, the wavelength limits the resolution. De Broglie postulated the following wavelength for matter particles [44]:

$$\lambda = \frac{h}{p} = \frac{h}{mv} \tag{4.1}$$

with h being Planck's constant, p the momentum, v the velocity and m the mass of the particle. Thus, the wavelength of 10 keV electrons is 0.12 Å. However, this limit is not reached in an electron microscope because of the various lens errors.
In an SEM, electrons are emitted from an electron source which can either be a hot cathode, i.e. a heated wire, or a field emission gun in which a high electrical field causes the emission of electrons from a tungsten tip, cf. the emission of ions for FIB in chapter 3. The acceleration voltage of the electrons is in the range of 2-30 kV. The beam is focused on the sample surface by several electromagnetic lenses, instead of the electrostatic lenses used in

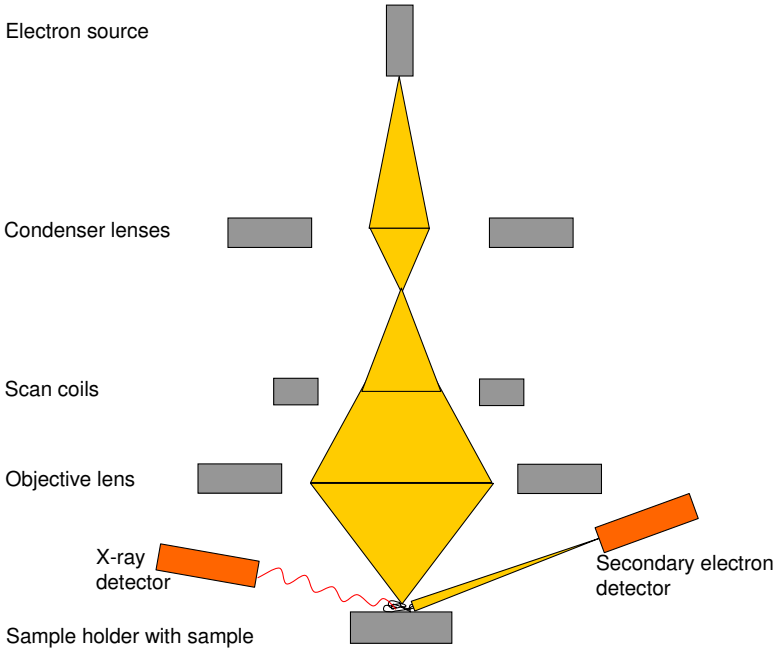

Figure 4.1: Sketch of an SEM setup.

the case of ions. Electrostatic lenses change the velocity of the electrons and have a very small refractive power.
The condenser lenses in an SEM form the beam and their apertures constrict it by eliminating high-angle electrons.
The scan coils deflect the beam and make it scan over a rectangular area of the sample.
The objective lens focuses the beam onto the region of interest.
As for ions, cf. chapter 3, spherical and chromatic aberration as well as astigmatism are lens errors limiting the resolution of the SEM.
The interaction volume of the electron beam in the sample has a pear-like shape, see fig. 4.2 bottom. The higher the energy of the electrons and the lower the atomic number of the investigated material, the larger the size of the interaction volume. The electrons interact with the sample in various ways which can be seen in fig. 4.2 at the top.

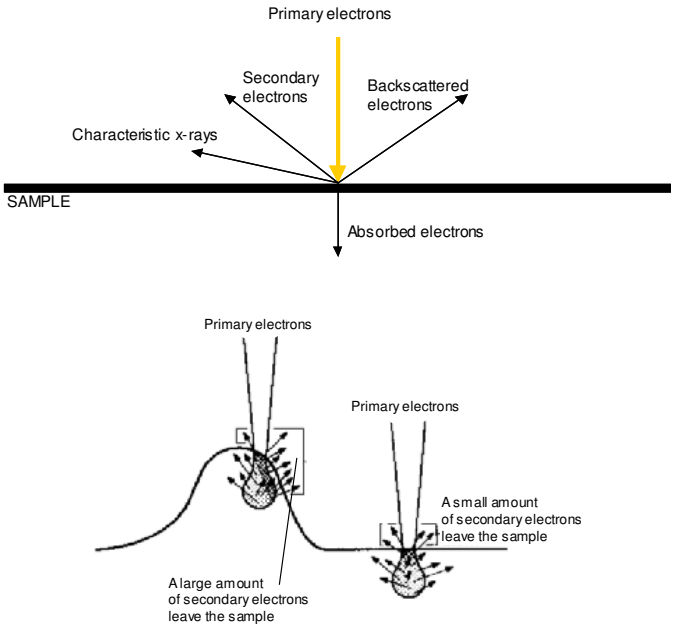

Figure 4.2: Top: The most important interactions of incident electrons with a sample surface. Bottom: Behavior of secondary electrons at different morphologies, taken from [45].

These interactions are detected in different ways. The most widely used mode is secondary electron (SE) detection. Secondary electrons are emitted from the sample surface by energy absorption from the incident primary electrons. Because of their relative small energy in the range of some eVs, they are only able to leave the upper zone of the interaction volume. The amount of secondary detected electrons at a certain point of the scanned rectangle determines the gray scale value corresponding to that point in the created image. This value depends on the angle of the incident beam. Edges are brighter due to the larger amount of emitted secondary electrons.
In contrast to secondary electrons, backscattered electrons have higher energies in the range of some keVs. A second detector is thus necessary with a larger solid angle of collection. The backscattered electron contrast is used to detect different materials because it is highly dependent on the atomic number of the investigated material. The brightness increases with the atomic number.
Characteristic x-rays which leave the sample due to the electron bombard-

ment are detected by a silicon crystal doped with lithium. The photons generate electron-hole pairs in the crystal which correspond to their energy. Thus, the energy distribution of the x-rays can be measured. The spatial resolution for energy dispersive x-ray analysis (EDX) amounts to about 1 micron because of the high photon energy.
More details about SEM can be found in [46] and [47].

4.1.2 Transmission electron microscopy

Transmission electron microscopy (TEM) is analog to classical microscopy with electron beams instead of light. The electron source is the same as for SEM but now the source is used to illuminate the whole area of interest instead of scanning the area point by point. The acceleration voltage for the electrons ranges from some tens of kV up to over 1 MV. The transilluminated sample is imaged with an electromagnetic lens system analog to a light optics lens system. Detectors are either phosphorous or photographic screens or CCDs. The sample has to be very thin so that multiple scattering cannot occur. The resolution g is about 0.2 nm. This can be calculated using Abbe's formula [48]:

$$g = \frac{\lambda}{2n \cdot \sin \alpha} \tag{4.2}$$

n is the refraction index of the medium, for the vacuum in the TEM, this is about 1, and α is half of the aperture angle of the lens. Although the wavelengths of light and electrons in a TEM (cf. equation 4.1) differ by a factor of at least 50000, the resolution increases for electrons only by a factor of 1000 because of lens errors, as already mentioned above.

Different contrast modes

There are several interactions between beam and sample which contribute to the image in the TEM. The sample should be so thin that it is transparent for the electron beam. For imaging, elastically scattered electrons are used. The most important contrast is the diffraction contrast. For crystalline samples, there are certain directions in which the electrons are diffracted. They are determined by Bragg's equation:

$$n \cdot \lambda = 2d \cdot \sin \theta \tag{4.3}$$

n is a natural number, d is the lattice spacing of the crystal and θ the diffraction angle. A sketch for deriving this equation is given in fig. 4.3.

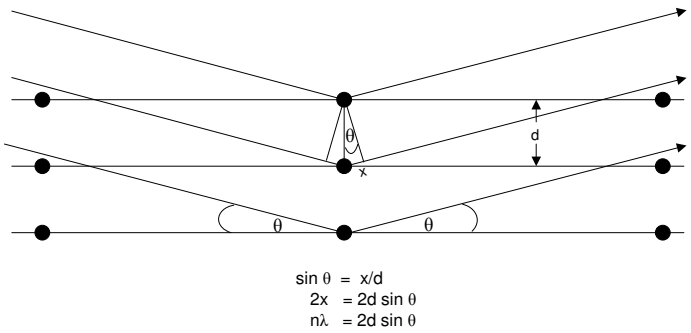

Figure 4.3: Sketch for the derivation of Bragg's equation.

The crystal structure can be deduced from the diffraction contrast.
A second mode is bright and dark field imaging. In the bright field mode, an aperture allows only the direct beam to pass and all points at which the beam is diffracted are dark in the image. In the dark field mode, one diffracted beam is selected which leads to an image on which only the points in this special direction are bright.
A third contrast is the phase contrast on which high-resolution TEM is based. In this mode of operation, diffracted beams are interfered in the image plane resulting in a contrast pattern correlated to the crystal lattice.
The amplitude contrast gives information about the composition of the sample as electrons are scattered more at parts of sample with higher atomic number.

All measurements for this thesis have been performed using a JEOL JEM-2200FS TEM.
The cross sections have been prepared according to the common procedure found in [49].

More detailed description of TEM can be found in [47] and [50].

4.2 Atomic force microscopy

Atomic force microscopy (AFM) means scanning a surface with an atomically thin tip. The setup of the AFM is shown in fig. 4.4.

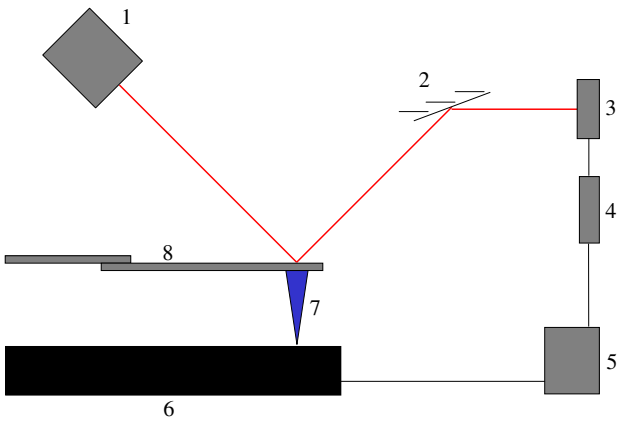

Figure 4.4: Setup of the AFM

The following components are shown:
1: Laser
2: Mirror
3: Photo diodes
4: Amplifier
5: Control unit with piezo crystal
6: Sample
7: Tip
8: Cantilever

The tip atoms feel the effect of a force induced by the atoms of the sample, cf. fig. 4.5. At small distances, these forces are repulsive, at larger ones they are attractive.

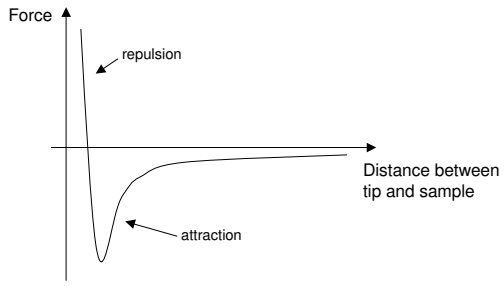

Figure 4.5: Force-distance-curve.

To determine the deflection of the tip caused by the force, a laser beam is bent to a cantilever to which the tip is attached. The beam is then reflected onto a mirror from where it is directed to an array of photo diodes. Their signals are proportional to the force felt by the tip. This information is then transferred to a piezo sensor which in the used most constant force mode subsequently adjusts the distance between the tip and the sample so that the force between the atoms is always constant. Thus, from the movements induced by the piezo sensor, information is received about the topography of the sample.

All AFM measurements for this theses have been performed using a Topometrix SPM device. The data analysis has been carried out using the SPM-Lab V 3.06.06 software.

Dependence of the picture quality on the tip shape

Fig. 4.6 shows micrographs of silicon germanium structures measured once with a new tip and once with an old one and SEM images of the corresponding tips.

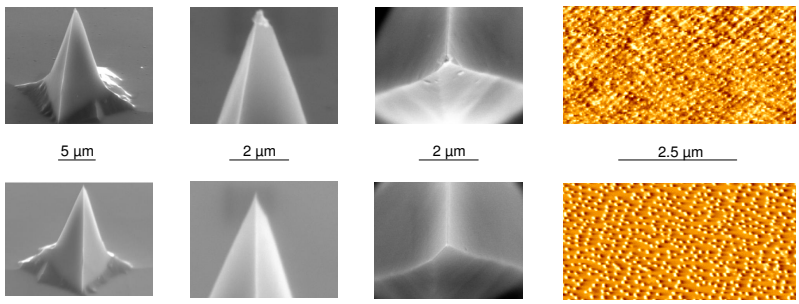

Figure 4.6: SEM images of a broken (top) and a new tip (bottom) as well as a sample measured by them.

The reason why the tip plays such an important role in image quality is intuitively clear but can also be shown mathematically.
Fourier transformation is used for developing a function in a complete system of orthogonal functions. It is defined as follows:

$$F(k) = \frac{1}{2\pi} \int_{-\infty}^{+\infty} f(x) \exp(-ikx) dx \tag{4.4}$$

$F(k)$ is called the Fourier transform of $f(x)$.

For image editing, Fourier analysis is also applied. Instead of displaying the gray value of each point of the picture, the whole image is described by a superposition of gray value fluctuations. To obtain the Fourier transform of the image, the Fourier transform of the sample surface has to be multiplied by the one of the tip.
Multiplication of two Fourier transforms $F(k)$ and $G(k)$ in k-space means a convolution of the two functions $f(x)$ and $g(x)$ in position space. This is defined as follows:

$$(f * g)(x) = \int f(\xi) \cdot g(x - \xi) \, d\xi \tag{4.5}$$

The image obtained by an AFM measurement can be expressed as follows:

$$Image_{AFM}(x, y) = (S * T)(x, y) = \int \int S(\xi, \eta) \cdot T(x - \xi, y - \eta) \, d\xi d\eta \tag{4.6}$$

$S(x, y)$ is the surface function of the sample und $T(x, y)$ the function of the tip. The ideal function for the tip is thus a delta function:

$$Image_{AFM}(x, y) = \int \int S(\xi, \eta) \cdot \delta(x - \xi, y - \eta) \, d\xi d\eta = S(x, y) \tag{4.7}$$

In such a case, the AFM image would correspond exactly at each point (x, y) to the surface of the sample.

4.3 X-ray reflectometry

To determine the layer thickness of a material deposited on a substrate, x-ray reflectometry can be applied. The basic principle of this method is the reflection of x-rays at low incident angles. It can be applied to layers of 2-500 nm with a typical accuracy of better than 1 nm.

Theoretical basics

X-rays at an incident angle α at the interface of two materials with refractive indices n_1 und n_2 are partly reflected and partly transmitted, cf. fig. 4.7.

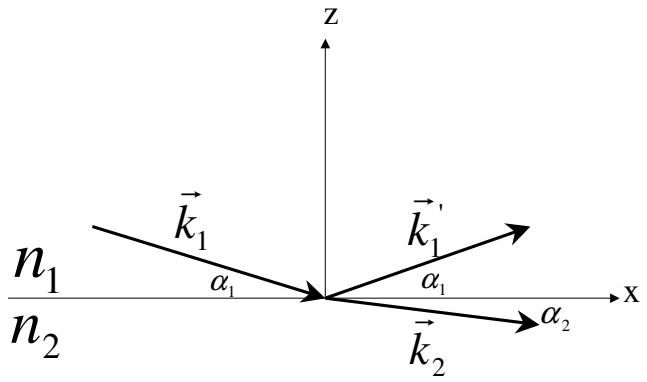

Figure 4.7: Reflection and transmission of an electromagnetic wave with wave vector $\vec{k_1}$ incident at the interface layer of two materials with refractive indices n_1 and n_2.

Reflection and transmission coefficients are expressed by the Fresnel equations (see e.g. [51]) as functions of the refractive indices of the concerned materials and the incident angle α.
To determine the dependence of the refractive index on various material properties, the approach is made that radiation in interaction with a medium excites forced damped oscillations of the electrons in the solid which results in electromagnetic radiation of the accelerated charges. This so-called oscillator model [52] results in the following formula for the refractive index:

$$n = 1 - \delta + i\beta \tag{4.8}$$

δ describes the refraction, β the absorption. In good approximation (far from

absorption edges) δ can be written as:

$$\delta = r_0 \frac{\lambda^2}{2\pi} \rho(\overrightarrow{r}) \tag{4.9}$$

with r_0 being the classical electron radius (≈ 2.8 x 10^{-15} m), λ the wavelength of the used x-rays and $\rho(\overrightarrow{r})$ the electron density. Thus, reflectivity is a function of the electron density and consequently also of the mass density.
At angles smaller than α_c, according to Snell's law, total internal reflection occurs:

$$1 - \delta = \cos \alpha_c \approx 1 - \frac{\alpha_c^2}{2} \tag{4.10}$$

Thus, α_c is approximately $\sqrt{2\delta}$. As the values of δ are typically in the range of 10^{-6}–10^{-5} in the x-ray regime, reflection from a surface occurs only at rather small incidence angles.
The thickness t of a measured layer is obtained by the interference of the reflected x-rays at the surface of the layer and the interface between substrate and layer. For a single layer, intensity oscillations are obtained which in good approximation are separated by:

$$\Delta\alpha = \frac{\lambda}{2t} \tag{4.11}$$

Surface and interface roughness have an influence on the reflectivity as well, which is described by a parameter σ, which is the root mean square deviation from a medium location of the interface.
For several layers, there is a recursion formula for the reflectivity, introduced by Parratt in 1954 [53].

More detailed description can be found in chapter 3 of [54].

Measurements

The measurements were performed at a commercial high-resolution x-ray diffractometer (GE Inspection technology). The characteristic $K\alpha_1$ x-ray radiation of copper with a wavelength of 0.154 nm is used. Depending on the sample, typical entrance and detector slits of 0.2 mm are applied leading to an angular resolution at the detector of $r(2\alpha)$=$5{\cdot}10^{-4}$ rad = 0.03° which is sufficient for analyzing layer structures with thicknesses smaller than 300 nm (eq. 4.11).

Analysis of spectra

For spectrum analyzing, the program "Parratt 32" is used [55]. In this program, a model which describes the spectrum best is detected by varying the different influences on the spectrum. Fig. 4.8 shows an example of a spectrum with simulation curve.

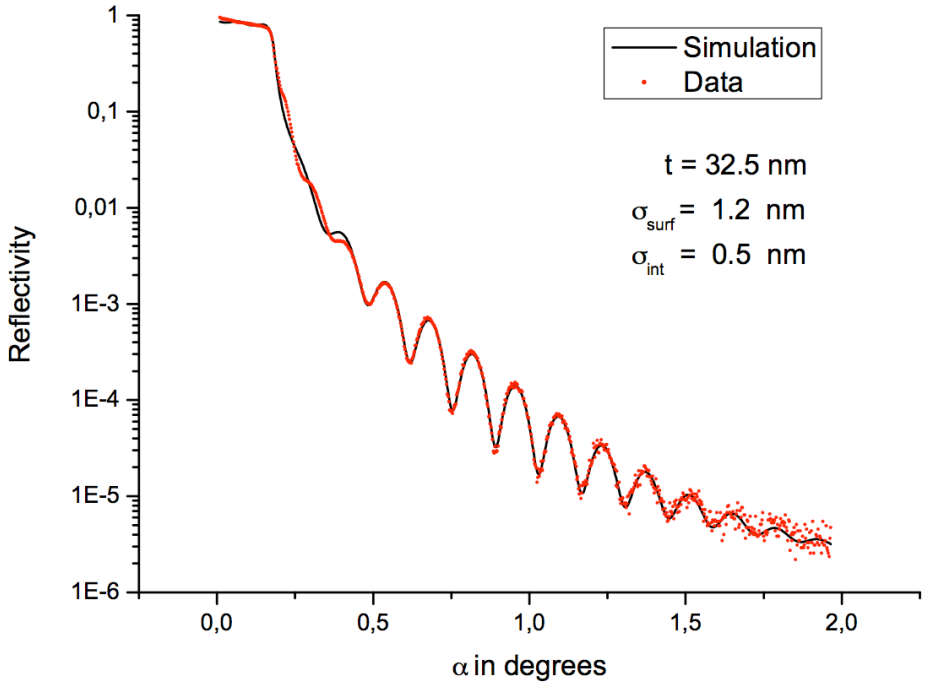

Figure 4.8: Typical reflectometry spectrum against the incident angle α and the simulation with the results for thickness and roughnesses.

The Parratt model gives information about the layer thickness, the number of layers, the density of the layer material and the interface and surface roughness.

After having presented the characterization methods in this chapter, the following chapter presents the experimental results of nanowhisker growth and the discussion.

Chapter 5

Experimental results and discussion

This chapter presents the results of our experiments and discusses them based on the thermodynamics considered in chapter 1.
As the whiskers are grown by the VLS mechanism, cf. chapter 1, it is essential to investigate droplet formation in detail. Especially the differences when applying different solvents will be considered. The first part of this chapter deals, therefore, with the results of droplet formation of gold and indium on silicon substrates.
The second part presents the results of silicon and germanium nanowhisker growth. Silicon nanowhiskers are mostly grown from gold droplets. No other solvent for the growth of nanowhiskers has been investigated more thoroughly. That is the reason why gold is very suitable for fundamental research if practical application is not the most important aim. But how gold is incorporated into the whisker and thus its influence on the electronic properties of the whisker is still a matter of discussion in the literature [56, 57, 58]. Gold is a deep-level defect in bulk silicon [59] and if this is also true for nanowhiskers grown from gold droplets, an alternative metal for the growth would be necessary. For this reason, apart from gold we also applied indium as a solvent for the growth. Indium has already been used in silicon technology, see e.g. [60], and would therefore be a good alternative in comparison to gold.
Germanium was chosen as a second nanowhisker material because of its similarities to silicon in many aspects. It is therefore suitable for a comparison to silicon. Some fundamentals regarding the growth of nanowhiskers, especially the growth direction, can be deduced from this comparison. The experiments on germanium have been performed with gold as the solvent.
In the last sections of this chapter, the results of growth of SiGe heterostructures and of the arrangement of nanowhiskers will be presented and discussed.

5.1 Droplet formation on Si(111)

Gold droplets on Si(111)

The following figures show the influence of the experimental parameters of evaporation rate R, evaporation time t, substrate temperature T, desorption and annealing on the size and distribution of gold droplets. Desorption means an annealing step of about 10 min at 850 °C before substrate processing with the objective of cleaning the sample of a thin oxide layer. This oxide layer can form during handling the sample in spite of the preceding hydrogen-termination, cf. chapter 2.
These results will be discussed in more detail after having presented the results of indium droplets on silicon as well for having the possibility of drawing a comparison.

Rate:

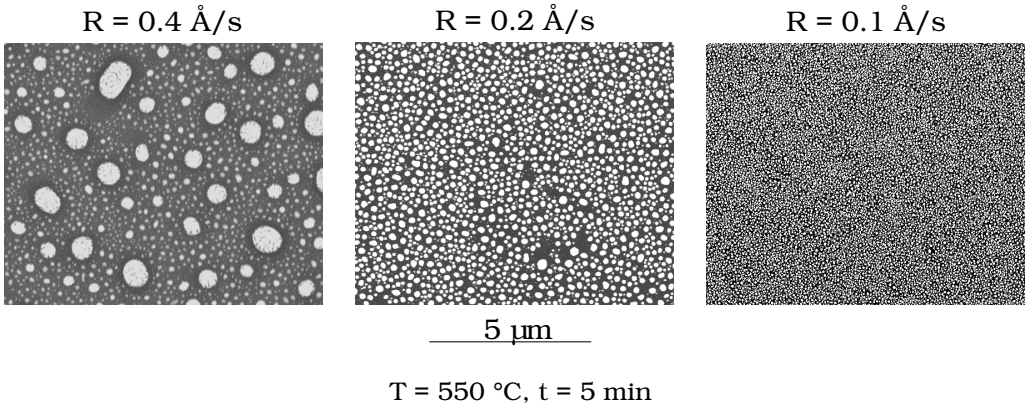

Figure 5.1: Gold droplets on silicon. Influence of evaporation rate.

A higher rate results in smaller distances between the arriving gold particles and in coalescence of the gold droplets forming larger ones.

Evaporation time:

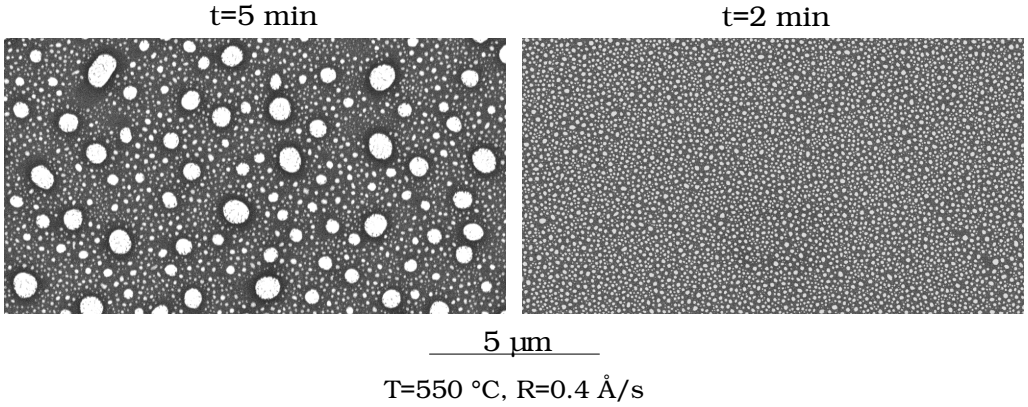

Figure 5.2: Gold droplets on silicon. Influence of evaporation time.

A longer evaporation time has the same effect on droplet formation as a higher rate and leads to coalescence of the gold droplets.

Substrate temperature:

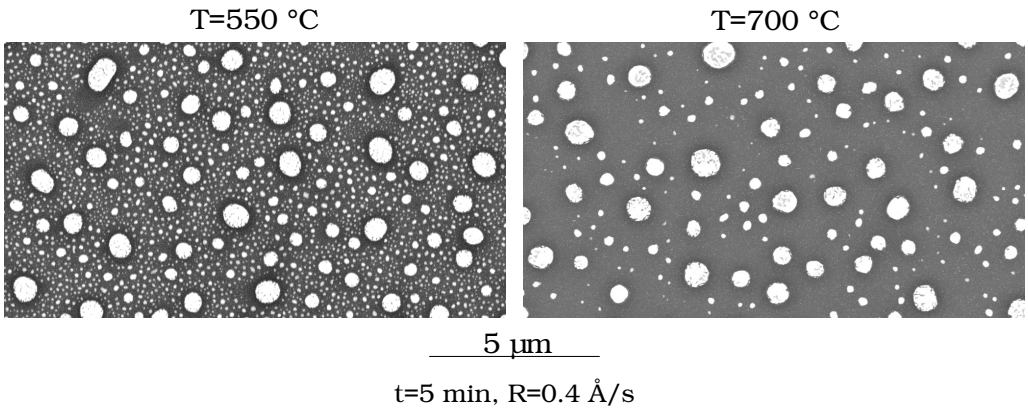

Figure 5.3: Gold droplets on silicon. Influence of substrate temperature.

Larger droplets form at a higher substrate temperature. Their distribution is more homogenous.

Oxide desorption step:

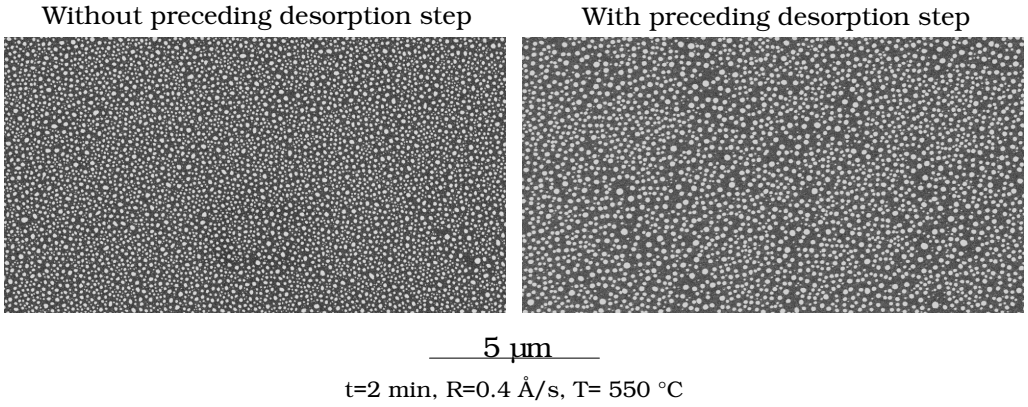

Figure 5.4: Gold droplets on silicon. Influence of preliminary oxide desorption.

A preceding oxide desorption step has no significant influence on the formation of gold droplets on the silicon substrate.

Annealing:

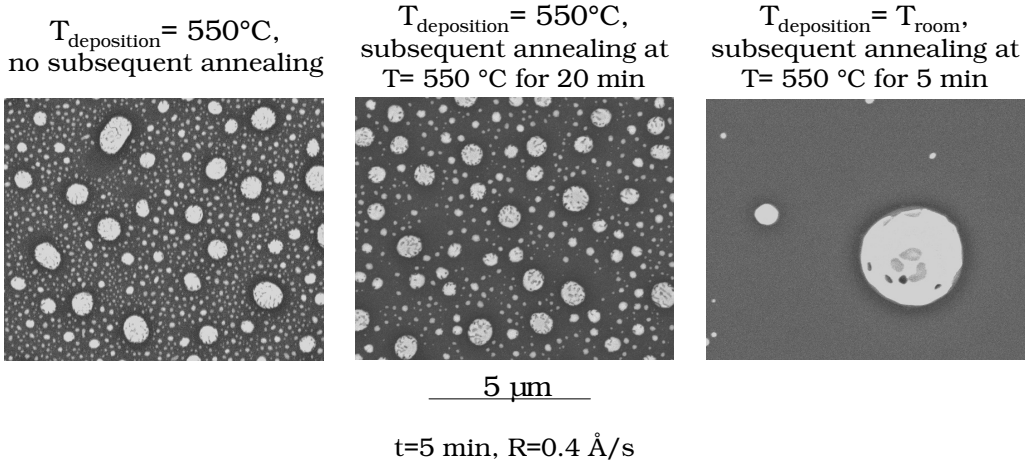

Figure 5.5: Gold droplets on silicon. Influence of temperature during evaporation and annealing.

Annealing at the same temperature at which the deposition has taken place has no influence on droplet formation. However, deposition at room temperature and subsequent tempering at 550 °C leads to large droplets with large distances in-between.

Indium droplets on Si(111)

The above described experiments for gold were also performed with indium. The influence of the experimental parameters are shown in the following before discussing the difference behavior of gold and indium on a silicon substrate.

Rate:

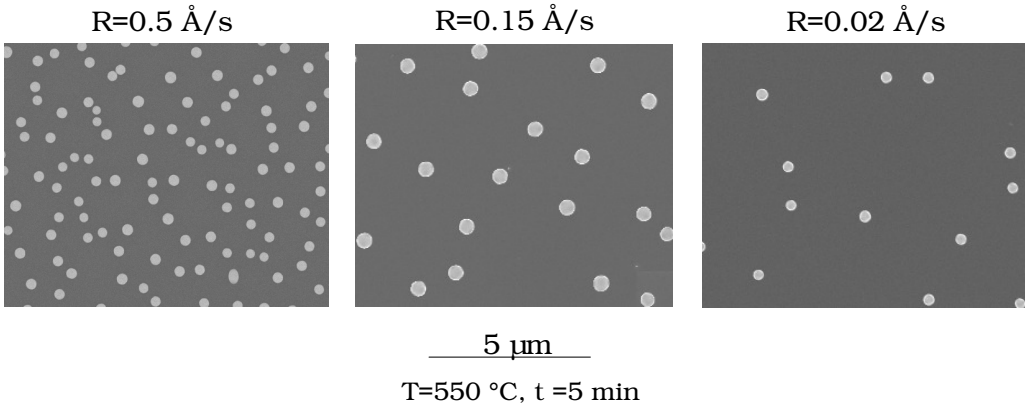

Figure 5.6: Indium droplets on silicon. Influence of evaporation rate.

A higher evaporation rate leads in the case of indium to a smaller distance between the droplets.

Evaporation time:

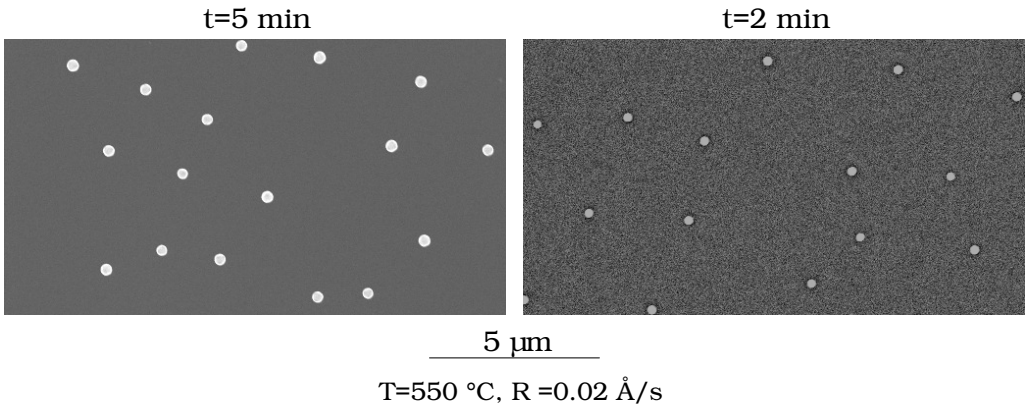

Figure 5.7: Indium droplets on silicon. Influence of evaporation time.

A longer evaporation time leads to larger droplets with the same distribution on the substrate.

Substrate temperature:

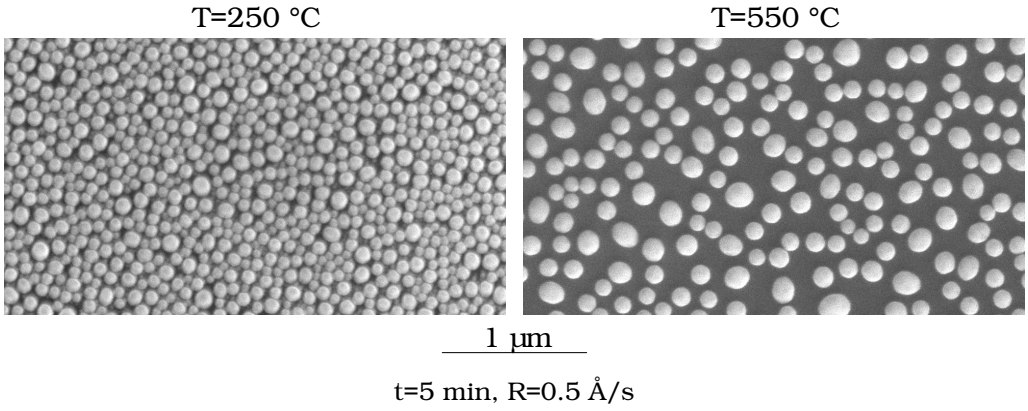

Figure 5.8: Indium droplets on silicon. Influence of substrate temperature.

Larger droplets with larger distances in-between form at a higher substrate temperature.

Oxide desorption step:

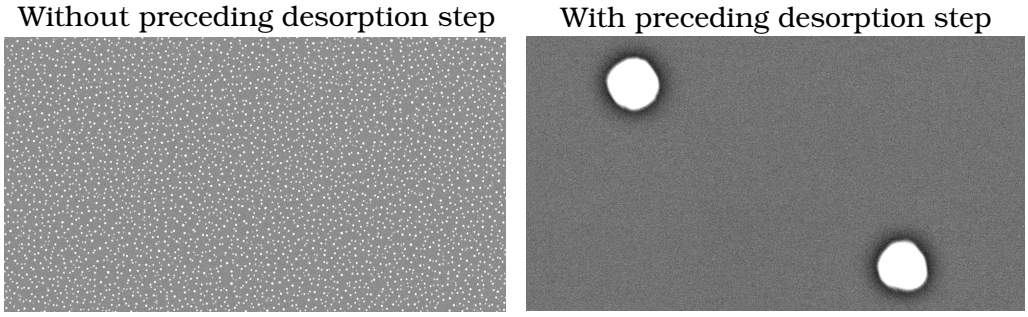

Figure 5.9: Indium droplets on silicon. Influence of preliminary oxide desorption.

A preceding oxide desorption step has a significant influence in the case of indium and leads to larger indium droplets with large distances in-between.

Annealing:

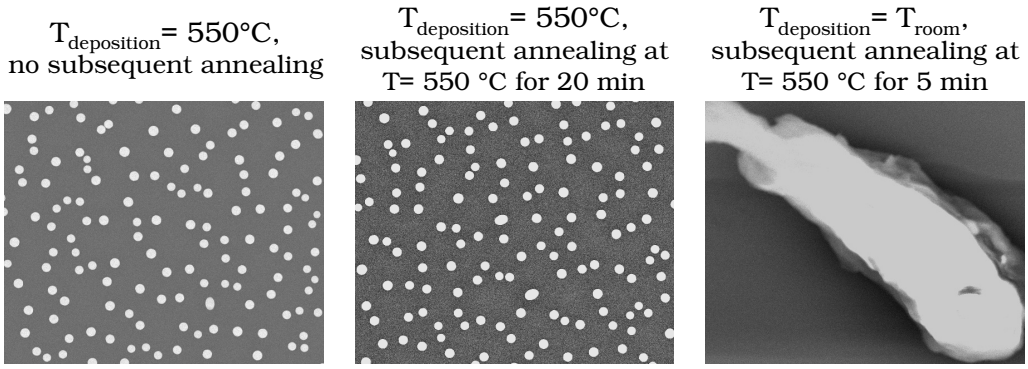

Figure 5.10: Indium droplets on silicon. Influence of temperature during evaporation and annealing.

As in the case of gold, annealing at the same temperature at which the deposition has taken place has no influence on droplet formation. Deposition at room temperature and subsequent tempering at 550 °C, however, leads to a few large indium deposits.

Discussion of the results of gold and indium droplet formation on Si(111)

The behavior of gold and indium on a silicon substrate has been investigated with regard to the influence of metal evaporation rate, evaporation time, substrate temperature, substrate pre-processing and tempering.
In contrast to indium, gold seems to form a wetting layer on the "non-desorbed" substrate, i.e. it interacts strongly with the substrate. This is also expected from the phase diagrams Au-Si and In-Si in figs. 1.4 and 5.11 which show that the solubility of silicon in gold at our deposition temperatures is about 20 mole% whereas the solubility of silicon in indium is less than 1 mole%.

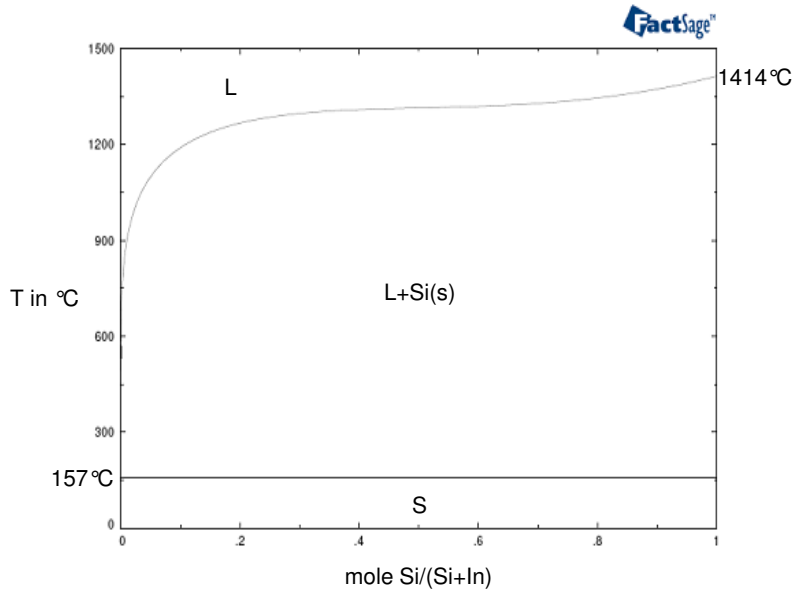

Figure 5.11: Phase diagram In-Si.

The interaction between gold and the silicon substrate can also be clearly seen in fig. 5.12 in which gold droplets and indium droplets on silicon are shown. The surface of the gold droplets after cooling down contains silicon whereas the indium droplets do not show any traces of silicon. The wetting angle of the gold droplets is much smaller than the one of the indium droplets. The gold rate amounted to 0.4 Å/sec, the indium rate to 0.5 Å/sec, the substrate temperature was 550 °C in both cases and the evaporation time 10 min. The samples were annealed for 20 min after metal deposition.

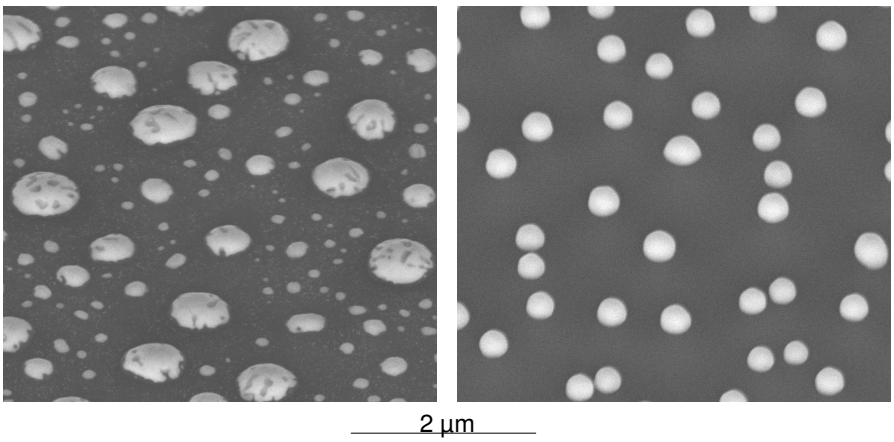

Figure 5.12: Tilted view of droplets on silicon. Left: gold droplets with dissolved silicon from the substrate, right: indium droplets without any silicon traces.

TEM measurements confirmed the existence of a wetting layer in the case of gold, cf. fig. 5.13.

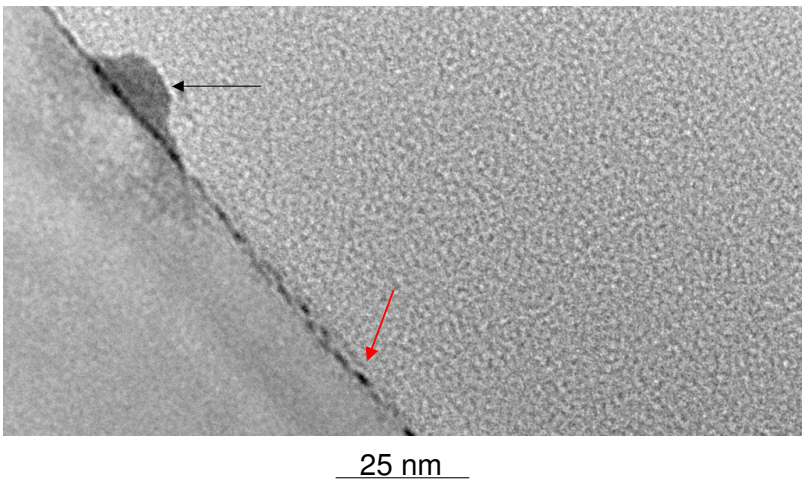

Figure 5.13: TEM image of a sample with gold droplets. The black arrow indicates a small droplet, the red one a part of which is interpreted as the wetting layer.

Considering the influence of rate, evaporation time and substrate temperature, the differences between gold and indium are clearly visible: A higher rate leads to a smaller distance between the arriving atoms because they have not enough time to diffuse and to coalesce before another atom arrives nearby. This can be seen very clearly in the case of indium. The gold atoms are in some way connected to each other because of the wetting layer and consequently one atom arriving nearby is incorporated into an already existing droplet. The same happens if the evaporation time is longer. Using indium, this results in larger droplets with the same distribution as the diffusion remains the same. At higher substrate temperatures, the diffusion is enhanced, and that means for indium larger droplets and a larger distance between them. For gold, the droplets become larger as well and in the space between them, the smaller ones disappear due to the higher mobility. Tempering at the same temperature at which the deposition has taken place has no influence either in the case of gold or in the case of indium. But depositing at room temperature and subsequent tempering at 550 °C leads in the case of gold to large droplets with quite large distances and in the case of indium to huge deposits of some tens of microns with distances of over 500 microns. It is probable that in both cases the small droplets which form at room temperature evaporate during heating because of the Gibbs-Thomson effect. For indium, this effect should be stronger because the single droplets are not connected by a wetting layer. The deposits of indium probably form only sporadically because of some anomalies of the surface. The biggest difference between gold and indium has been observed in connection with the oxide desorption step: The gold droplet distribution was seen to be the same with or without desorption whereas the indium droplet distribution was totally different after performing this step. To explain differences in droplet formation between indium and gold, the effects of different diffusion coefficients of gold and indium on silicon, the solubility of substrate atoms in the two metals, the surface tension of gold and indium and the surface energy of silicon and silicon oxide will be considered. The diffusion coefficients at temperatures around 550 °C for indium and gold on a clean Si(111) surface are 0.30 and 0.12 m^2/s, respectively [61, 62]. They are of the same order of magnitude and thus cannot account for the very different experimental results on a clean Si(111) substrate, i.e. after the desorption step.
In spite of the preceding HF-dip, a thin oxide layer probably forms during insertion of the sample into the UHV chamber . There are hints in the literature [63] that the deposition of gold onto a thin layer of SiO_2 on the top of Si(111) favors the decomposition of SiO_2, i.e. that gold contributes to cleaning the surface. This could explain why the gold distribution is similar with or without the desorption step. Unfortunately, no literature data about

the enhancement of dissolution of a silicon oxide layer by indium were found. From the phase diagrams In−Si and Au−Si, it can be seen that the solubilities of silicon in gold and indium at the applied growth temperatures are as already mentioned about 20 and less than 1 mole%, respectively. It can be argued that also the solubilities of SiO_x in gold and indium are significantly different, and thus that indium does not enhance the decomposition of an oxide layer. If this is actually the case, the indium distribution will then depend on whether a desorption step has been applied or not.
Now the role of surface tension and surface energy of the different components of the experiment will be discussed. From the phase diagram Au−Si, a liquid Au−Si alloy with a silicon concentration of about 20 mole% can be expected at the applied growth temperatures. For this concentration, Naidich et al. [64] found a surface tension of about 1.0 J/m^2 at 1500 °C. No data could be found in the literature for the surface tension of indium−silicon alloys. However, as the solubility of silicon in indium at our growth temperature is less than 1 mole%, the surface tension of pure indium is taken as an approximation which is 0.6 J/m^2 at its melting point (157 °C) [65]. As the surface tension of most liquids decreases linearly with increasing temperature [66], there is a wide difference between the surface tension of the Au−Si alloy and the In−Si alloy at the applied growth temperatures. Since the state of the substrate surface after desorption and the vacuum conditions are the same during evaporation of gold and indium, the different liquid−solid−vapor interface dynamics can be ascribed to the surface tension of the solvent. Liquids with high surface tension tend to form droplets with a small contact area with the underlying substrate whereas liquids with lower surface tension tend to wet the substrate. This could explain the formation of smaller droplets in the case of gold than in the case of indium on a bare silicon surface, i.e. after the desorption step.
Without desorption step, indium forms smaller droplets which can be explained by the different surface energies of silicon and silicon oxide. The surface energy of silicon at its melting temperature (1410 °C) is 0.9 J/m^2, and it decreases in a linearly with increasing temperature [65], i.e. it is higher than 0.9 J/m^2 at our growth temperatures. As the exact composition of the surface after inserting the sample into the growth chamber is not known, data of similar surfaces from the literature are taken as an approximation. Asay and Kim [67] expect the surface energy of a not exactly specified silicon oxide surface to be higher than 0.1 J/m^2 at room temperature. Janczuk and Zdziennicka [68] determined the surface energy of quartz in the temperature range from 200 to 1000 °C and found out that it changed only slightly from 0.19 to 0.18 J/m^2. This indicates that the surface energy of silicon oxide is lower than the surface energy of silicon. This is not surprising if one considers

a crystalline silicon surface and an amorphous oxide surface. This explains why the bare silicon tends to minimize the free surface by maximizing the contact area between indium and silicon. This leads to larger droplets compared to those on the silicon oxide surface.
The size and distribution of gold and indium droplets obtained on the silicon surface may therefore be reasonably explained considering the influence of solubilities and surface energies on the mechanism of formation of droplets with or without the desorption step.

5.2 Silicon nanowhisker growth

Having examined the influence of the experimental parameters on droplet formation, this section deals with the results of silicon nanowhisker growth on Si(111).

Gold as the solvent

Very regular nanowhiskers in the [111] direction (fig. 5.14) were obtained on the samples on which gold was used as the solvent.

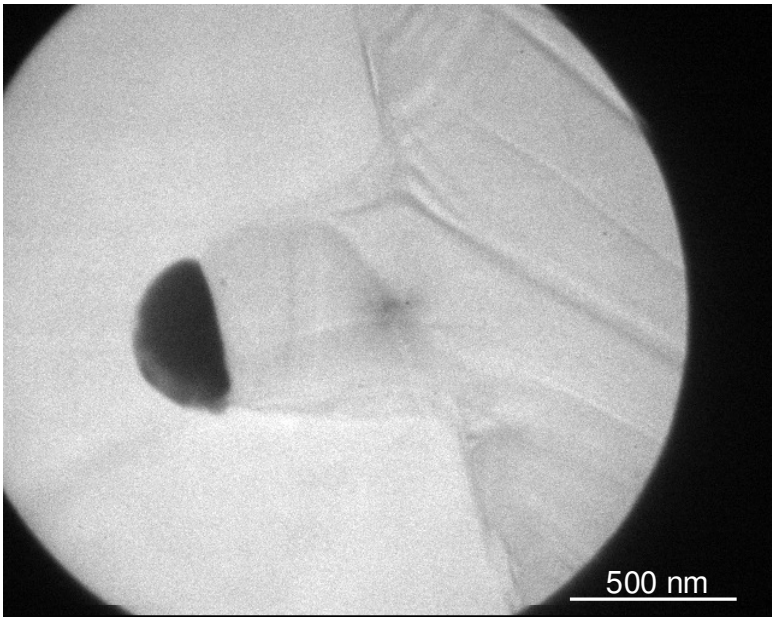

Figure 5.14: TEM image of a whisker grown from a gold droplet on Si(111).

The following results show unambiguous correlations between the experimental parameters and the whiskers grown. The experiments with gold as the solvent were well reproducible.

The first experiment was performed in order to determine the correlation between droplet and whisker distribution. For this reason, fig. 5.15 shows two samples with gold evaporated at a rate of 0.4 Å/s for 10 s on the substrates

at 550 °C after a desorption step at 850 °C. On one of the samples, silicon was evaporated for 150 min at a nominal rate of 0.5 Å/s thereafter.

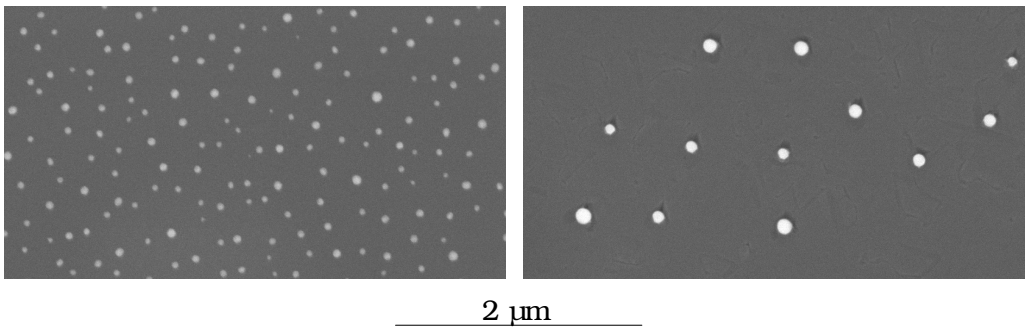

Figure 5.15: Left: gold droplets on silicon, right: silicon nanowhiskers on silicon.

The number of nanowhiskers is obviously smaller than the number of the gold droplets. The diameters of the whiskers is larger than the one of the droplets.

In the following, the influence of different parameters on the outcome of the experiment will be shown.

Silicon rate:

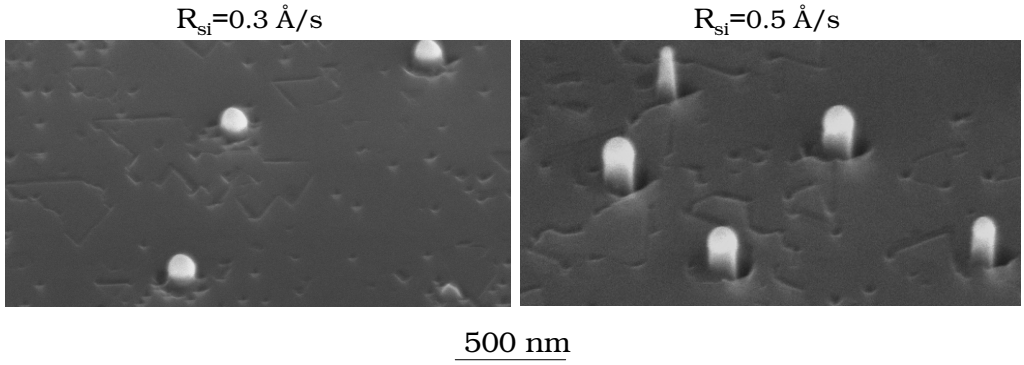

Figure 5.16: Silicon nanowhiskers on silicon. Influence of evaporation rate.

A higher silicon evaporation rate leads to longer nanowhiskers and a higher density.

Evaporation time:

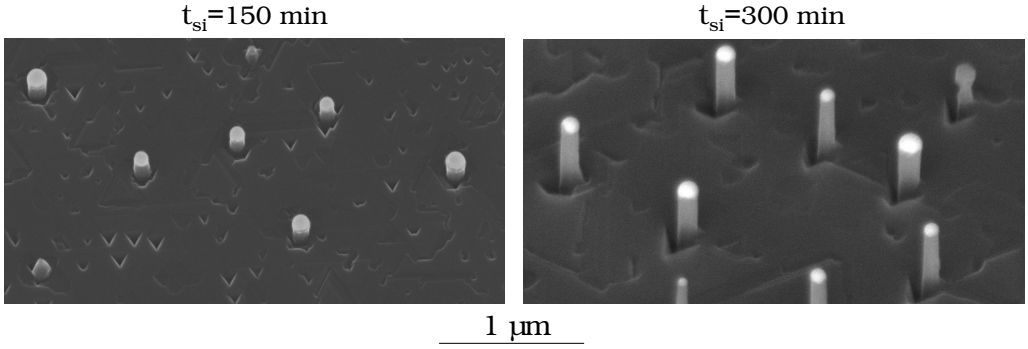

Preceding desorption, T=550 °C, R_{Au}=0.4 Å/s, t_{Au}=10 s, R_{Si}=0.5 Å/s

Figure 5.17: Silicon nanowhiskers on silicon. Influence of evaporation time.

A higher evaporation time leads to longer nanowhiskers as well. However, the density remains the same in this case.

Substrate temperature:

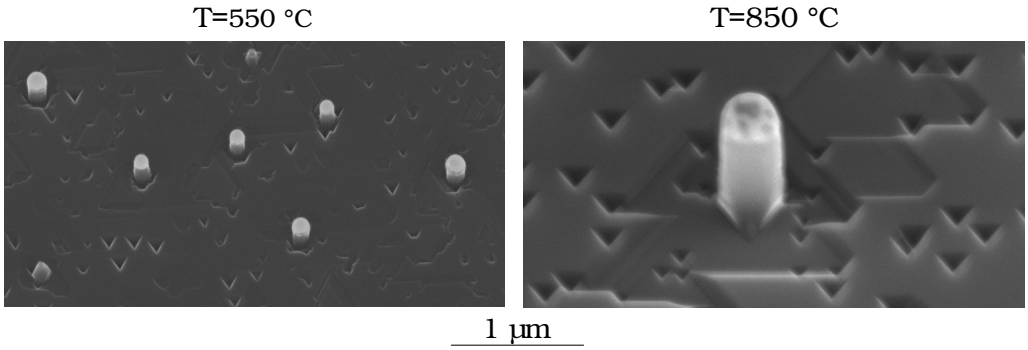

Preceding desorption, R_{Au}=0.4 Å/s, t_{Au}=10 s, R_{Si}=0.5 Å/s, t_{Si}=150 min

Figure 5.18: Silicon nanowhiskers on silicon. Influence of substrate temperature.

Thicker nanowhiskers are obtained at a higher substrate temperature.

Oxide desorption step:

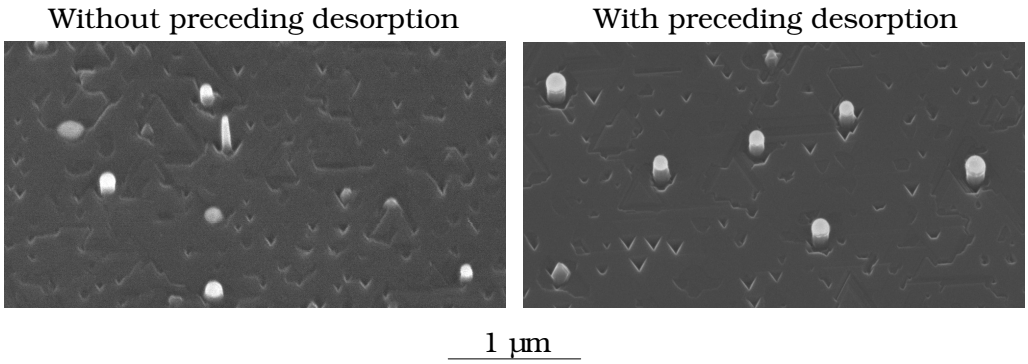

T=550 °C, R_{Au}=0.4 Å/s, t_{Au}=10 s, R_{Si}=0.5 Å/s, t_{Si}=150 min

Figure 5.19: Silicon nanowhiskers on silicon. Left: without preceding desorption step, right: with preceding desorption step.

Nanowhisker growth is possible without oxide desorption step as well. However, better results are obtained when performing it.

As already mentioned in chapter 1, in addition to the whiskers, a silicon layer is always obtained on the whole substrate when applying PVD. The length of the whiskers and the thickness of the layer were investigated for different samples by imaging cross sections in the SEM. One example of such an image can be seen in fig. 5.20.

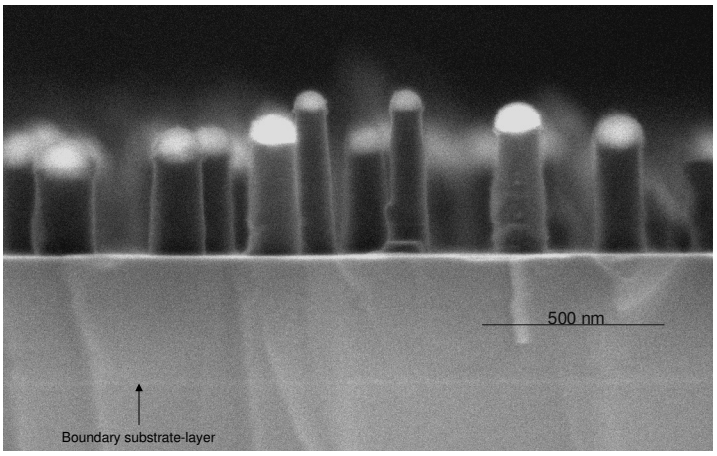

Figure 5.20: Cross section image of silicon nanowhiskers on silicon with a clearly visible boundary between substrate and layer.

Table 5.1 lists the results of those measurements, indicating the parameters of the different samples as well.

T in °C	R_{Au} in Å/s	t_{Au} in s	R_{Si} in Å/s	t_{Si} in min	$l_{whiskers}$ in nm	$\rho_{whiskers}$ in $\frac{1}{\mu m^2}$	d_{layer} in nm
550	0.4	10	0.3	150	35	0.70	140
550	0.4	10	0.5	150	130	1.19	200
550	0.4	10	0.5	300	270	1.10	350
850	0.4	10	0.5	150	470	0.04	225

Table 5.1: Length $l_{whiskers}$ and density $\rho_{whiskers}$ of whiskers and thickness of the layer d_{layer} as a function of the parameters of the experiment.

The density of whiskers was always homogeneous. Thus, it could be determined by counting the whiskers of an SEM image with low magnification.

When describing the VLS mechanism, one usually simplifies the explanation and suggests that a whisker emerges from every metal droplet. However, in the first experiment with gold as the solvent, in which droplet distribution and whisker distribution were compared, more and smaller gold droplets before silicon evaporation were counted than whiskers thereafter. The whisker density on the sample is lower and the droplets on their tops are larger compared to the original ones. One explanation could again be the fact that gold diffusion is quite high in silicon at our growth temperatures [69] and that silicon has a high solubility in gold as already described above.
It was shown that also without preceding desorption, whisker growth is possible for gold. This supports the theory that the behavior of gold on silicon is not affected by a thin oxide layer.

In the following, the results concerning length and density of whiskers as well as thickness of the layer, as summarized in table 5.1, will be discussed:
It is striking that a lower whisker density is obtained at a lower silicon rate although the gold droplet distribution had been the same as for the higher rate. As can be seen in fig. 5.21, some whiskers seem to have stopped growing at an early stage.

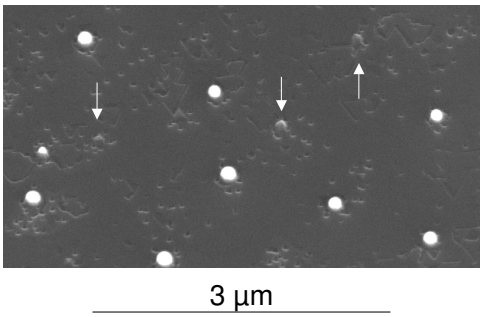

Figure 5.21: SEM image of not completely developed whiskers, indicated by white arrows.

It is plausible to assume that whisker growth from some droplets did not occur at all. The higher the rate, the higher the whisker density as the supply of silicon atoms reaches more gold droplets before growing on the substrate between them and building a layer. This is also reflected in the whisker lengths: At a rate increase by a factor of about 1.5, the thickness of the layer between the whiskers changes by a factor of about 1.4 but the length of the whiskers by a factor of 3.7. At double evaporation time, the density of whiskers is somewhat less and the length/layer ratio larger. But as the parameters are never completely stable, it can be assumed that at double evaporation time, layer and whiskers have double thickness and length, respectively. At higher substrate temperature, the mobility of the atoms is enhanced and the whiskers are longer than the thickness of the layer. The density of the whiskers is lower at higher temperatures which has already been seen in relation to the droplet formation.
It can be easily derived from the values in table 5.1 that the nominal silicon rate $R_{Si}(nom)$, determined at the beginning of this work (cf. chapter 2), was not reached during those experiments. Table 5.2 shows again a part of table 5.1 and the real reached rate which was calculated by considering the volume of the whiskers and of the layer as well as the silicon evaporation time:

$$R_{Si}(calc) = \frac{\pi r_{whiskers}^2 \cdot l_{whiskers} \cdot \rho_{whiskers} \cdot A + d_{layer} \cdot A}{A \cdot t_{Si}} \tag{5.1}$$

A, the area of the sample, can be canceled.

$R_{Si}(nom)$ in Å/s	t_{Si} in min	$l_{whiskers}$ in nm	$r_{whiskers}$ in nm	$\rho_{whiskers}$ in $\frac{1}{\mu m^2}$	d_{layer} in nm	$R_{Si}(calc)$ in Å/s
0.34 ± 0.03	150	35	75	0.70	140	0.16
0.47 ± 0.03	150	130	75	1.19	200	0.22
0.47 ± 0.03	300	270	75	1.10	350	0.20
0.47 ± 0.03	150	470	225	0.04	225	0.25

Table 5.2: R_{Si} calculated for the experiments presented in table 5.1

It can be clearly seen that the rate is not the one expected. One reason is certainly that $R_{Si}(nom)$ was determined by x-ray reflectometry of a layer which was deposited at room temperature and thus did not grow crystalline on the substrate. The average density of those layers was found to be 80 % of the density of silicon. Thus, layers deposited at high temperature which are crystalline should have 92 % of the thickness of layers deposited at room temperature. This could explain the result of a lower rate when depositing at high temperature. But this error is too small to account for the differences between real and nominal rate.
Another reason could be a decrease of rate with time. The x-ray reflectometry measurements for determining the rate were performed before starting any experiment, i.e. with a completely new electron beam evaporator. The data in table 5.2 was obtained from experiments performed after the evaporator had been used about 45 times except the data in the third row which was obtained after about 80 experiments. After 110 experiments using electron beam evaporation, another reflectometry measurement was completed in order to determine the actual rate. It was found to be 0.09 Å/s at an emission current of 130 mA. Fig. 5.22 shows the decrease of rate with time, the rates obtained by x-ray reflectometry at room temperature were decreased to 92 %.

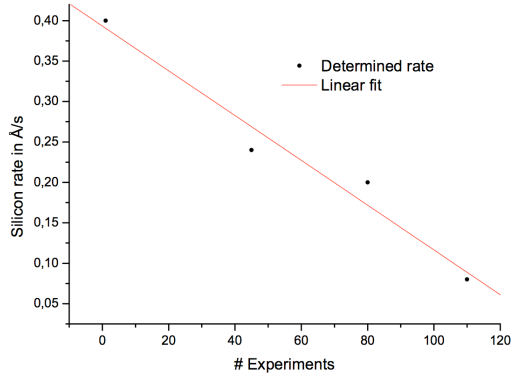

Figure 5.22: Change of silicon rate with time.

The straight line does not fit exactly. The reason is that the number of experiments does not always correlate with the amount of evaporated silicon. But it is obvious that the rate decreases with time. This can be due to the fact that after a certain length of operation, the silicon block has a hole at the place where silicon is evaporated by the electron beam. Then shadowing effects occur. We have seen that higher silicon rates and higher temperatures improve the whisker/layer ratio but neither the rate nor the temperature could be further increased in our equipment.

Another important point which is not included in table 5.2 – the lengths being average values – is that thinner whiskers are longer, i.e. growing faster than thicker ones. The model of Dubrovskii et al. which was already described in section 1.2.4, explains in detail the role of diffusion on whisker growth by PVD and derives also growth velocities for different radii and lengths of whiskers as well as for different distances between them. As most of the whiskers are smaller than 1 µm and the diffusion length λ_f on the whisker sides is probably very high as the whiskers do not grow laterally, the assumption $\frac{L}{\lambda_f} \ll 1$ seems to be reasonable. λ_s, the diffusion length on the surface of the substrate, is the adjustable parameter of the model as the active nucleation of islands and their growth on the substrate surface tend to decrease its value. It can be determined by comparing theory and experiment. In our case, we assume $\frac{R_w}{\lambda_s} \gg 1$ because for nanowhiskers which have more or less the same radius, R_w is half of the average spacing between them, which is in our case always larger than 800 nm. On the other hand, λ_s seems to be very small because we always get a quite thick layer, i.e. the adatoms have a small diffusion length before growing on the sample. For this case, Dubrovskii et al. calculated formulas for the limits $\frac{R}{\lambda_s} \gg 1$

$$\frac{L}{H} = \epsilon - \gamma + \frac{2\lambda_s}{R} \tag{5.2}$$

and $\frac{R}{\lambda_s} \ll 1$

$$\frac{L}{H} = \epsilon - \gamma + \frac{2\lambda_s^2}{R^2 ln\frac{\lambda_s}{R}} \tag{5.3}$$

The second case differs radically from the classical diffusion dependence $L(R) \propto \frac{1}{R}$.
To find out if eq. 5.2 or eq. 5.3 is valid for our results, whiskers of the sample shown in fig. 5.23 have been evaluated.

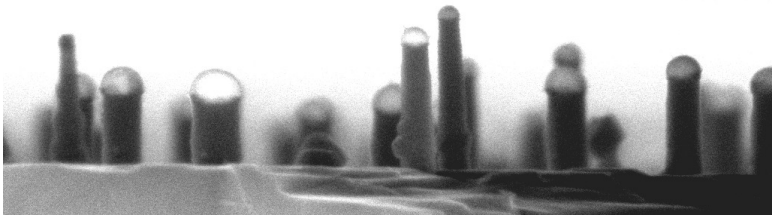

Figure 5.23: Sample used to find out the L-R dependence.

The overall thickness of the deposited material of the investigated sample was 360 nm which corresponds to H in formulas 5.2 and 5.3. $\epsilon = 1 - \frac{V_s}{V} = 1 - \frac{H_s}{H}$, with H_s being the thickness of the layer between the whiskers, in the considered case 350 nm, i.e. $\epsilon = 0.03$. γ, accounting for the desorption of atoms from the droplet surface, is not known and thus like λ_s variable in the fit process. Fig. 5.24 shows whisker lengths against whisker radius, a linear fit and a fit according to equation 5.2.

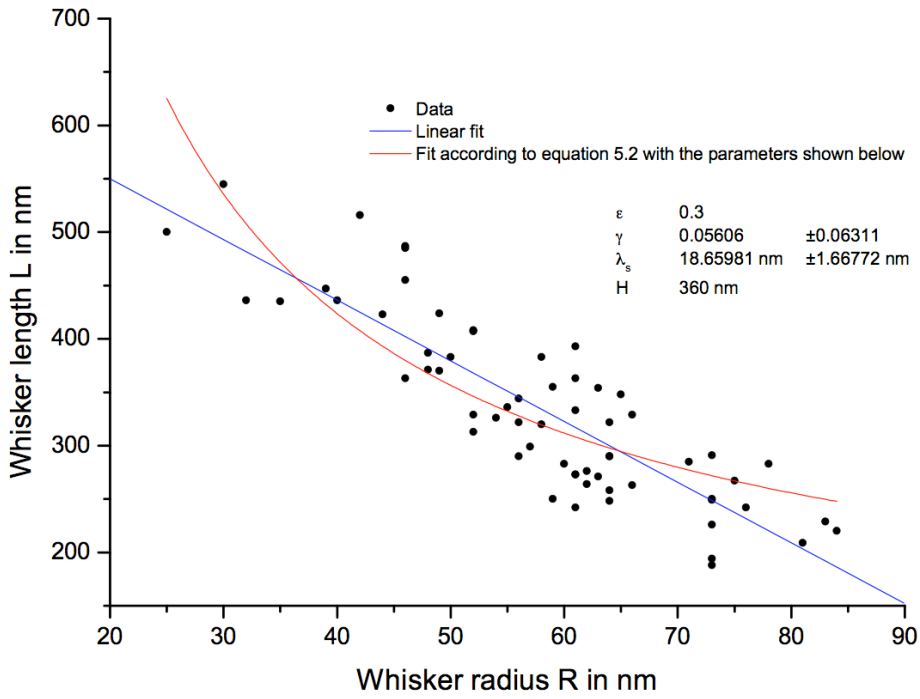

Figure 5.24: Whisker length dependence on whisker radius.

For the second case $R \ll \lambda_s \ll R_w$ considered by Dubrovskii and described in equation 5.3, there was no fit possible. Our data values are widely dispersed, thus it is not clear if the diffusion behavior in our experiments can be described by eq. 5.2 or by a linear function. $\lambda_s \approx 20$ nm, assuming the diffusion behavior can be described by eq. 5.2. To compare this value to our experimental results, fig. 5.25 is considered in which the whisker diameter is about 150 nm. The extension of the depleted zone around the whisker is about 50 nm and has the same order of magnitude as the fitting parameter λ_s.

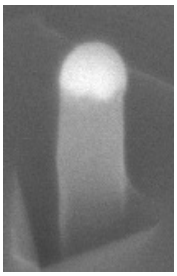

Figure 5.25: Whisker with depleted zone around.

Our results showing that thinner whiskers grow faster than thicker ones are in good agreement with the results of Schubert et al. [70] for MBE growth of whiskers under similar conditions. From their data, they concluded that the whisker length is inversely proportional to its diameter. The Gibbs-Thomson effect, cf. chapter 1, does not seem to play a role for whiskers with diameters of about 100 nm or more.

Indium as the solvent

As expected from the results of droplet formation, the behavior of indium as solvent material for nanowhisker growth is completely different than the one of gold.
The first significant difference is the fact that it was not at all possible to grow nanowhiskers from indium when the oxide desorption step had not been performed.
When it had been performed, whisker growth occurred only sporadically in the not completely closed silicon layer between the large droplets, which is shown in fig. 5.26.

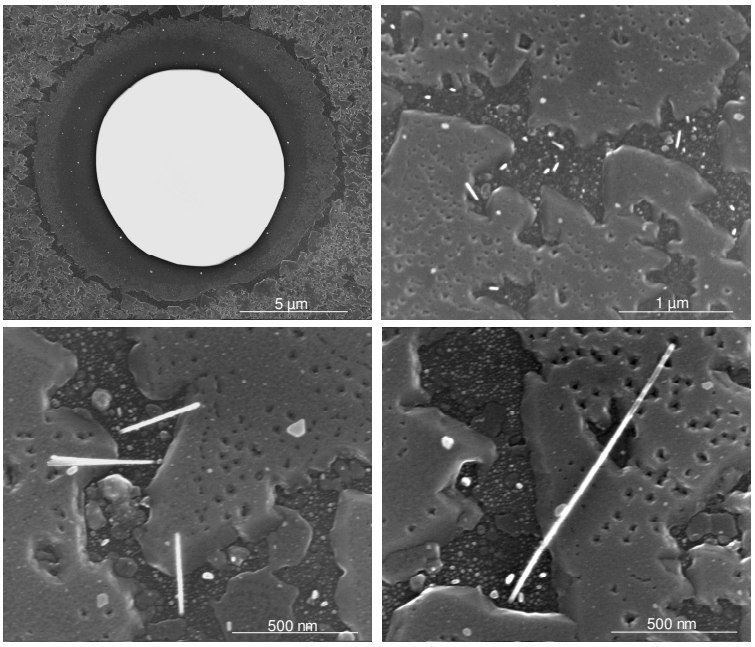

Figure 5.26: Nanowhiskers on silicon with indium applied as solvent. After desorption, indium was evaporated for 5 min at T=590 °C and R=0.5 Å/s, afterwards silicon for 60 min at T=590 °C and R=0.5 Å/s.

The growth of nanowhiskers from indium was insensitive to a change of substrate temperature, rate and evaporation time of metal and silicon evaporation. Furthermore, a droplet on top of the whiskers could not be found.

The difficulties with growing nanowhiskers using indium as the solvent will be discussed in the following.
Growth of nanowhiskers could not be performed at all without the oxide

desorption step. The whiskers which appeared sporadically were very thin. By EDX measurement, shown in fig. 5.27, it could be confirmed that they were made of silicon.

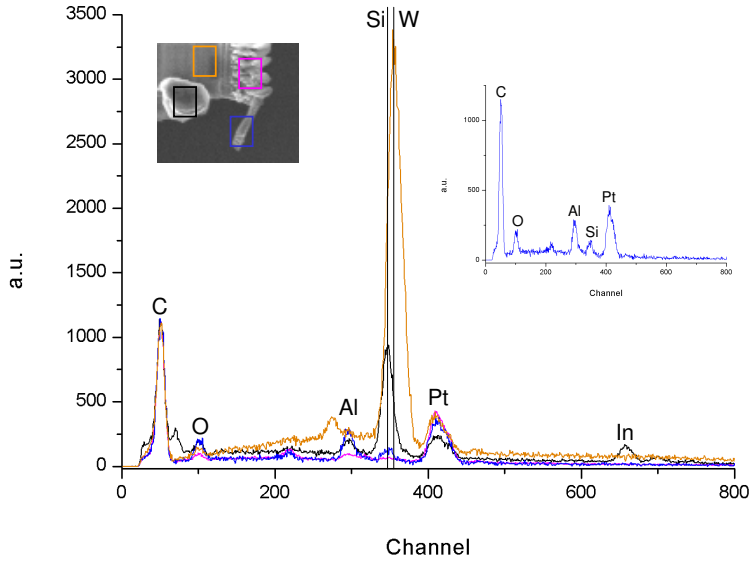

Figure 5.27: EDX measurement of a whisker grown from indium.

The left inset in fig. 5.27 shows the secondary electron image of the whisker investigated. It had a diameter of about 50 nm and was torn out of the sample by a micromanipulator to measure EDX without any disturbance from the surroundings. The micromanipulator is a tungsten needle, whereon the orange rectangle is drawn in the image. The whisker is glued to the needle by platinum (magenta rectangle). Indium, accidently picked up from the sample, was detected from the measurements in the area of the black rectangle. The colors correspond to the curves in the diagram. The right inset shows only the measured curve of the whisker. Carbon and oxygen are always on the sample, and the aluminum and platinum peak are results of the presence of parts of the micromanipulator. Thus, the whisker is made of silicon.

There are no literature reports about silicon nanowhiskers grown from indium droplets by PVD. There are only few published reports about the growth of silicon whiskers from indium droplets by CVD. Givargizov and Sheftal [71] show in a 1971 publication whiskers grown from gallium by CVD. They

report that the results of whiskers grown from indium are similar but do not show any images. Bootsma and Gassen [15] also tried to grow silicon and germanium whiskers from indium deposits by CVD and failed. They argue that the slope of the liquidus in systems with indium, tin or bismuth could be too high or that the catalytic activity of these metals could be too low.
However, Iacopi et al. [72] succeeded in growing nanowhiskers using indium as a solvent. They used plasma-enhanced CVD, i.e. silicon was already supplied in dissociated species to the substrate. In their case, indium was electrodeposited from an aqueous solution after cleaning the substrate by HF. Before further processing, samples were treated by H_2 plasma to remove surface oxides. The growth rate of the whiskers amounted to 1 micron per min. The difference between their equipment and ours is that it was possible for them to provide a large silicon rate and probably to clean the surfaces better.

An interesting theoretical approach can be found in a publication of Nebol'sin and Shchetinin [73]. They consider the role of surface energies in the vapor-liquid-solid growth of silicon and thus also the role of different solvents. With their model, they predict very good growth amongst others from gold droplets and very poor growth from indium. The model will be presented and discussed here.
They consider the general case of a tapered whisker, as can be seen in fig. 5.28.

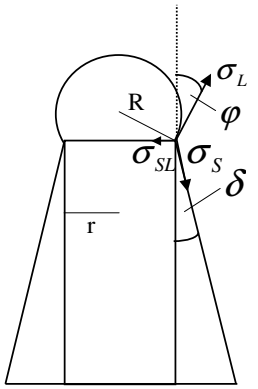

Figure 5.28: Conical whisker; R: droplet radius, r: radius of the whisker at its top, φ: wetting angle, δ: tapering angle, σ_{SL}: interface energy solid-liquid, σ_L: interface energy liquid-vapor, σ_S: interface energy solid-vapor.

They cite Voronkov [74] who calculated the change of energy during displacement of the 3-phase line for bulk growth from the melt. Applied to whisker growth, this looks as shown in fig. 5.29.

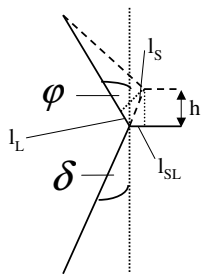

Figure 5.29: Displacement of the 3-phase line during conical whisker growth of a monolayer h.

For the angles, the following is valid:

$$\cos\delta = \frac{h}{l_S} \qquad \sin\delta = \frac{l_{SL}}{l_S} \qquad \cos(\varphi+\delta) = \frac{l_L}{l_S} \tag{5.4}$$

The total change of surface energy γ per h adds up to:

$$\gamma = \frac{1}{h}\left(\sigma_S \cdot l_S - \sigma_{SL} \cdot l_{SL} - \sigma_L \cdot l_l\right)$$

$$= \frac{1}{h}\left(\sigma_S \cdot \frac{h}{\cos\delta} - \sigma_{SL} \cdot \frac{h}{\cos\delta}\sin\delta - \sigma_L \cdot \frac{h}{\cos\delta}\cos\left(\varphi+\delta\right)\right) \tag{5.5}$$

Equating the derivative of γ with respect to δ to zero yields:

$$\gamma\left(\varphi\right) = \sqrt{\sigma_S^2 - \left(\sigma_{SL} - \sigma_L \sin\varphi\right)^2} - \sigma_L \cos\varphi \tag{5.6}$$

The following condition being valid for the equilibrium of surface energies, cf. equation 1.13, has been applied to receive eq. 5.6:

$$\sin\varphi = \frac{\sigma_{SL} - \sigma_S \sin\delta}{\sigma_L} \tag{5.7}$$

γ in equation 5.6 is the minimum increase of the surface Gibbs energy. The authors argue that it includes the reduction in the liquid-vapor interfacial

energy upon a displacement of the droplet by distance h and the solid-vapor interfacial energy increment and that $\gamma(\varphi)$ should be equated less than σ_{SL} so that the total energy change is negative. This is not understandable because equation 5.6 includes contrary to their statement the reduction in the solid-liquid interfacial energy as well. This can be seen in the deduction of Voronkov . However, the idea of assessing the feasibility of whisker growth according to the surface tension of the solvent is in principle a good one. The energy change during a displacement of the 3-phase line expressed in equation 5.6 is different for different solvent materials. Thus, for some solvents less energy is necessary to promote growth than for others. But the driving force for growth as described in section 1.2.1 is always supersaturation. Assuming $\delta = 0$ and $\varphi = 90°$, $\gamma(\varphi)$ is larger for indium than for gold, because σ_L is smaller than for gold, cf. section 5.1. However, supersaturation should be more easily achieved than in the case of gold because indium is already supersaturated at less than 1 % silicon content. Thus, surface tension cannot be the only reason that growth is either enhanced or impeded. The question is also how effectively silicon can get into a solvent droplet. Here, probably the rate and the absence of oxide on the droplet surface play an important role and may be the reason for the success of Iacopi et al. [72] in whisker growth from indium.

5.3 Germanium nanowhisker growth

To analyze the principles of whisker growth further, another material system was investigated for comparison. Germanium was chosen because of its affinity to silicon and its promising possibilities for application. Gold was again taken as the solvent.

Growth on Ge(111)

As for silicon, the first experiment, shown in fig. 5.30, was carried out to compare droplet distribution and whisker distribution. After desorption, gold was evaporated on both samples at a rate of 0.4 Å/s for 10 s and at a temperature of 430 °C. The best growth temperature for PVD is related to the melting point of the material [75], thus a lower temperature was chosen for germanium nanowhisker growth than for silicon. On one of the samples, germanium has been evaporated for 150 min at a rate of 0.5 Å/s afterwards.

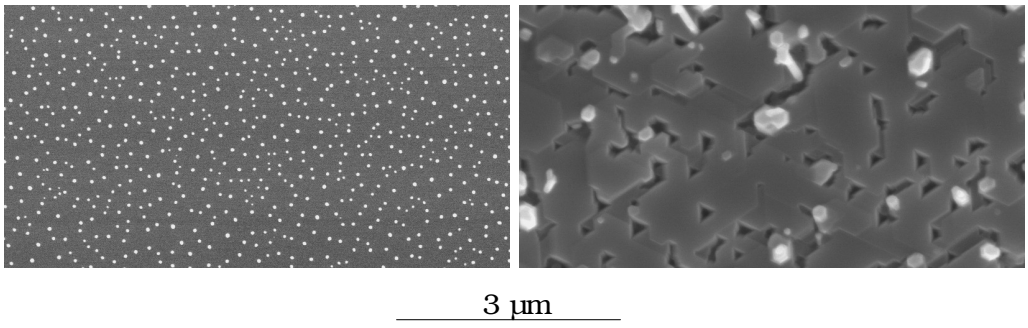

Figure 5.30: Left: gold droplets on germanium, right: germanium nanowhiskers on germanium.

As in the case of silicon, it is clearly visible that droplet distribution differs from the obtained whisker distribution.

In the following, the influence of the experimental parameters on the growth of germanium nanowhiskers will be shown.

Germanium rate:

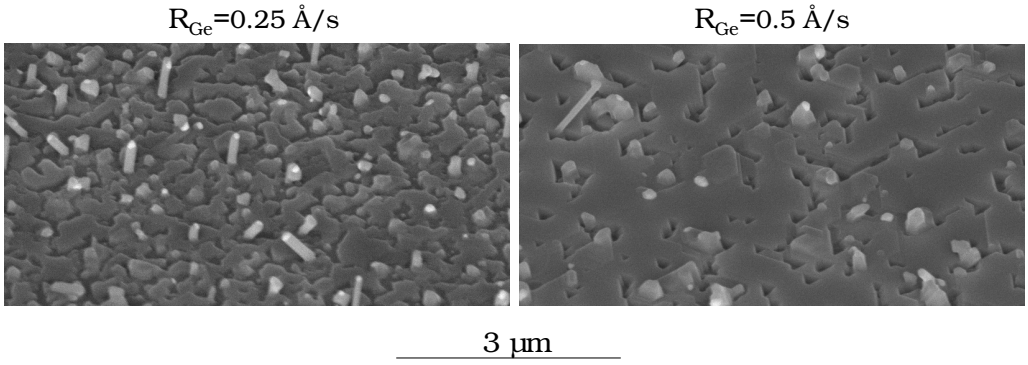

Preceding desorption, T=430 °C, R_{Au}=0.4 Å/s, t_{Au}=10 s, t_{Ge}=150 min

Figure 5.31: Germanium nanowhiskers on germanium. Influence of evaporation rate.

A higher rate seems to lead to a lower density of whiskers but those results are not as easily to interpret as the ones on silicon.

Evaporation time:

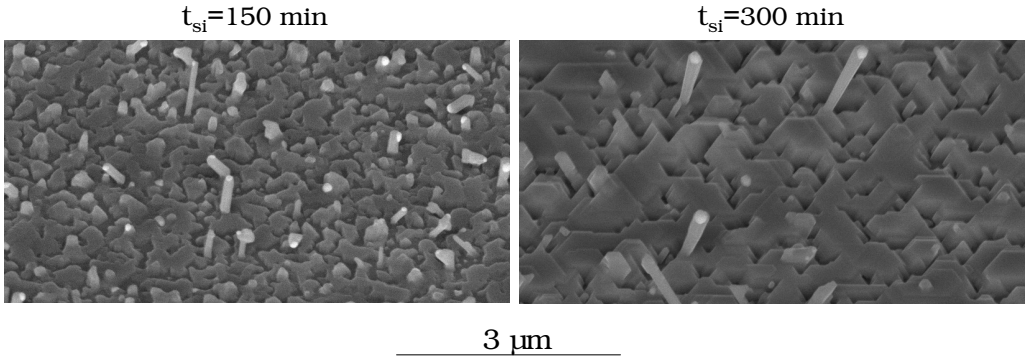

Preceding desorption, T=430 °C, R_{Au}=0.4 Å/s, t_{Au}=10 s, R_{Ge}=0.25 Å/s

Figure 5.32: Germanium nanowhiskers on germanium. Influence of evaporation time.

As on silicon, a longer evaporation time leads to longer nanowhiskers.

Substrate temperature:

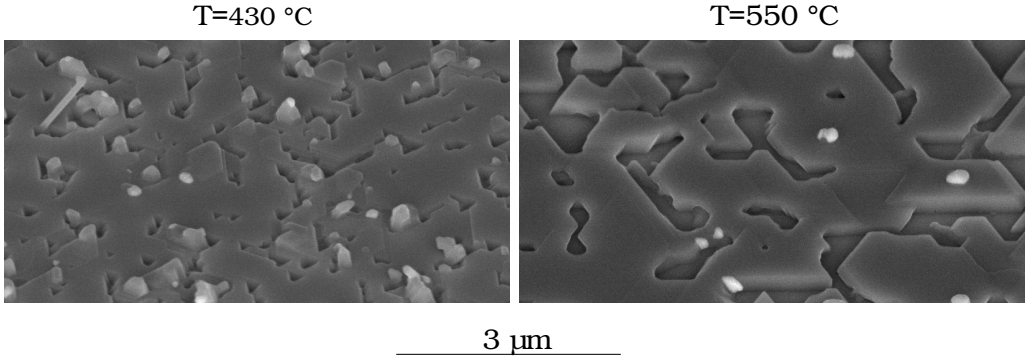

Preceding desorption, R_{Au}=0.4 Å/s, t_{Au}=10 s, R_{Ge}=0.5 Å/s, t_{Ge}=150 min

Figure 5.33: Germanium nanowhiskers on germanium. Influence of substrate temperature.

Above a certain temperature, whiskers do not grow any more. Instead, a layer forms on the whole substrate.

Oxide desorption step:

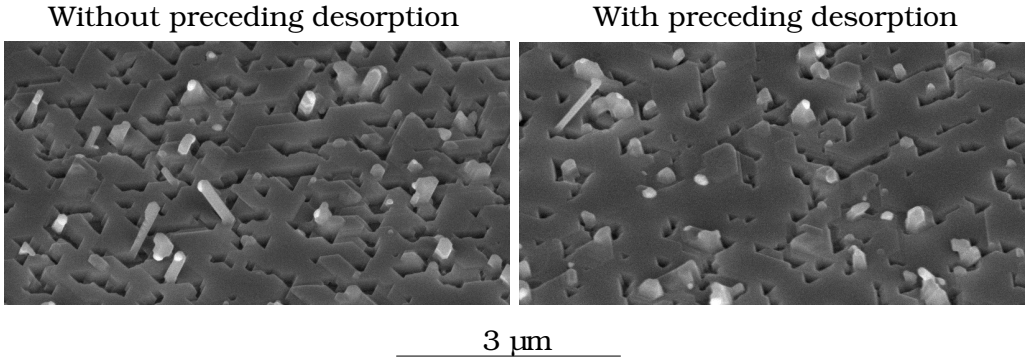

T=550 °C, R_{Au}=0.4 Å/s, t_{Au}=10 s, R_{Ge}=0.5 Å/s, t_{Ge}=150 min

Figure 5.34: Germanium nanowhiskers on germanium. Left: without preceding desorption step, right: with preceding desorption step.

The oxide desorption step does not influence the outcome of the experiment significantly.

Germanium behaves very differently from silicon. The most striking fact is the whiskers' direction of growth which is not always [111] as on silicon. In order to find out the direction, the sample was tilted in the SEM until the whisker of interest was seen from above. As shown in fig. 5.35, this was the case at a tilt angle of 35°, e.g. the angle between whisker and substrate was 55°.

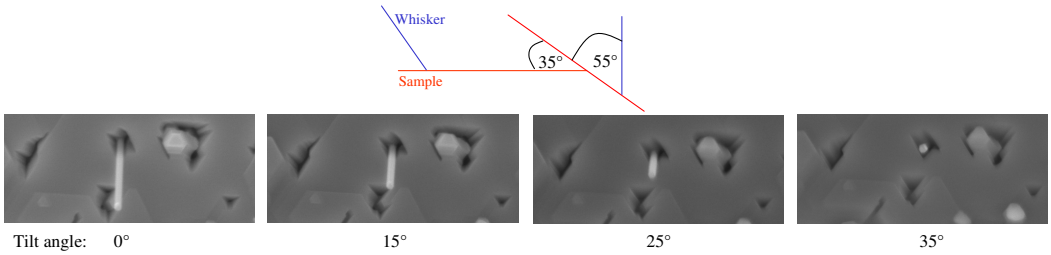

Figure 5.35: Determination of the angle between germanium substrate and whisker.

By TEM measurements, this growth direction was verified as can be seen in fig. 5.36. It was also seen that whisker growth began in [111] direction before kinking.

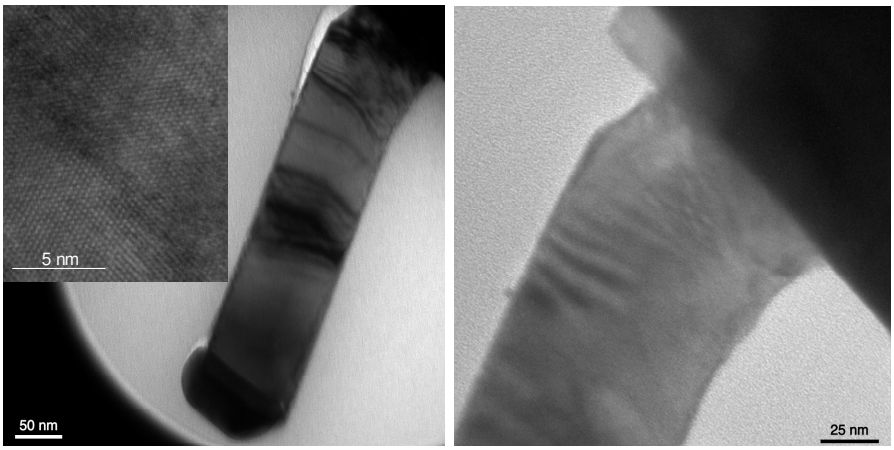

Figure 5.36: TEM image of a Ge whisker on Ge(111).

Growth on germanium substrates with other orientations

To get more information about directions of growth of germanium whiskers on germanium, several experiments on differently oriented substrates were performed.
In fig. 5.37, the typical outcome of an experiment on a Ge(100) substrate can be seen. This did not change to any large extent if substrate temperature or evaporation rate were changed. The structures were mostly pyramids, some individual whiskers at an angle of 45° to the substrate could also be seen.

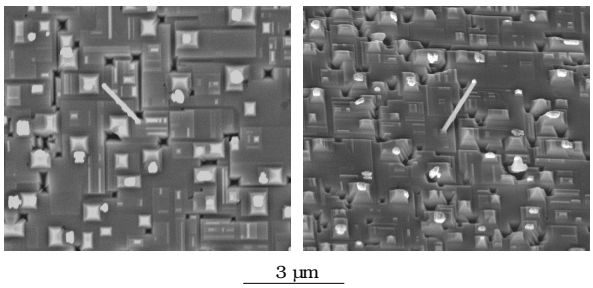

Preceding desorption, T=430 °C, R_{Au}=0.4 Å/s, t_{Au}=30 s, R_{Ge}=0.5 Å/s, t_{Ge}=150 min

Figure 5.37: Non-tilted and tilted view of a growth experiment on Ge(100).

Fig. 5.38 shows a typical result of an experiment performed on a Ge(110) substrate.

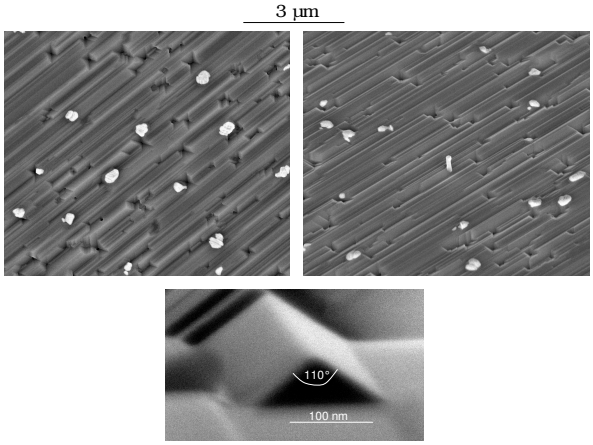

Preceding desorption, T=430 °C, R_{Au}=0.4 Å/s, t_{Au}=30 s, R_{Ge}=0.5 Å/s, t_{Ge}=150 min

Figure 5.38: Non-tilted and tilted view of a growth experiment on Ge(110).

In this case as well, the roof-like structure appeared independently of the experimental parameters, even on a substrate which was only annealed with gold, as shown in fig. 5.39.

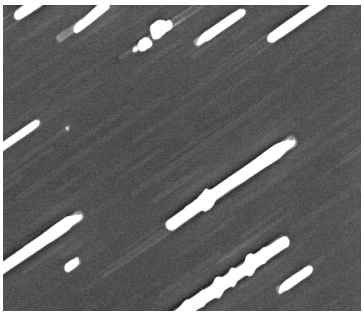

Figure 5.39: Ge(110) annealed with gold.

Discussion of the growth results on germanium

As on silicon, the first experiment was performed to compare droplet distribution and whisker distribution and again it turned out that the whisker density was smaller than the original droplet density.
The interpretation of the results on germanium is not straightforward compared to silicon. The orientation of the whiskers is most striking and it seems to change to [111] in the case of higher rates and higher temperatures. The desorption step does not improve the results. A longer evaporation time seems to result in longer whiskers as in the case of silicon.
In order to understand the results, the crystallographic structure of silicon and germanium as well as nucleation energies on different surfaces will be considered. Both materials crystallize in diamond structure which is shown in fig. 5.40. The diamond lattice consists of two face centered cubic (FCC) lattices, placed next to one another along the body diagonal of the cubic cell and separated by one quarter of its length.

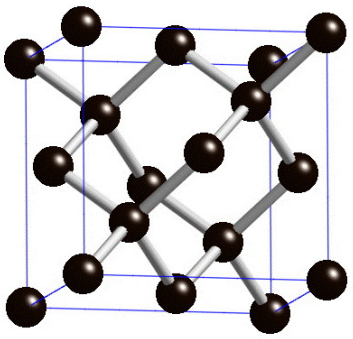

Figure 5.40: The diamond crystal lattice, taken from [76].

Fig. 5.41 shows the angles between different facets of the silicon and germanium crystal.

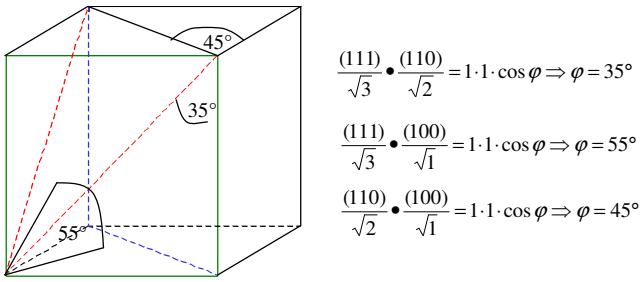

Figure 5.41: Angles between different facets of the diamond lattice.

Thus, the whiskers on germanium which could be seen from above in the SEM after having tilted the (111) substrate by 35° grew in <110> direction. Also the few whiskers on the (100) substrates, at an angle of 45° to the substrate, grew in <110> direction.
Fig. 5.42 shows the main difference between silicon and germanium nanowhisker growth.

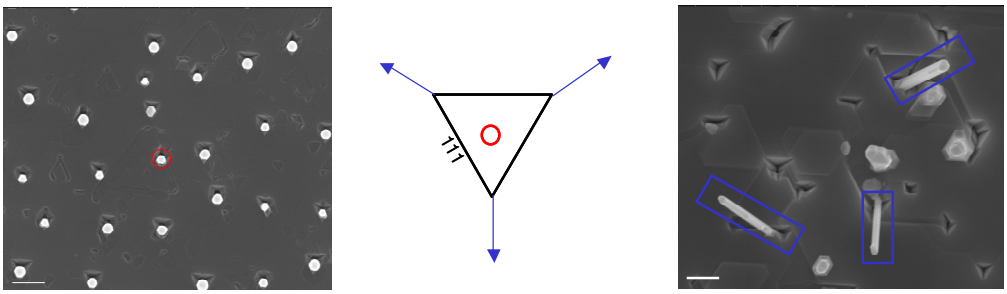

Figure 5.42: Left: Si whiskers on Si(111). Right: Ge whiskers on Ge(111). Middle: Projection of the [111] and <110> directions on a (111) surface.

To answer the question why germanium behaves in such a manner, nucleation energies on different crystal facets are considered.

Grzegory et al. [77] calculated the change in Gibbs free energy related to the formation of 2D nuclei on different surfaces of GaN and we followed their idea for our materials. We also assume a flat interface between droplet and whisker and thus growth by 2D nucleation, cf. the sketch on the right side. This assumption is reasonable because it has been shown by TEM for heterostructures in semiconductor nanowhiskers that the junctions are atomically sharp [78].

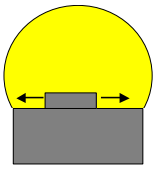

The critical nucleation energy, i.e. the energy which is necessary to form a critical nucleus as described in section 1.2.2, depends on the orientation of the surface. The surface orientation determines the form of the nucleus as well as the number of the resulting additional unsaturated bonds created. On the basis of the lattice geometry, the nuclei on the three main surfaces are expected as shown in fig. 5.43.

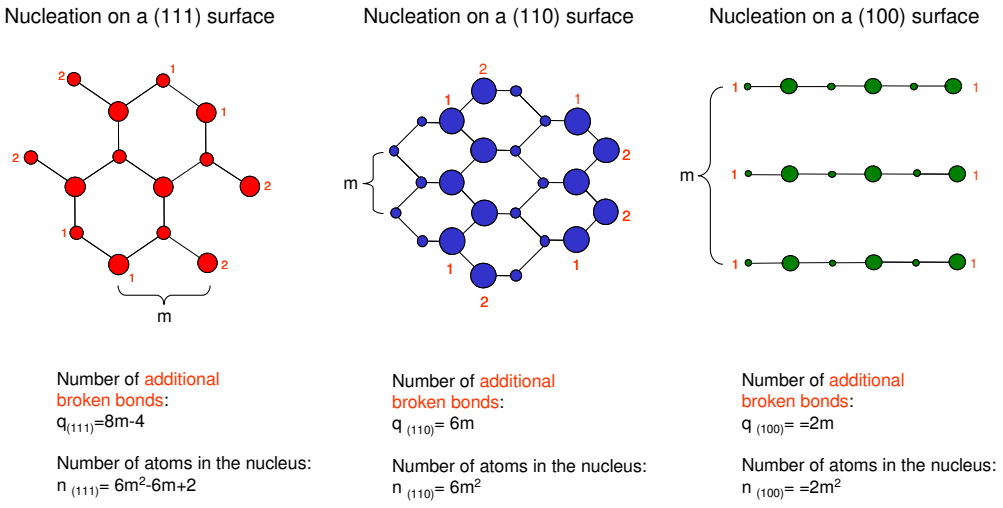

Figure 5.43: Expected shape of nuclei on the (111), (110) and (100) surface of a crystal with diamond lattice.

Atoms beneath are shown smaller. The size of the nuclei is parameterized by m, which is the number of atoms along one side of the nucleus. The total number of atoms n as well as the number of additional unsaturated bonds q are functions of m. The small red numbers correspond to the additional unsaturated bonds for the number of atoms shown in fig. 5.43. The validity of the functions in fig. 5.43 can be easily shown by mathematical induction.

This is exemplified by the nucleus on a (111) surface:
If m=1, the nucleus appears as shown on the right. The atom below has saturated one bound of the surface and has two remaining unsaturated bonds. The second one has three remaining unsaturated bonds. There is a total of four *additional* unsaturated bonds.

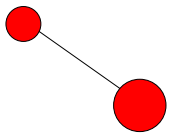

Inserting $m = 1$ into the formula for the additional unsaturated bonds on a (111) surface yields four, i.e. the formula is true for $m = 1$. To show that the statement holds for $m + 1$ as well, provided that it holds for m, the additional unsaturated bonds for $m = 1, 2, 3, 4$ are shown in fig. 5.44, which can be found out by considering the diamond lattice in detail.

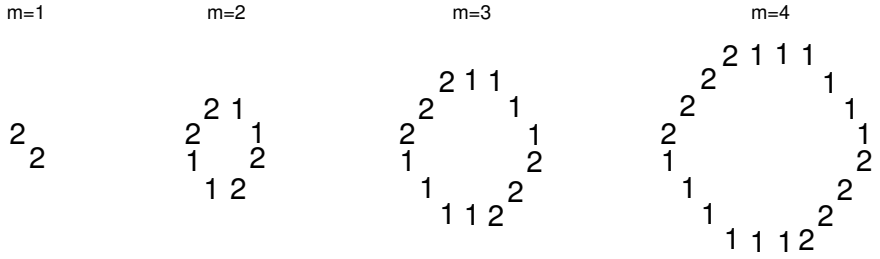

Figure 5.44: Additional unsaturated bonds for m=1-4.

Thus, increasing m by 1 means increasing the number of additional unsaturated bonds by $2 \cdot 2 + 4 \cdot 1$. The inductive step can be seen in the following:

$$q_m + 2 \cdot 2 + 4 \cdot 1 = 8m - 4 + 4 + 4 = 8m + 4 = 8(m+1) - 4 = q_{m+1}$$

In analogy, the formula for the number of atoms in the nucleus can be proven. For $m = 1$, $n(1) = 6 - 6 + 2 = 2$. The development of the number of atoms (only one layer) with increasing m is shown in fig. 5.45.

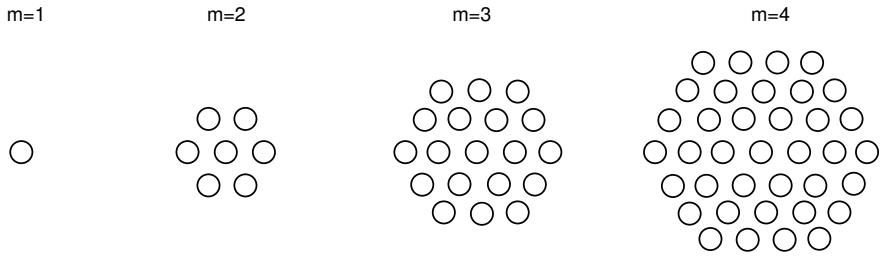

Figure 5.45: Number of atoms of one layer for m=1-4.

Increasing m by 1 means increasing the number of atoms by

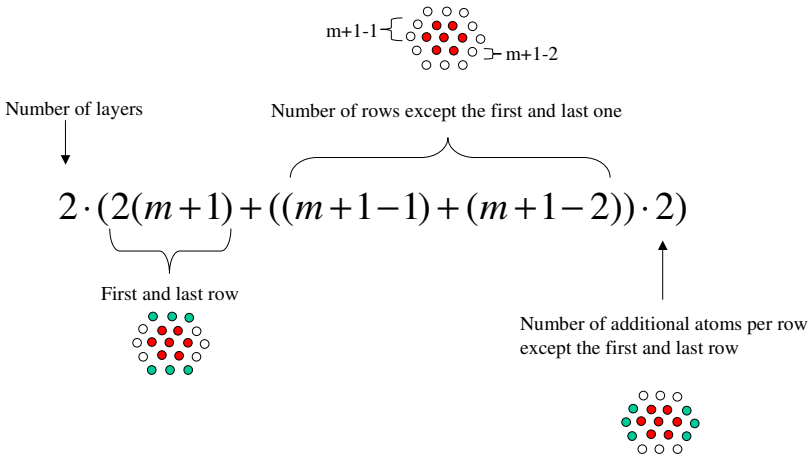

The mth nucleus is shown in red.

The inductive step can be seen in the following:

$$n_m + 2(2(m+1) + ((m+1-1) + (m+1-2)) \cdot 2)$$

$$= 6m^2 - 6m + 2 + 4m + 4 + 4m + 4m - 4$$

$$= 6m^2 + 6m + 2$$

$$= 6(m+1)^2 - 6(m+1) + 2 = n_{m+1}$$

In analogy, the formulas for additional unsaturated bonds and number of atoms on the (110) and the (100) surface can be verified by mathematical induction as well.

To determine the nucleation energy ΔG, volume and surface contributions have to be considered, cf. fig. 1.3. The volume term is negative and proportional to the number of atoms in the nucleus: $-n(m)\Delta\mu$. $\Delta\mu$ is the difference in chemical potential of the atoms before and after incorporation into the nucleus and can be expressed as a function of temperature and supersaturation, cf. equation 1.9. The surface term is positive and proportional to the number of additional unsaturated bonds resulting from building new surfaces: $q(m)\Phi$. Φ is the energy of an unsaturated bond. Thus, ΔG can be expressed as:

$$\Delta G(m) = -n(m)\Delta\mu + q(m)\Phi \tag{5.8}$$

To determine m^*, the number of atoms along one side of the critical nucleus, the derivative of $\Delta G(m)$ with respect to m has to be equated to zero. Inserting m^* into eq. 5.8 results in $\Delta G(m^*)$, the energy necessary to form a critical nucleus. Like $\Delta\mu$, also $\Delta G(m^*) \equiv \Delta G^*$ is a function of temperature and supersaturation. For the three different surfaces, the following is obtained:

$$\Delta G^*(111) = -\frac{1}{2}kT \cdot ln\frac{x}{x_0} + \frac{8}{3}\frac{\Phi^2}{kT \cdot ln\frac{x}{x_0}} \tag{5.9}$$

$$\Delta G^*(110) = \frac{3}{2}\frac{\Phi^2}{kT \cdot ln\frac{x}{x_0}} \tag{5.10}$$

$$\Delta G^*(100) = \frac{1}{2}\frac{\Phi^2}{kT \cdot ln\frac{x}{x_0}} \tag{5.11}$$

$\frac{x}{x_0}$ is the supersaturation.
This is qualitatively shown for different temperatures in fig. 5.46.

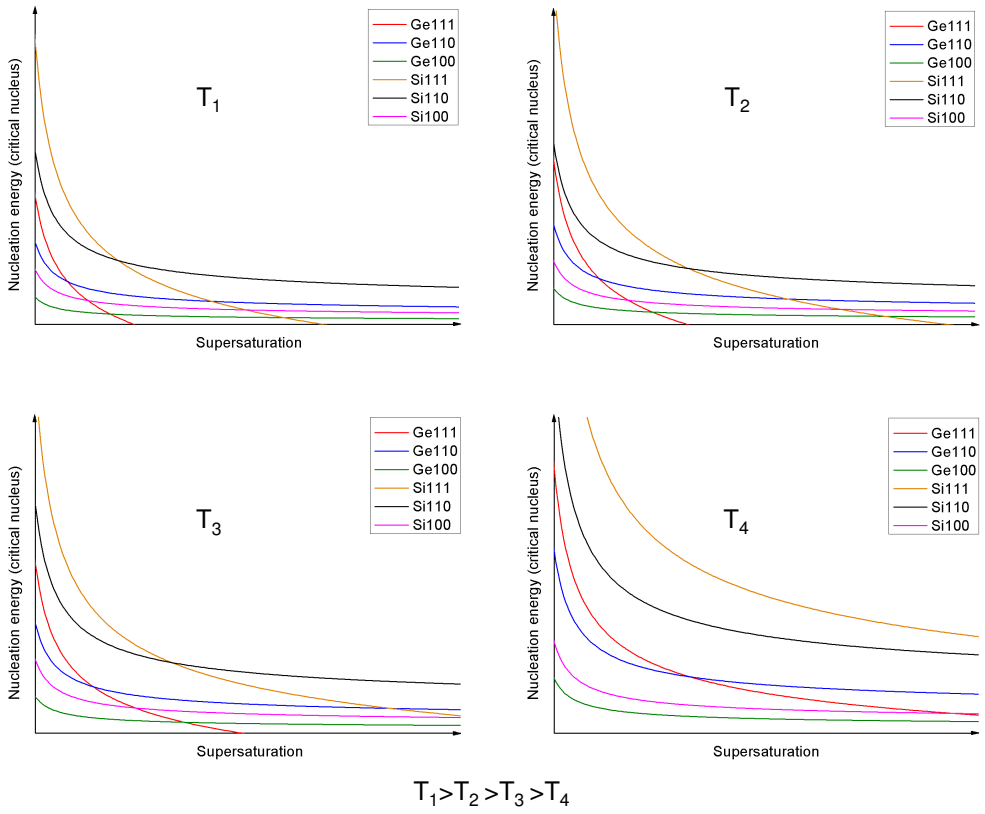

Figure 5.46: Nucleation energy versus supersaturation for different temperatures on different surfaces of silicon and germanium.

Φ is not known for the growth from solution. But from this qualitative plot, it can be seen that at lower supersaturation, nucleation on (110) is favored whereas at higher supersaturation, nucleation on (111) is favored. For a given orientation, the intersection is for higher temperatures at lower supersaturation. This is valid for both silicon and germanium. As the energy of a Si–Si bond (3.73 eV) is larger than the one of a Ge–Ge bond (3.56 eV) [79], also Φ is supposed to be larger for silicon than for germanium. If these assumptions are correct, it is possible that the first nucleus, which is in the case of a (111) substrate always (111) orientated, exhibits facets with other orientations. If then nucleation is favored on another facet than (111), growth can also proceed in other directions. From the diagrams in fig. 5.46, one can conclude that growth is favored on (111) surfaces at high temperature and

high supersaturation. The supersaturation is assumed to be a function of the germanium rate. Fig. 5.47 shows results at different rates and temperatures and confirms the applicability of our assumptions.

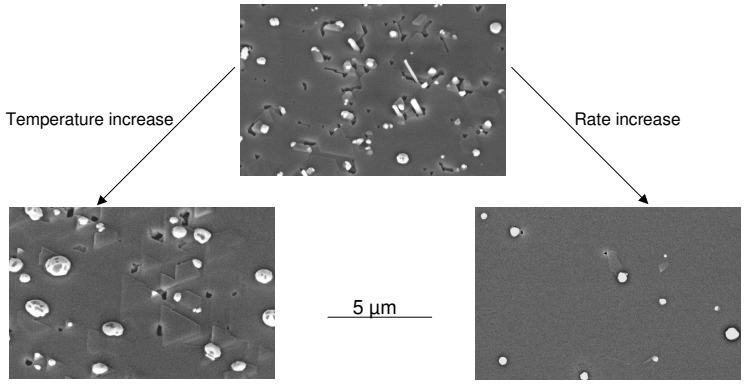

Figure 5.47: Germanium whiskers on germanium grown at different rates and temperatures.

However, it is striking that there are no real whiskers in the [111] direction because their height is minimal. The reason for this fact could be the slower growth of the (111) facets because they are always the remaining facets with the lowest surface energy [80]. That they are the most slowly growing facets can also be seen from the experiments performed on (110) and (100) substrates where in the first case roofs and in the second pyramids are forming – both with (111) facets.
Why no whiskers grew in a <100> direction is still an open question. In our model, the critical nucleation energy is lowest on (100) surfaces as can be seen in fig. 5.46. One reason could be that the (100) facet has the highest surface energy [81] and thus does perhaps not form during nucleation.
From the results on germanium we concluded that also on silicon it should be possible to get growth directions of whiskers different from [111]. We tried a low silicon rate of less than 0.1 Å/s and got indeed some first results showing whisker growth in <110> direction as can be seen in fig. 5.48.

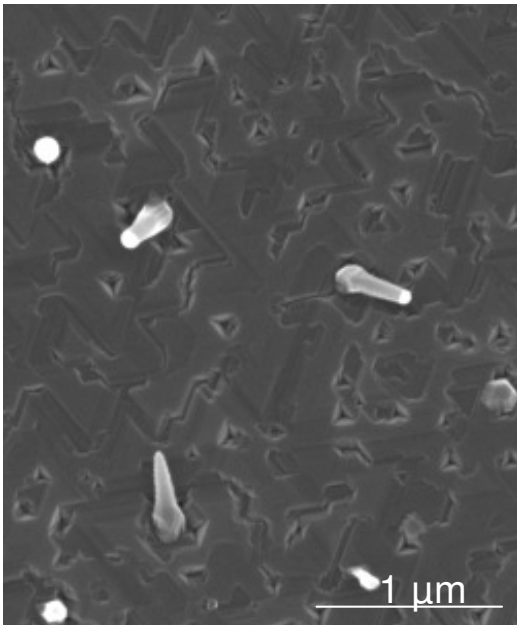

Figure 5.48: Silicon whiskers on Si(111) grown at a very low silicon rate.

Further investigations, and especially an exactly known silicon rate, are necessary to understand the influence of rate and temperature on the growth direction on silicon.

5.4 Silicon-germanium heterostructures

After having grown silicon nanowhiskers on silicon substrates and germanium nanowhiskers on germanium substrates, heterostructures of the two materials were grown as well. Fig. 5.49 shows germanium nanowhiskers grown on a silicon substrate.

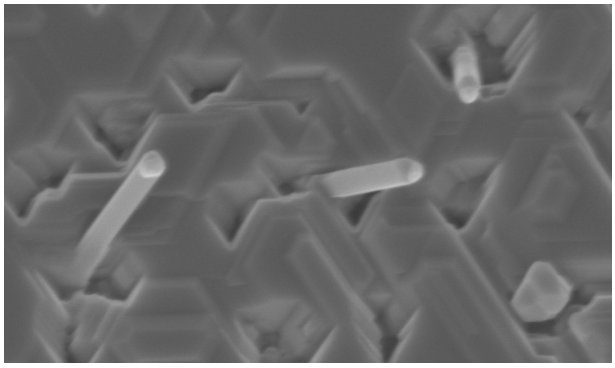

Preceding desorption, T=480 °C, R_{Au}=0.4 Å/s, t_{Au}=10 s, R_{Ge}=0.5 Å/s, t_{Ge}=150 min

Figure 5.49: Germanium nanowhiskers on a silicon substrate.

In analogy to the experiments on silicon, silicon nanowhiskers on germanium were grown as well, as shown in fig. 5.50.

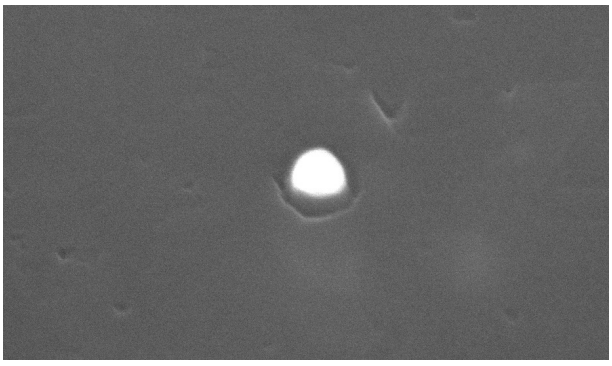

Preceding desorption, T=435 °C, R_{Au}=0.4 Å/s, t_{Au}=10 s, R_{Si}=0.5 Å/s, t_{Si}=150 min

Figure 5.50: Silicon nanowhisker on a germanium substrate.

On silicon substrates, also SiGe heteronanowhiskers were grown, see fig. 5.51. They show kinks at the junction of silicon and germanium, because silicon grows perpendicular to the substrate and germanium subsequently at an angle of 55°. The composition of the whiskers was analyzed by EDX.

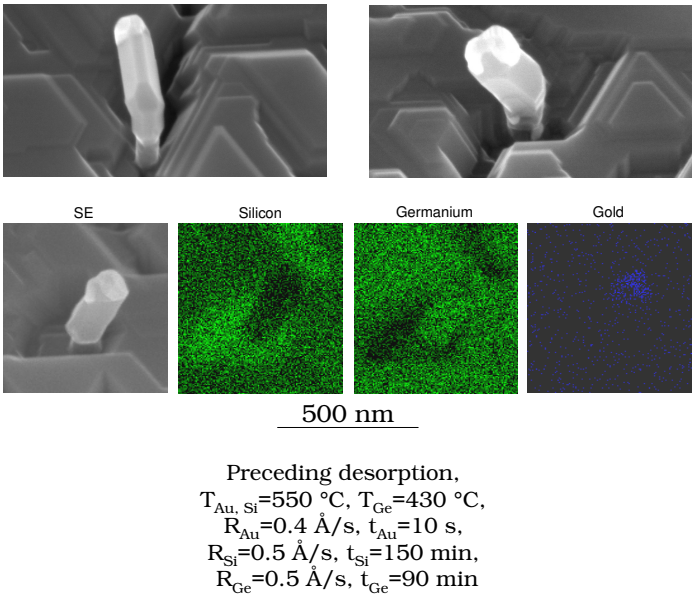

Figure 5.51: SiGe nanowhiskers on a silicon substrate and results of EDX measurements.

In spite of the 4 % larger lattice constant of germanium in comparison to silicon, it was possible to grow germanium nanowhiskers on silicon in <110> direction and silicon nanowhiskers on germanium in the [111] direction of the substrate. For these cases, eq. 5.8 has to be changed because there is an additional term caused by the number of "substituted" unsaturated bonds, i.e. bonds which are broken at the substrate surface and then saturated by a foreign atom. Then the following is valid

$$\Delta G(m) = -n(m)\Delta\mu + q(m)\Phi_N + x(m)(\Phi_N - \Phi_S) \tag{5.12}$$

The subscripts N and S refer to the nucleus and the substrate atoms. $x(m)$ is the number of "substituted" broken bonds, which is in the case of a (111) and a (110) surface equal to 0.5 x $n(m)$, and in the case of a (100) surface equal to $n(m)$. In the case of homoepitaxy, i.e. the substrate and nucleus atoms are the same, eq. 5.12 is identical to eq. 5.8.

Fig. 5.52 shows the critical nucleation energy against supersaturation for silicon on germanium and for germanium on silicon omitting growth on <100> surfaces. The curves look qualitatively like in the homoepitaxial case.

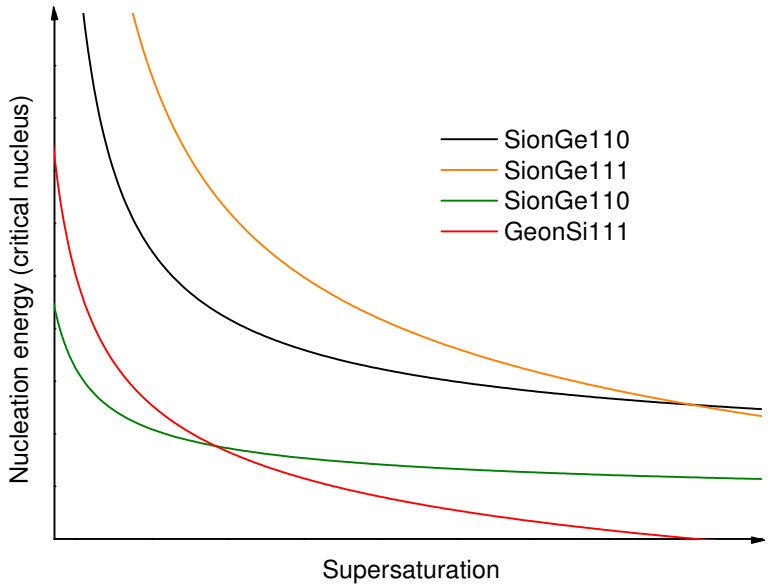

Figure 5.52: Nucleation energy against supersaturation for silicon growth on germanium and for germanium growth on silicon.

It was assumed that $\Phi_{Si} > \Phi_{Ge}$ and that growth experiments of silicon on germanium are performed at higher temperatures than in the opposite case. That means that we have a higher supersaturation in the case of silicon on germanium which could explain the growth in [111] direction. However, this vertical growth proceeds very slowly like in the homoepitaxial case of germanium on germanium.
Silicon-germanium heterostructures on silicon have also been grown, and a kink can be seen at the interface of the two materials. At first, silicon whisker growth proceeds normally in [111] direction. Germanium then changes the direction of the whisker to a <110> direction which can be explained based on our model.

5.5 Arrangement of nanowhiskers

Silicon – also with different layers on top – and germanium substrates have been structured as described in chapter 3 to provide preferential points for droplet formation and for whisker growth.

Silicon nanowhiskers

Fig. 5.53 shows silicon nanowhiskers grown from an ordered array of gold droplets.

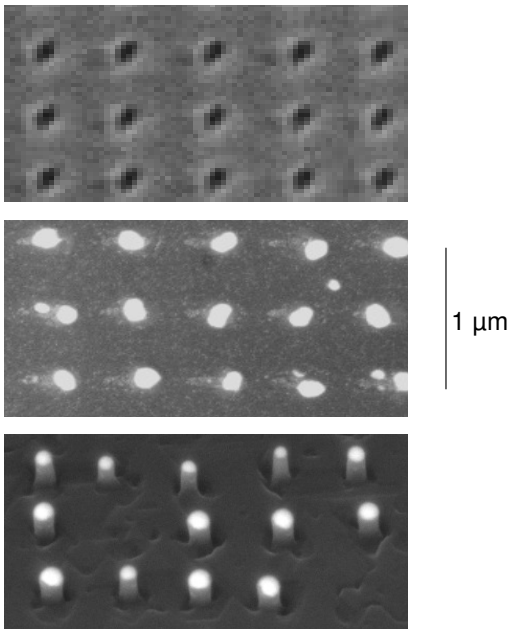

Figure 5.53: FIB holes, an ordered array of gold droplets and ordered nanowhiskers.

The first three images in fig. 5.54 show whiskers grown on pre-structured areas, the forth image shows whiskers grown outside of the structure for comparison.

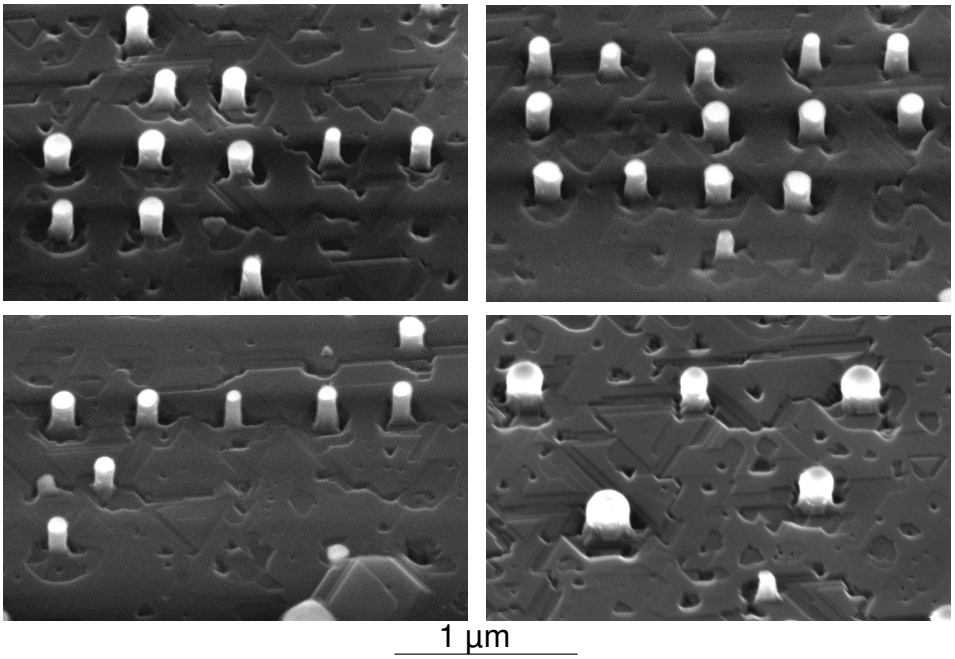

Figure 5.54: Silicon nanowhiskers grown from an ordered array of gold droplets and in the forth image on a non-structured area.

After adjustment of gold rate and substrate temperature during evaporation, perfect arrays of ordered gold droplets on silicon (see chapter 3) were obtained. Silicon nanowhiskers from an array of gold droplets could be successfully grown. However, it was not possible to grow a whisker from every droplet. Growth seems to be strongly dependent on the surface state. But in principle it is possible to heal the lattice damaged by FIB during growth and to array silicon nanowhiskers.

Germanium nanowhiskers

Germanium whiskers were grown on pre-structured substrates as well. The result can be seen in fig. 5.55.

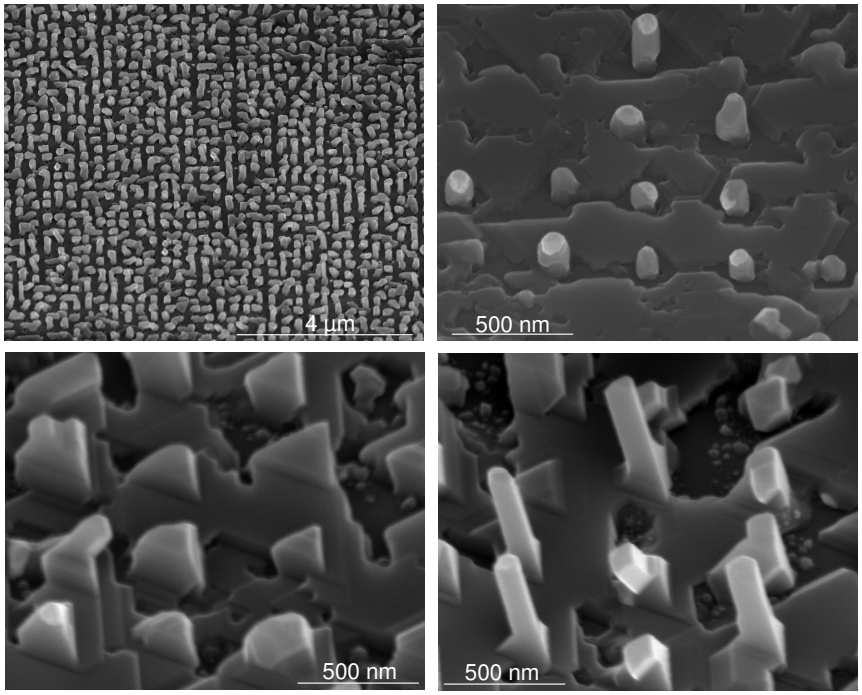

Figure 5.55: Germanium nanowhiskers grown from an ordered array of gold droplets.

As on silicon, perfect arrays of ordered gold droplets were obtained on germanium. However, in the case of germanium, it was seen to be much more difficult to order the whiskers. Our explanation for this fact is again the tendency for germanium whiskers to grow in a different direction in comparison to silicon whiskers.

GaN nanowhiskers

As described in chapter 3, silicon substrates with or without different layers on top have been structured to array GaN nanowhiskers. The growth results shown in the following were achieved at Forschungszentrum Jülich.
GaN nanowhiskers can be obtained using catalyst-free MBE growth at high temperature (about 800 °C) and N-rich conditions. The growth implies a nucleation stage at which stable nanocrystals are constructed from Ga and N adatoms. Some of these nanocrystals with a favorable orientation develop rapidly into nanowhiskers by a diffusion induced mechanism [82, 83, 84]. The nucleation and the subsequent growth processes are controlled not only by surface diffusion of the species, but also by adsorption and desorption of adatoms, especially of Ga which limits the growth rate at N-rich conditions. At a constant N flux and a controlled Ga flux and deposition temperature, nucleation and multiplication of nanowhiskers depends on the substrate type and its roughness. Thus, selective MBE epitaxy of GaN nanowhiskers can be obtained using FIB patterned substrates, where areas of very small nucleation and growth rate coexist with areas of fast nanowhisker formation.
Fig. 5.56 shows GaN nanowhiskers grown on Si(111). The bare Si(111) substrate was pre-structured by focused ion beams with holes in a hexagonal pattern. In comparison to the rest of the substrate, longer nanowhiskers with a higher areal density form in the pattern.

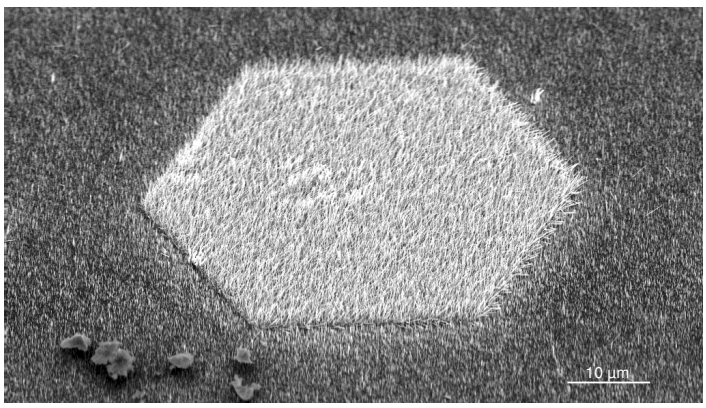

Figure 5.56: GaN nanowhiskers on structured Si(111).

The result of GaN nanowhisker growth on an area patterned with holes in a 5 nm AlN layer on Si(111) can be seen in fig. 5.57.

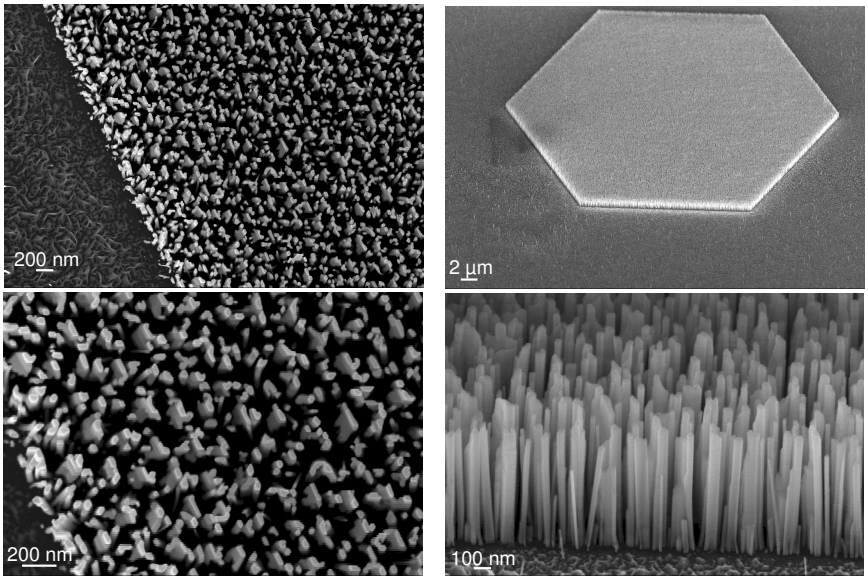

Figure 5.57: GaN nanowhiskers on structured Si(111) covered with a 5 nm AlN layer. Left: top view, right: side view.

On the same sample, also a mesh of stripes has been structured (fig. 3.13) resulting in AlN dots in a uniform array. This area looks like shown in fig. 5.58 after the growth process.

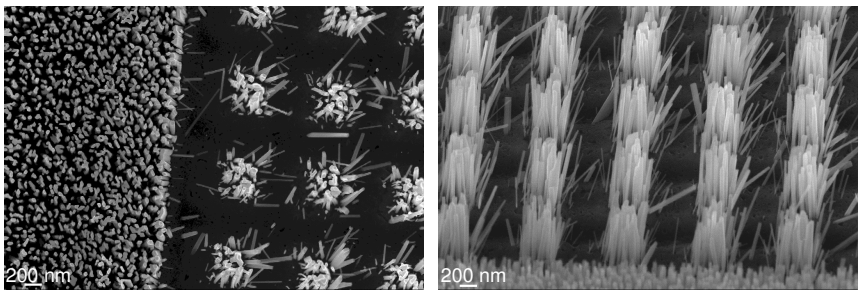

Figure 5.58: GaN nanowhiskers on Si(111) with a 5 nm AlN layer structured with a mesh of stripes. Left: top view, right: side view.

Using a structured Si substrate with a 20 nm AlN layer and a 5 nm Si layer (fig. 3.14) results in growth shown in fig. 5.59.

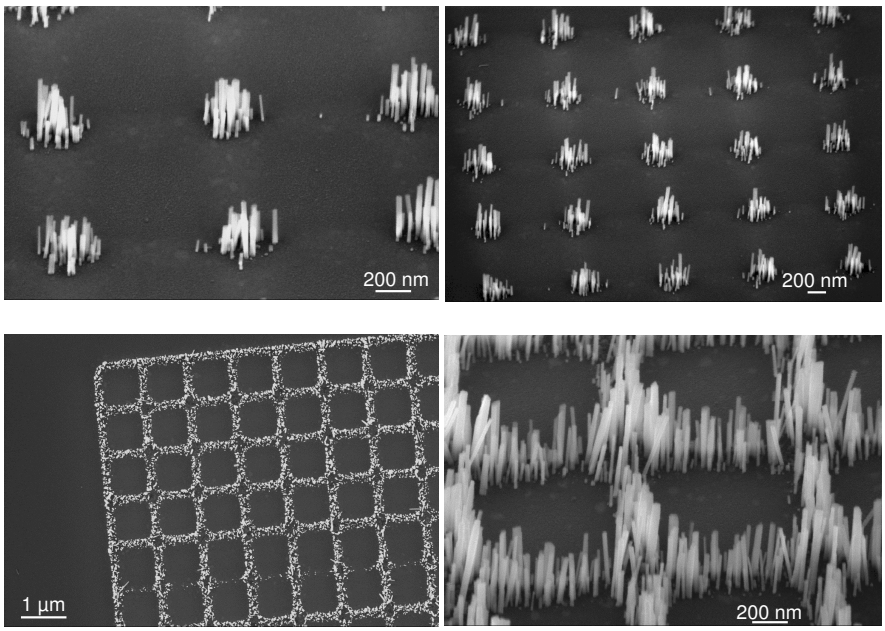

Figure 5.59: GaN nanowhiskers on Si(111) with a 20 nm AlN layer and a 5 nm Si structured with a mesh of stripes. Top: nominal depth of the structure in Si: 10 nm, bottom: nominal depth of the structure in Si: 20 nm.

On the bare silicon substrate, growth of GaN nanowhiskers was enhanced on the patterned areas but did also occur on the rest of the sample (fig. 5.56). The single whiskers were not separated from each other. The reason is probably that there was not only one nucleation per nanopore. Apart from that, also the FIB holes are not always perfectly round, astigmatism e.g. leads to rather elliptic holes, cf. chapter 3. If this occurs, the holes sometimes even overlap.
On the silicon sample with a 5 nm aluminium nitride layer, the difference between growth on the patterned area and outside the structure is considerable (figs. 5.57 and 5.58). Gallium desorption seems to be enhanced on the non-patterned area where a low density of GaN nanowhiskers was observed. In the case of the hexagonal structure with holes, it is not clear if growth takes place in the holes or in-between the holes but some ordering of GaN nanowhiskers can be detected in the top view images. In the area of the mesh structure, growth takes place on the AlN dots.
Better selective growth of GaN nanowhiskers was obtained by pre-structuring a silicon substrate with a 20 nm AlN layer and a 5 nm Si layer on top (fig. 5.59). GaN nanowhiskers only formed within patterned areas. At a nominal depth $Z(Si) = 10$ nm, growth occurs at the intersection points of the mesh because there we have the double depth and the silicon layer is probably

milled at these points. At a nominal depth $Z(Si) = 20$ nm, growth occurs on the stripes but not at the intersection points of the mesh. This can be explained by the assumption that in this case, silicon is milled at the stripes and both the Si and the AlN layer are milled at the intersection points. Apparently, growth occurs more likely on AlN. However, to know exactly the influence of AlN on the growth, more investigations are still necessary.

Summary

In this work, the growth of silicon and germanium nanowhiskers by vapor-liquid-solid mechanism via physical vapor deposition in ultra-high vacuum has been investigated with regard to their size, orientation and position.

The lateral dimension of nanowhiskers could be mainly influenced by the diameter of the solution droplets they grew from. This was determined by the parameters of solvent rate and evaporation time, substrate temperature, preparation and pre-annealing of the sample. Droplets and nanowhiskers were mainly investigated by scanning electron microscopy. For silicon nanowhisker growth, two different solvents – gold and indium – were applied. Droplet formation was influenced by solubilities and surface energies which led to a very different behavior of gold and indium on silicon. On the basis of droplet formation, the better feasibility of nanowhisker growth from gold than from indium was explained.
The length of nanowhiskers could be increased by the parameters of silicon or germanium evaporation rate and time. For silicon, this was investigated in detail by cross-section scanning electron microscopy. A higher silicon evaporation rate increased the ratio of whisker length and thickness of the layer in-between the whiskers. A longer evaporation time did not influence this ratio. It was found that thinner whiskers grow faster than thicker ones. This fact was discussed based on theoretical calculations from the literature, dealing with the influence of diffusion during the growth process.

By transmission electron microscopy (TEM), the orientation of silicon nanowhiskers was verified to be (111) like the one of the silicon substrate used. Germanium nanowhiskers on the other hand grew mainly in a <110> direction on the (111) germanium substrate. TEM measurements revealed that they started growing in the [111] direction and then proceeded in a <110> direction. This could be reproduced by growing SiGe heterostructures on silicon substrates. Silicon grew in the [111] direction and the subsequently evaporated germanium in a <110> direction on the silicon whisker forming a

kink at the interface between silicon and germanium. To explain these facts, nucleation energies on different facets of the crystal were considered. The result of these calculations was that at high supersaturation of the solvent droplet and at high substrate temperature, nucleation should be favored on (111) facets and at lower supersaturation and temperature on (110). This could explain the results of our experiments as silicon nanowhiskers were grown at higher temperatures than germanium nanowhiskers. To change the conditions for silicon nanowhisker growth keeping the temperature constant, the rate was decreased. Some first results showed that it was possible to grow silicon nanowhiskers in <110> direction as well.

A method was developed to position nanodroplets of the solvent material and thus to obtain a regular arrangement of nanowhiskers. For this purpose, substrates were pre-structured with nanopores by focused ion beams (FIB). Gold droplets have been successfully arranged both on silicon and germanium substrates. A regular array of epitaxial silicon nanowhiskers has been obtained as well. Moreover, the effect of FIB structuring on different surfaces has not only been investigated by the subsequent growth experiments – mainly growth of silicon and germanium whiskers but within the scope of a cooperation also growth of GaN nanowhiskers – but also by detailed atomic force microscopy measurements.

In conclusion, in the course of this work, a better understanding of the growth process of silicon and germanium nanowhiskers was achieved, especially with regard to their size, orientation and position.
For future investigations, some improvements regarding the experimental conditions are suggested. An in situ observation during growth by RHEED (reflection high energy electron diffraction) could be helpful to know exactly the surface state of a substrate before evaporation and to watch the early stages of droplet formation. A larger range of stable silicon rates would answer the question more precisely as to how a very low rate influences the orientation of the whiskers and how a very high rate influences the ratio of whisker length and thickness of the layer in-between the whiskers. A better base vacuum and the possibility of attaining higher substrate temperatures would assure clean substrate surfaces which could be verified by RHEED. A good solution would be the combination of the present growth method with gas source molecular beam epitaxy to attain higher growth rates of the whiskers and to compare those results to the ones achieved by solid source physical vapor deposition.

Bibliography

[1] H. Kroemer. Nano-whatever: Do we really know where we are heading? *physica status solidi (a)*, 202:957–964, 2005.

[2] C. Thelander et al. Nanowire-based one-dimensional electronics. *Materials Today*, 9:28–35, 2006.

[3] B. Yu et al. One-Dimensional Germanium Nanowires for Future Electronics. *Journal of Cluster Science*, 17:579–597, 2006.

[4] H. Adhikari et al. Germanium Nanowire Epitaxy: Shape and Orientation Control. *Nano Letters*, 6:318–323, 2006.

[5] V. Schmidt et al. Realization of a Silicon Nanowire Vertical Surround-Gate Field-Effect Transistor. *Small*, 2:85–88, 2006.

[6] J. Xiang et al. Ge/Si nanowire heterostructures as high-performance field-effect transistors. *Nature*, 441:489–493, 2006.

[7] R.S. Wagner and W.C. Ellis. Vapor-liquid-solid mechanism of single crystal growth. *Applied Physics Letters*, 4(5):89–90, 1964.

[8] E.I. Givargizov. Fundamental aspects of VLS growth. *Journal of Crystal Growth*, 31:20–30, 1975.

[9] H. Wu et al. High-Yield GaN Nanowire Synthesis and Field-Effect Transistor Fabrication. *Journal of Electronic Materials*, 35(4):670–674, 2006.

[10] I. Regolin et al. Composition control in metal-organic vapor-phase epitaxy grown InGaAs nanowhiskers. *Journal of Applied Physics*, 100: 074321, 2006.

[11] N. Zakharov et al. Growth of Si whiskers by MBE: Mechanism and peculiarities. *Physica E*, 37:148–152, 2007.

[12] T. Boeck et al. A method to grow silicon crystallites on glass. *Journal of Crystal Growth*, 198/199:420–424, 1999.

[13] Brent A. Wacaser. Nanoscale Crystal Growth - The Importance of Interfaces and Phase Boundaries. *Lund University, PhD Thesis*, 2007.

[14] A.I. Persson et al. Solid-phase diffusion mechanism for GaAs nanowire growth. *Nature Materials*, 4:677–681, 2004.

[15] G.A. Bootsma and H.J. Gassen. A quantitative study on the growth of silicon whiskers from silane and germanium whiskers from germane. *Journal of Crystal Growth*, 10:223–234, 1971.

[16] K.A. Dick et al. Failure of the Vapor-Liquid-Solid Mechanism in Au-Assisted MOVPE Growth of InAs Nanowires. *Nano Letters*, 5:761–764, 2005.

[17] T.I. Kamins et al. Ti-catalyzed Si nanowires by chemical vapor deposition: Microscopy and growth mechanisms. *Journal of Applied Physics*, 89:1008–1016, 2001.

[18] Y. Wang et al. Epitaxial growth of silicon nanowires using an aluminium catalyst. *Nature Nanotechnology*, 1:186–189, 2006.

[19] C.J. Novotny and P.K.L. Yu. Vertically aligned, catalyst-free InP nanowires grown by metalorganic chemical vapor deposition. *Applied Physics Letters*, 87:203111, 2005.

[20] D.T.J. Hurle (ed.). *Handbook of Crystal Growth 1: Fundamentals, Part A: Thermodynamics and Kinetics*. North-Holland Publishing, 1993. ISBN 978-0444889089.

[21] J. Honerkamp. *Statistical Physics: An Advanced Approach with Applications*. Springer, 2007. ISBN 978-3540430209.

[22] A.C. Zettlemoyer (ed.). *Nucleation*. Marcel Dekker, 1970. ISBN 978-0824718220.

[23] W. Thomson. Equilibrium Vapour at a Curved Surface of a Liquid. *Philosophical Magazine*, 42:448–452, 1871.

[24] X.Y. Liu. Heterogeneous nucleation or homogeneous nucleation? *Journal of Chemical Physics*, 112(22):9949–9955, 2000.

[25] T. Young. An essay on the cohesion of fluids. *Philosophical Transactions of the Royal Society*, 95:65–87, 1805.

[26] H.-J. Butt et al. On the Derivation of Young's Equation for Sessile Drops: Nonequilibrium Effects Due to Evaporation. *Journal of Physical Chemistry B*, 1113:5277–5283, 2007.

[27] R. Vallée et al. Size and segregation effects on the phase diagrams of nanoparticles of binary systems. *Nanotechnology*, 12:68–74, 2001.

[28] G. Abudukelimu et al. Theoretical phase diagrams of nanowires. *Journal of Material Research*, 21(11):2829–2834, 2006.

[29] H. Adhikari et al. Metastability of Au-Ge Liquid Nanocatalysts: Ge Vapor-Liquid-Solid Nanowire Growth Far below the Bulk Eutectic Temperature. *ACSNANO*, 1(5):415–422, 2007.

[30] V.G. Dubrovskii et al. The Role of Surface Diffusion of Adatoms in the Formation of Nanowire Crystals. *Semiconductors*, 40(9):1075–1082, 2006.

[31] W. Kern and D.A. Puotinen. Cleaning solutions based on hydrogen peroxide for use in silicon semiconductor technology. *RCA Review*, 31: 187–206, 1970.

[32] H. Angermann. *Chemische Konditionierung der Silicium-Oberfläche.* Berliner Debatte, 2001. ISBN 978-3931703899. P. 90.

[33] T. Akane et al. New Ge substrate cleaning method for $Si_{1-x-y}Ge_xC_y$ MOMBE growth. *Thin Solid Films*, 294:153–156, 1997.

[34] Dr. Eberl, MBE-Komponenten GmbH. Temperature at vapor pressure. http://www.mbe-components.com/applications/vap_data.html, web page.

[35] M. Knudsen. Experimentelle Bestimmung des Druckes gesättigter Quecksilberdämpfe bei 0 °C und höheren Temperaturen. *Annalen der Physik*, 334(6), 1909.

[36] J. Melngailis. Critical Review: Focused ion beam technology and applications. *Journal of Vacuum Science and Technology B*, 5(2):469–495, 1987.

[37] S.J. Pearton et al. *Topics in Growth and Device Processing of III-V Semiconductors*. World Scientific Publishing Company, 1996. ISBN 978-9810218843. P. 227.

[38] C. Chatillon and D. Chatain. Congruent vaporization of GaAs(s) and stability of Ga(l) droplets at the GaAs(s) surface. *Journal of Crystal Growth*, 151:91–101, 1995.

[39] S. Kocsis and E. Lendvay. The Thermal Etching of GaP. *Kristall und Technik*, 9:1131–1140, 1974.

[40] K. Deppert et al. Feasibility study of nanoparticle synthesis from powders of compounds with incongruent sublimation behavior by the evaporation/condensation method. *Nanostructured Materials*, 10:565–573, 1998.

[41] U. Voland et al. X-ray Diffraction Studies of Interdiffusion in InP-GaP Powder Blends. *Crystal Research and Technology*, 24(11):1177–1185, 1989.

[42] P.W. Nebiker. Strukturierung von Silizium mit niederenergetischen fokussierten Ionenstrahlen. *ETH Zürich, PhD Thesis*, 1997.

[43] J. Yanagisawa et al. Nanoporous structure formations on germanium surfaces by focused ion beam irradiations. *Journal of Physics: Condensed Matter*, 19:445002, 2007.

[44] L.-V. de Broglie. Recherches sur la théorie des quanta. *Sorbonne, Paris, PhD Thesis*, 1924.

[45] S.L. Flegler et al. *Elektronenmikroskopie*. Spektrum Akademischer Verlag, 1995. ISBN 978-3860253410.

[46] L. Reimer. *Scanning Electron Microscopy: Physics of Image Formation and Microanalysis*. Springer Verlag, 2008. ISBN 978-3540639763.

[47] H. Bethge and J. Heydenreich. *Elektronenmikroskopie in der Festkörperphysik*. Springer Verlag, 1982. ISBN 978-3540113614.

[48] E. Abbe. Beiträge zur Theorie des Mikroskops und der mikroskopischen Wahrnehmung. *Archiv f. Mikroskop. Anatomie*, 9:413–468, 1873.

[49] E. Müller and D. Abou-Ras. Preparation of cross-section samples for transmission electron microscopy (TEM). http://www.emez.ethz.ch/equipment/pips.pdf, web page.

[50] L. Reimer. *Transmission Electron Microscopy. Physics of Image Formation and Microanalysis*. Springer Verlag, 1989. ISBN 978-3540504993.

[51] W. Nolting. *Grundkurs Theoretische Physik 3: Elektrodynamik*. Springer Verlag, 2004. ISBN 978-3540205098.

[52] K. Kopitzki and P. Herzog. *Einführung in die Festkörperphysik*. Vieweg+Teubner Verlag, 2007. ISBN 978-3835101449.

[53] L.G. Parratt. Surface Studies of Solids by Total Reflection of X-Rays. *Physical Review*, 95:359–369, 1954.

[54] R.M. Öksüzoglu. Magnetowiderstand und Mikrostruktur Eigenschaften in gesputterten granularen Co25Ag75- und (Co0.9Al0.1)xAg1-x-Schichten. *TU Darmstadt, PhD Thesis*, 2000.

[55] C. Braun. Parratt 32 or the Reflectivity Tool. *HMI Berlin, PhD Thesis*, 2002.

[56] J.Y. Yu et al. Silicon Nanowires: Preparation, Device Fabrication, and Transport Properties. *The Journal of Physical Chemistry B*, 104:11864–11870, 2000.

[57] D.E. Perea et al. Composition analysis of single semiconductor nanowires using pulsed-laser atom probe tomography. *Applied Physics A*, 85:271–275, 2006.

[58] J.E. Allen et al. High-resolution detection of Au catalyst atoms in Si nanowires. *Nature Nanotechnology*, 3:168–173, 2008.

[59] S.M. Sze. *Physics of Semiconductor Devices*. Wiley-Interscience, 1981. ISBN 978-0471056614. P. 21.

[60] L. Rubin and J. Poate. Ion Implantation in Silicon Technology. *The Industrial Physicist*, June/July:12–15, 2003.

[61] C.E. Allen et al. Surface diffusion of In on Si(111): Evidence for surface ionization effects. *Journal of Vacuum Science and Technology A*, 14: 22–29, 1996.

[62] E.G. Seebauer and C.E. Allen. Estimating Surface Diffusion Coefficients. *Progress in Surface Science*, 49:265–330, 1995.

[63] W. Jun et al. Real time STM observation of Au-assisted decomposition of SiO2 films on Si(111) at elevated temperatures. *Surface Science*, 506: 66–79, 2002.

[64] Y.V. Naidich et al. The wettability of silicon carbide by Au-Si alloys. *Materials Science and Engineering: A*, 245:293–299, 1998.

[65] L.Z. Mezey and J. Giber. The Surface Free Energies of Solid Chemical Elements: Calculation from Internal Free Enthalpies of Atomization. *Japanese Journal of Applied Physics*, 21:1569–1571, 1982.

[66] Ch. Wohlfahrt and B. Wohlfahrt. *Landolt-Börnstein New Series IV/16: Surface Tension of Pure Liquids and Binary Liquid Mixtures*. Springer, 1997. ISBN 978-3540632764.

[67] D.B. Asay and S.H. Kim. Effects of adsorbed water layer structure on adhesion force of silicon oxide nanoasperity contact in humid ambient. *The Journal of Chemical Physics*, 124:174712, 2006.

[68] B. Janczuk and A. Zdziennicka. A study on the components of surface free energy of quartz from contact angle measurements. *Journal of Materials Science*, 29:3559–3564, 1994.

[69] S. Coffa et al. Determination of diffusion mechnisms in amorphous silicon. *Physical Review B*, 45:8355–8358, 1992.

[70] L. Schubert et al. Silicon nanowhiskers grown on <111>Si substrates by molecular-beam epitaxy. *Applied Physics Letters*, 84:4968–4970, 2004.

[71] E.I. Givargizov and N.N. Sheftal. Morphology of Silicon Whiskers grown by the VLS-Technique. *Journal of Crystal Growth*, 9:326–329, 1971.

[72] F. Iacopi et al. Alternative Catalysts For Si-Technology Compatible Growth Of Si Nanowires. *Material Research Society Symposium Proceedings*, 1017:DD01–10–EE01–10, 2007.

[73] V.A. Nebol'sin and A.A. Shchetinin. Role of Surface Energy in the Vapor-Liquid-Solid Growth of Silicon. *Inorganic Materials*, 39:899–903, 2003.

[74] V.V. Voronkov. Processes at the Solidification Interface. *Kristallografiya*, 19:922–929, 1974.

[75] S.M. Paik and S. Das Sarma. Dynamical simulation of molecular beam epitaxial growth of a model crystal. *Physical Review B*, 39(2):1224–1228, 1989.

[76] H.K.D.H. Bhadeshia. Crystal Strucures. http://www.msm.cam.ac.uk/phase-trans/2003/MP1.crystals/MP1.crystals.html, web page.

[77] I. Grzegory et al. Mechanisms of crystallization of bulk GaN from the solution under high N2 pressure. *Journal of Crystal Growth*, 246:177–186, 2002.

[78] M.T. Björk et al. One-dimensional heterostructures in semiconductor nanowhiskers. *Applied Physics Letters*, 80:1058–1060, 2002.

[79] S.K. Park et al. Low-temperature solid-phase-crystallization in $Si_{1-x}Ge_x/SiO_2$. *Applied Surface Science*, 159-160:116–120, 2000.

[80] Y. Wu et al. Controlled Growth and Structures of Molecular-Scale Silicon Nanowires. *Nano Letters*, 4:433–436, 2004.

[81] M. Albrecht. Surface energy and strain relaxation in heteroepitaxial growth – an analysis of solution grown GeSi. *Universität Hamburg, PhD Thesis*, 1995.

[82] R.K. Debnath et al. Mechanism of molecular beam epitaxy growth of GaN nanowires on Si(111). *Applied Physics Letters*, 90:123117, 2007.

[83] R. Calarco et al. Nucleation and Growth of GaN Nanowires on Si(111) Performed by Molecular Beam Epitaxy. *Nano Letters*, 7:2248–2251, 2007.

[84] T. Stoica et al. Interface and Wetting Layer Effect on the Catalyst-Free Nucleation and Growth of GaN Nanowires. *Small*, 4:751–754, 2008.

Publications

1. Vapour-liquid-solid mechanism as a tool for the growth of micro- and nanostructures
T. Boeck, A. Kramer, P. Schramm, Th. Teubner, P.-M. Wilde, R. Fornari
Proc. Joint Italo–German Meeting on: Current Issues in Crystal Growth from the Vapour
edited by S. Carrà and C. Paorici
Bardi Editore Srl / Accademia Dei Lincei Rome (2007), 99-113

2. Investigation of Au and In as solvents for the growth of silicon nanowires on Si(111)
A. Kramer, T. Boeck, P. Schramm, R. Fornari
Physica E **40** (2008), 2462-2467

3. Self-assembled and ordered growth of silicon and germanium nanowires
A. Kramer, M. Albrecht, T. Boeck, T. Remmele, P. Schramm, R. Fornari
submitted to Superlattices and Microstructures

Acknowledgements

I am grateful to Prof. Roberto Fornari for giving me the possibility of working on the interesting topic of nanowhisker growth at the Leibniz Institute for Crystal Growth in Berlin, and for his encouragement and advice.

I wish to express my special gratitude to the head of the group Si/SiGe nanostructures, to my mentor Dr. Torsten Boeck, for supporting this dissertation with his scientific expertise and for encouraging me in every phase of this work. I am very grateful to all group members for the nice work atmosphere and for the fact that I could always rely on their support. In particular, I would like to thank Peter Schramm for devoting so much time and energy to solve any problems related to the experimental equipment. In this context, I would like to thank Uwe Jendritzki from the group Equipment Maintenance and Development as well.

I would like to thank the characterization group of our institute, especially Dr. Martin Albrecht for his advice concerning scanning electron microscopy and focused ion beam structuring and for the many fruitful discussions, Thilo Remmele for sample characterization at the transmission electron microscope and Dr. Martin Schmidbauer for the x-ray reflectometry measurements.

I am very grateful to Dr. Raffaella Calarco, Dr. Toma Stoica and Dr. Gregor Mussler from Forschungszentrum Jülich for the fruitful cooperation in the field of arrangement of GaN nanowhiskers on pre-structured substrates.

For proof-reading, I would like to thank Suzanne Vorbrugg and Günther Grupp.